

UCLA

UCLA Electronic Theses and Dissertations

Title

QUANTITATIVE EVALUATION OF LEFT VENTRICULAR ROTATIONAL MECHANICS USING
MAGNETIC RESONANCE IMAGING

Permalink

<https://escholarship.org/uc/item/3v44x8c9>

Author

Wang, Zhe

Publication Date

2015

Peer reviewed|Thesis/dissertation

UNIVERSITY OF CALIFORNIA

Los Angeles

**QUANTITATIVE EVALUATION OF LEFT VENTRICULAR
ROTATIONAL MECHANICS USING MAGNETIC RESONANCE
IMAGING**

A dissertation submitted in partial satisfaction of the
requirements for the degree Doctor of Philosophy
in Biomedical Engineering

By

Zhe Wang

2015

© Copyright by

Zhe Wang

2015

ABSTRACT OF THE DISSERTATION

Quantitative Evaluation of Left Ventricular Rotational Mechanics using Magnetic
Resonance Imaging

By

Zhe Wang

Doctor of Philosophy in Biomedical Engineering

University of California, Los Angeles, 2015

Professor Daniel B. Ennis, Chair

Cardiac magnetic resonance imaging (MRI) is a proven technique for the evaluation of myocardial structure and function. An introduction to cardiac physiology is presented in Chapter 1, wherein a measure of LV rotational mechanics called LV twist is defined. LV twist is the apparent rotation of the LV apex relative to the LV base and provides insight into LV function beyond that traditionally reported in measures like ejection fraction. Importantly, cardiac MRI techniques are very well suited to evaluating cardiac structure and function and these methods are outlined in Chapter 2. In particular, MRI tagging can be used to non-invasively generate myocardial tissue landmarks that facilitate the qualitative and quantitative assessment of left ventricular (LV) myocardial deformation in both research and clinical settings. This thesis focuses on several developments. First, we developed a new tagging technique called complementary radial tagging (CRT) that generates a tagging pattern that better matches the annular shaped LV myocardium in the short-axis view. CRT also has better tag contrast during

late diastolic phases and can be used to accurately measure the LV mechanics during all cardiac phases (Chapter 3).

In parallel with the development of the CRT technique we used conventional clinical tagging protocols to measure LV rotational mechanics quantitatively. Myocardial fibrosis is known to frequently occur in patients with Duchenne Muscular Dystrophy (DMD). The consequences of myocardial fibrosis on LV mechanics, however, are incompletely understood. In Chapter 4 we report on the LV rotational mechanics in patients with DMD with or without myocardial fibrosis. The results suggested that both DMD and the presence of myocardial fibrosis independently worsen LV rotational mechanics.

In Chapter 5 we report on the effects of conventional cardiac MRI exams, which require repeated breath holding and place a burden on some clinical patients, on measure of LV rotational mechanics. This breath hold paradigm presents two problems for patients with DMD who typically develop progressive respiratory impairment and the signs and symptoms of cardiac involvement at an early age. Currently, clinical protocols use both breath-hold and free breathing techniques, as needed, to acquire data. Chapter 5 compared the LV rotational mechanics between these techniques in healthy subjects and patients with DMD. It was found that free-breathing significantly decreases estimates of LV twist compared to breath hold measures. The results suggest that when using quantitative imaging biomarkers of LV rotational mechanics to monitoring disease progression or the response to therapy, especially in patients with DMD for whom decline in respiratory function is certain, it is important to use a free-breathing strategy for all studies to facilitate intra-subject longitudinal comparisons.

In Chapter 6, LV rotational mechanics were further evaluated in patients with mitral regurgitation. In patients with mitral regurgitation LV twist decreases, while CL-shear angle (an alternate measure of LV rotational mechanics) pseudo-normalized due to subtle changes in the heart's geometry.

Lastly, in Chapter 7, a technique for acquiring two slices simultaneously – Controlled Aliasing In Parallel Imaging Results In Higher Acceleration (CAIPIRINHA) was implemented in a cardiac MRI tagging sequence. The application of CAIPIRINHA to a LV tagging sequence is shown to achieve similar estimates of peak LV twist in a single breath hold, which simplifies the exam and avoids measurement differences that may arise from data acquired in different breath holds.

In conclusion, this thesis reports on several technical developments and clinical applications related to estimating quantitatively the function of the left ventricle. Taken together these developments can be combined to provide fast and accurate estimates of LV rotational mechanics that provide insight to LV function beyond traditional measures.

This dissertation of Zhe Wang is approved:

Danny Jiong Jiong Wang

Peng Hu

Holden Wu

M. Albert Thomas

Daniel B. Ennis, Committee Chair

University of California, Los Angeles

2015

Table of Contents

List of Figures and Tables.....	vii
Vita.....	viii
Chapter 1: Introduction to Cardiac Physiology and Function.....	1
Chapter 2: Introduction to Cardiovascular Magnetic Resonance Imaging.....	12
Chapter 3: Complementary Radial Tagging for Improved Myocardial Tagging Contrast	29
Chapter 4: The Effect of Myocardial fibrosis in left ventricular rotational mechanics in Duchenne Muscular Dystrophy	53
Chapter 5: The Effect of Free-breathing on Left Ventricular Rotational Mechanics in Normal Subjects and Patients with Duchenne Muscular Dystrophy	61
Chapter 6: Left Ventricular Twist and Shear-Angle in Patients with Mitral Regurgitation	76
Chapter 7: Single Breath-hold Estimates of Left Ventricular Rotational Mechanics	95
Chapter 8: Thesis Summary	104
References	105

List of Figures and Tables

Figure 1.1.....	2	Table 4.1.....	58
Figure 1.2.....	5	Figure 4.1.....	58
Figure 1.3.....	7	Table 5.1.....	62
Figure 1.4.....	8	Figure 5.1.....	66
Figure 2.1.....	13	Figure 5.2.....	68
Figure 2.2.....	15	Table 5.2.....	69
Figure 2.3.....	19	Figure 5.3.....	70
Figure 2.4.....	20	Table 6.1.....	82
Figure 2.5.....	21	Figure 6.1.....	83
Figure 2.6.....	24	Table 6.2.....	84
Figure 2.7.....	27	Figure 6.2.....	85
Figure 2.8.....	28	Figure 6.3.....	86
Figure 3.1.....	32	Figure 6.4.....	87
Figure 3.2.....	34	Figure 6.5.....	88
Figure 3.3.....	41	Figure 6.6.....	89
Figure 3.4.....	42	Table 6.3.....	90
Figure 3.5.....	43	Figure 7.1.....	97
Table 3.1.....	44	Figure 7.2.....	100
Figure 3.6.....	45	Table 7.2.....	100
Figure 3.7.....	46	Figure 7.3.....	101
Figure 3.8.....	48	Table 7.1.....	101
Figure 3.9.....	49	Table 7.2.....	102

Vita

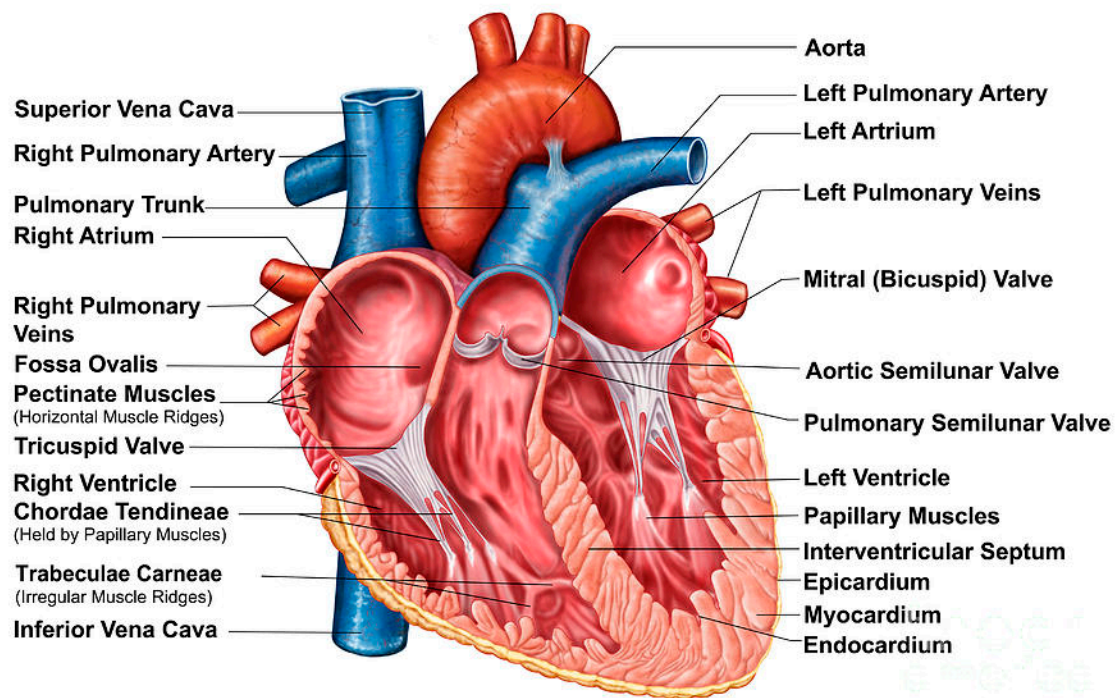
2009-2015 Doctor of Philosophy Candidate, Department of Biomedical Engineering, University of California, Los Angeles, the U.S.A.

2007-2009 Master of Science, Department of Biomedical Engineering, Case Western Reserve University, Cleveland, Ohio, the U.S.A.

2002-2006 Bachelor of Science, Department of Bioengineering, Shanghai Jiao Tong University, Shanghai, China

Chapter 1 Introduction to Cardiac Physiology and Function

The human heart is composed of four chambers: Left Atrium (LA), Left Ventricle (LV), Right Atrium (RA) and Right Ventricle (RV) (Figure 1.1). The heart pumps blood through two coupled circulatory systems – the systemic circulatory system and the pulmonary circulatory system. Oxygenated blood (high O₂ concentration) drains from the lungs and flows into the LA and enters the LV through the mitral valve. Contraction of the LV ejects blood past the aortic valve, through aorta, and into the systemic circulation to the rest of the body. After oxygen is consumed during metabolism, deoxygenated blood (low O₂ concentration) from the systemic circulation flows back into the RA from the superior and inferior vena cava. It then enters the RV through the tricuspid valve and the RV then pumps the blood through the pulmonary valve into the pulmonary circulation and the lungs where the blood exchanges oxygen and carbon dioxide. The blood also carries the necessary nutrients from the liver and gastrointestinal tract to all organs of the body, while transporting waste to the liver and kidneys. In healthy subjects, the heart is located in the middle compartment of the mediastinum in the chest (1) towards the left side of the body. In addition, muscle mass is greater on the left side and the apex of the heart is pointed slightly to the left too, which makes apparent a palpable cardiac impulse on the left side of the chest, especially in thin individuals.



(Sylvia S. Mader. Inquiry into life 8th edition)

Figure 1.1 Human Heart Anatomical Terminology

Human Heart Development

Heart development begins as early as 18 days after fertilization. Precursor cells in cardiogenic region start to develop and form a paired region called endocardial tubes. These paired two cell layers migrate and join together to form the primitive embryonic heart tube (2). Then the tubular heart continues to increase its mass and form the primary formats of the four chambers. At about day 23 the primary heart undergoes morphogenesis where the tubular heart begins to fold into an S-shape (3). The folding process ends at about day 28 where the primitive four chambers and the major vessels are aligned into the correct location and continue to grow into the mature heart. (3). Until this stage the heart is the first functional organ. The heart beat starts at week 4. Further

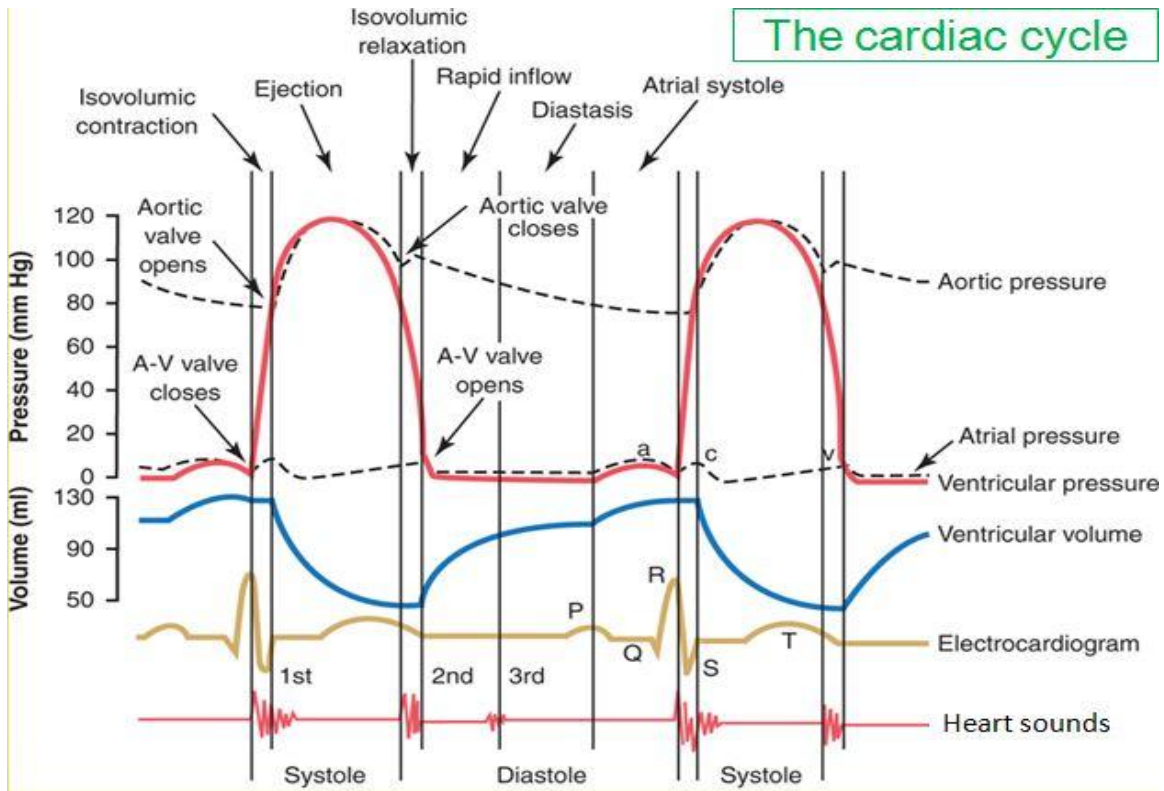
development includes an increase in myocardium mass and formation of the septa and valves until the ninth week.

Human embryonic heart begins beating approximately 22 days after fertilization. Myocytes in the primitive heart tube initiate rhythmic heart beating by electrical depolarization and repolarization. This electrical activity begins in the pacemaker cells (4). Pacemaker cells develop in the primitive atrium and the sinus venosus to form the sinoatrial node and the atrioventricular node respectively. Conductive cells develop into the bundle of His and Purkinje fibers that transduce the electrical activity into other parts of the heart (5). The human embryonic heart begins beating at a rate near to the mother's 75-80 Beats Per Minutes (BPM), then increases to 160-180 BPM during early embryonic development (6). After week 9 the heart rate starts to decrease until 140 BPM at birth. From the fetal stage through early childhood, adolescences and adulthood the human the heart rate gradually decreases to a normal level of 65-75 BPM (6).

Heart Contraction and Electrical Activity

Triggered by the auto-rhythmic action potential in the pacemaker cells, cardiac muscle has the unique ability to contract and relax. The "cardiac cycle" is the term used to describe one heartbeat. It begins with contraction of the atria (systole) and ends with ventricular relaxation (diastole). The frequency of the cardiac cycle is often described by heart rate and measured by beats-per-minute (BPM). The human heart rate varies according to the body's physical conditions. The normal heart rate ranges from ~65-75 BPM under rest to over 150 BPM during exercise(7) and can be modulated by the endocrine and nervous systems(3). One cardiac cycle can be divided into several small

steps. In the first step the pulmonary and aortic valves remain closed; the mitral valve and tricuspid valve remains open, and the whole heart is in early diastole (relaxed). At the end of the first step, the atria contracts and blood is further squeezed from the atria into the ventricles. This step is often called ventricular filling stage. In the second step, the ventricles begin to contract with all of the valves closed. There is no net blood flow and the pressure in the ventricles increases to prepare for the ejection of blood. Since there is no blood volume change within the chamber, this step is often called isovolumic contraction (IVC). In the third step the pulmonary and aortic valves open and blood is ejected into the pulmonary artery (right ventricle) and the aorta (left ventricle) (8). This step is referred to as ventricular ejection stage. In the last step, the ventricles stop contracting and begin to relax, and the semilunar valves close due to pressure decreases in ventricles. No blood enters the ventricles and this step is called Isovolumic relaxation time (IVR). After IVR, the mitral valve and tricuspid valve open again and the whole heart relaxes and returns to step one. Throughout the cardiac cycle, blood pressure increases and decreases (9) (Figure 1.2).



(Mina, Anatomy & Physiology Bg 211, Erskine College)

Figure 1.2 Diagram of the Cardiac Cycle

The apparent electrical activity of the heart be recorded using electrocardiography (ECG). A typical ECG tracing of the cardiac cycle consists of a P wave (atrial depolarization and contraction), a QRS complex (ventricular depolarization and contraction) and a T wave (ventricular repolarization and relaxation) (Figure 1.2). During normal atrial depolarization, the main electrical vector is directed from the SA node towards the AV node and spreads from the right atrium to the left atrium. This is apparent as the P wave on the ECG. The QRS complex reflects the rapid depolarization of the right and left ventricles. The ventricles have a large muscle mass compared to the atria, so the QRS complex usually has much larger amplitude than the P-wave. The T wave represents the repolarization (or relaxation) of the ventricles. The interval from the

beginning of the QRS complex to the apex of the T wave is referred to as the absolute refractory period. (10).

Myocardium

The myocardium is the cardiac muscle that is constituted by cardiomyocytes. Myocytes are tubular shaped cell developed by the process of myogenesis. Cardiomyocytes are connected with neighboring cells by intercalated discs, which have high electrical conductivity. Action potentials spread quickly, which allows cardiac contraction between different cardiomyocytes at the same rate. Many myocytes form a tissue layer that is further wrapped in endomysium collagen fibers. Perisysium is a sheath of tissue that groups different endomysium fibers into bundles. Epimysium collagen provides the outermost layer and protects the myocytes from friction while sliding alongside one another during systole and diastole (11).

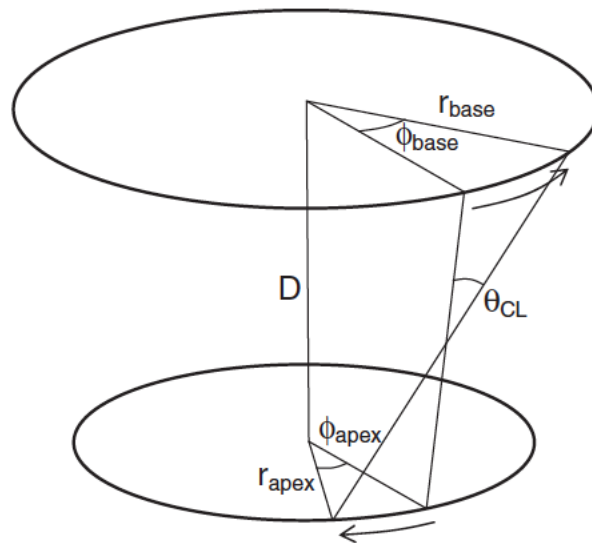
The basic structural formation of the myocardium can be described by subendocardial and subepicardial tissue layers. The orientation of each layer is described by the helical fiber orientation model (12). The fiber orientations have a nearly orthogonal arrangement within the two layers, which helps equally distribute stress and strain transmurally in the heart (13). A study presented by Chen et al. (14) measured fiber and sheet (collections of myocytes into laminae) angles and used histological staining to compare them to measures from Diffusion Tensor Magnetic Resonance Imaging (DT-MRI). Given that DT-MRI has limited spatial resolution and a relative long scan time, DT-MRI can be used non-invasively to study the in vivo fiber orientation and structure (15). With regards to the sheet structure it has recently been shown that two

local myocardial sheet populations exist with mean sheet angles reported from DT-MRI of $36^\circ \pm 24^\circ$ and $-55^\circ \pm 28^\circ$ (16).

LV Twist

Left ventricular twist is defined as the rotational angle difference between the apical and the basal aspects of the heart (Figure 1.3).

$$LV\ Twist = \phi_{apex} - \phi_{base} \quad \text{Eq. 1.1}$$

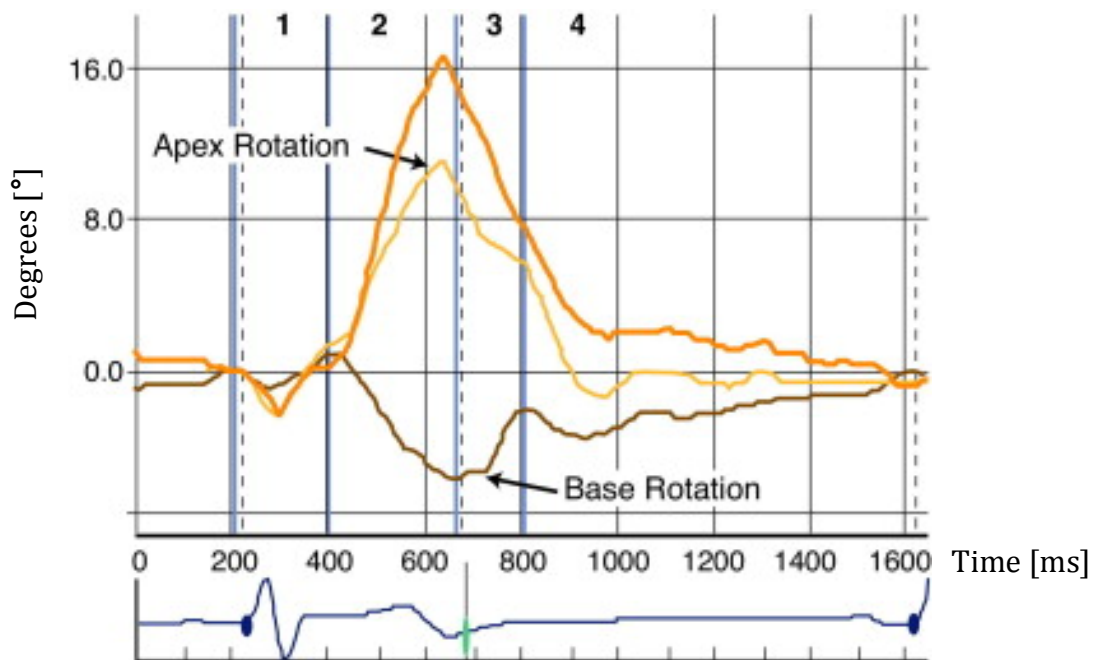


(Alistair A. Young *et al.* JCMR 2012, 14:49)

Figure 1.3 Left Ventricular Twist Diagram

The LV apex rotates counterclockwise during ejection followed by a clockwise rotation during IVR and the beginning of diastolic filling. The LV base has a clockwise rotation during ejection, and then a counterclockwise rotation during IVR and early diastole (13). It is conventional to define the positive values as counter-clockwise

rotations when viewed from the apex towards the base in a short-axis view (Figure 1.4).



(Partho P. Sengupta *et al.* Am Coll Cardiol Img. 2008;1(3):366-376)

Figure 1.4 Left ventricular twist during the cardiac cycle.

Helical layer model was proposed by Taber et al. (12) to explain the myocardial fiber alignment and contraction relative to the LV twist. During the apex to base sequence of electromechanical activation, the transmural spread of electrical activation leads to subendocardial to subepicardial shortening accompanied by subepicardial fiber stretching (13). The larger radius of the subepicardium results in greater torque, thus dominating the direction of rotation (12). This results in a global counterclockwise rotation near the apex and clockwise rotation near the base at the time of ejection. In the subendocardium, the myofibers rearrange and shear towards the LV cavity causing LV wall thickening (17). Both twisting and shearing of the fibers cause matrix

deformation and stores potential energy for release during diastolic recoil (13). Diastolic recoil at the time of IVR and early diastole releases the stored energy in the subendocardium, causing the myofibers to lengthen near the apex and drives recoil in a clockwise direction, while shortening of the subendocardial fiber occurs at the base (18). LV twist and shear aids in the distribution of fiber stress and fiber shortening across the left ventricular wall (19).

LV Shear Angle

By definition, LV twist (Equation 1.1) does not take into consideration the heart geometry, but only the rotational mechanics. CL-shear angle (Equation 1.2 and Figure 3) is a measure of the change in angle between two line segments, which are initially aligned with the anatomical circumferential and longitudinal axes of the LV. CL-shear normalizes for LV size (length and diameter) and can be calculated at any point in the ventricle. While there are different versions of the CL-shear equation (20), a formula given by Russel *et al.* (21) calculates the difference in circumferential displacement directly as (Equation 1.2)

$$CL - Shear = \frac{\phi_{apex}\rho_{apex} - \phi_{base}\rho_{base}}{D} \quad \text{Eq.1. 2}$$

where ρ is the epicardial radius of the apex or base in mm, and D is the distance between the apical and basal slices in mm. This version has been found to give unbiased estimates of the shear angle (22) and will be used in my work as the preferred definition.

LV Disease and Rotational Mechanics

Ejection Fraction (EF) is a parameter used in clinical reports to give overall evaluation of the heart's systolic function. Although widely used, unfortunately EF is a late outcome in disease process (23). Other parameters focus on LV rotational mechanics and may provide early insight to LV dysfunction. Strain, for example, measures the shortening and thickening of the LV wall. It is often described as radial, circumferential and longitudinal strains. Given its advantage to represent sub-pixel level movement, strain is relatively difficult to measure accurately and is an expression of regional function. Shear angle described above takes into consideration the heart geometry. However it tends to pseudo normalize in Duchenne Muscular Dystrophy (DMD) and mitral regurgitation patients, which will be demonstrated in later chapters. Thus they may not be suitable imaging biomarkers for the detection of LV dysfunction. On the other hand LV twist is relatively easy to measure accurately and gives global LV estimation. In addition, LV twist is sensitive to different cardiac disease and loading conditions.

Aortic stenosis, a disease wherein the aortic valve only partially opens and has been shown to significantly increase peak LV twist (24,25). Dilated cardiomyopathy (DCM), a condition in which the heart is weakened and enlarged, has been shown to lead to a decrease peak LV twist(26). In DCM, it is thought that a marked attenuation of LV apical rotation occurs, while basal rotation may be spared (27). However, in hypertrophic cardiomyopathy (HCM), a condition in which the heart muscle substantially thickens, peak LV twist has been shown to increase. It is thought that the apex to base progression of the rotation sequence is altered, such that the midlevel of the LV rotates in a clockwise direction, similar to that of the base (28,29). In DMD patients, a gene

mutation causes dysfunctional expression or a complete lack of the dystrophin protein (30). Ultimately, fibro-fatty tissue replaces damaged muscle cells and the result is progressive cardiomyopathy, a major contributor to morbidity and mortality in patients with DMD (31). Without the complexes that dystrophin normally forms in muscle cells, mechanical stress damages both cardiac and skeletal muscle (32). Similar to DCM patients, LV twist tends to decrease in DMD patients and may serve as a sensitive biomarker for disease diagnosis (Chapter 4 and 5) and progression. Chronic mitral regurgitation is a disease in which the mitral valve does not close properly. Decreased peak LV twist is observed in mitral regurgitation patients (33), which may be caused by a decreased leverage of the epicardial fibers relative to the endocardial muscle fibers (33,34).

Cardiac preload is a measure of the distending force or stretch of the ventricular wall at end diastole; while cardiac afterload is a measure of the resisting force faced by the LV during systolic ejection. Increasing preload leads to an increase in LV twist while increasing afterload leads to a decrease in LV twist. The effect on twist of preload is about two-thirds as great as that of afterload (35). It has also been shown that twist increases with increasing age (36). This increase is thought to be caused by attenuation in subendocardial function and an unopposed increase in LV apical rotation (36).

Chapter 2 Introduction to Cardiovascular Magnetic Resonance Imaging

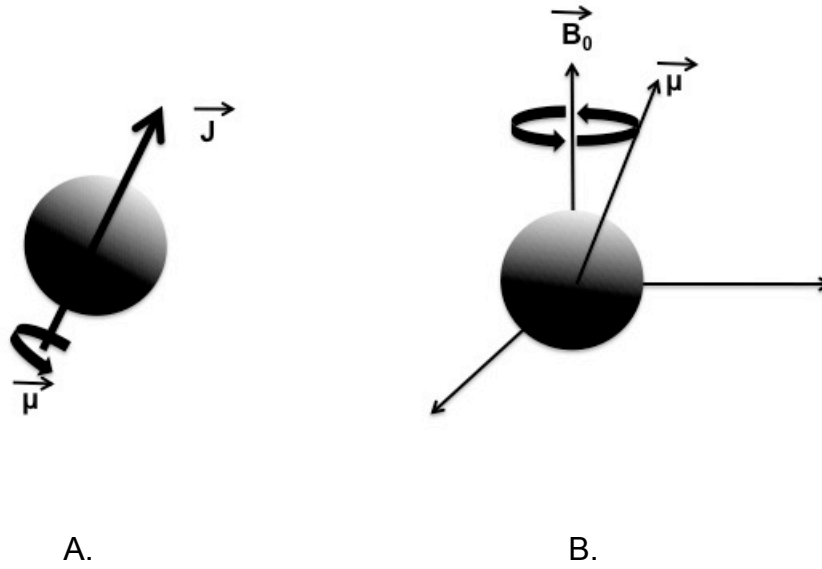
Nuclear Magnetic Resonance

Nuclear magnetic resonance is a physical phenomenon in which nuclei in a magnetic field absorb and re-emit electromagnetic radiation. This energy is at a specific resonance frequency, which depends on the strength of the magnetic field and the magnetic properties of the isotope of the atoms. The most commonly found atom in humans is the hydrogen atom, which is mainly contained in water, fat, and proteins. The rotation of positively charged particle induces a magnetic field, which can be represented by a nuclear magnetic dipole moment. The rotation of the nucleus, also known as angular momentum $\vec{\mu}$, is related to magnetic moment \vec{J} , by the following equation:(37,38) (Figure 2.1):

$$\vec{\mu} = \gamma \vec{J} \quad \text{Eq. 2.1}$$

where γ is known as the gyromagnetic ratio and for the hydrogen atom γ is measured as:(37,38)

$$\frac{\gamma}{2\pi} = 42.57 \text{MHz/T} \quad \text{Eq. 2.2}$$



(Haacke EM et al. Magnetic resonance imaging: physical principles and sequence design.)

Figure 2.1 A. Illustration of a magnetic dipole. B. Depiction of magnetic dipole in an external field, B_0 .

Normally the spins are randomly oriented in three-dimensional space. However when placed in an external magnetic field with field strength of B_0 , the spins have two energy status: parallel and anti-parallel. This energy difference is known as Zeeman splitting and is characterized by a Boltzmann distribution:

$$\frac{N^+ - N^-}{N} = \frac{1 - e^{\frac{\Delta E}{kT}}}{1 + e^{\frac{\Delta E}{kT}}} \approx -\frac{\Delta E}{2kT} = \frac{\gamma h B_0}{4\pi kT} \quad \text{Eq. 2.3}$$

,where N^+ and N^- stands for the number of spins in parallel and anti-parallel energy status. T is the equilibrium temperature of the system. h is the Planck constant. k is the Boltzmann constant. This difference is usually very small: 3 in 1 million at room temperature 300K and $B_0 = 1.0T$. However, since the number of hydrogen atoms in

humans is extremely huge (7×10^{19} per gram of water), the next effect is that a substantial number of spins are available to generate a net signal for MR imaging. The spin's precessional axis is aligned with the direction of the B_0 field. The precessional frequency is governed by Equation 2.4 (37-39):

$$\omega_0 = \gamma B_0 \quad \text{Eq. 2.4}$$

This frequency is called the Larmor frequency. Spins that have the same resonance frequency are called isochromat (39).

Excitation

As described above the bulk magnetization formed by a collection of spins points along the main magnetic field direction (z-direction). To generate a usable signal, the longitudinal magnetization has to be tilted into the transverse plane (xy-plane). This is achieved by adding an external RF pulse, which is a short and weak magnetic field (B_1). The carrier frequency of the RF pulse must match the Larmor frequency. The RF pulse can be written as:

$$B_a(t) = 2B_1^e \cos(\omega_0 + \phi) \vec{i} \quad \text{Eq. 2.5}$$

It is helpful to introduce a rotating frame (i, j, k) that rotates around the z-axis of the system at the Larmor frequency. In the presence of the B_0 and B_1 fields, the spin magnetization can be defined by Bloch equations (37-39):

$$\frac{dM}{dt} = \gamma M \times B - \frac{M_x i + M_y j}{T_2} - \frac{(M_z - M_z^0) k}{T_1} \quad \text{Eq. 2.6}$$

where M_z^0 is the thermal equilibrium value, T_1 is the spin-lattice time constant of relaxation of the bulk magnetization, and T_2 is the spin-spin relaxation time constant of the bulk magnetization. In the rotating frame Equation 2.6 can be rewritten as:

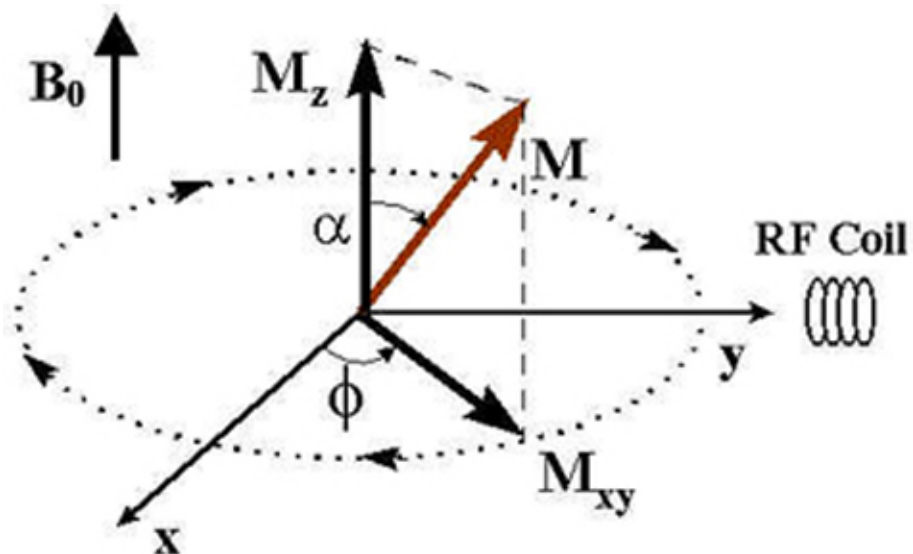
$$\frac{dM_{rot}}{dt} = \gamma M_{rot} \times B_{eff} \quad \text{Eq. 2.7}$$

$$B_{eff} = B_{rot} + \frac{\omega}{\gamma} \quad \text{Eq. 2.8}$$

The effect of the external RF pulse results in the magnetization M_z^0 , which is originally aligned along the longitudinal direction, to have a component of precession in the transverse plane.

The flip angle α can be calculated as Equation 2.9 (Figure 2.2)

$$\alpha = \gamma \int_0^t B_1(\tau) d\tau \quad \text{Eq. 2.9}$$



(Hyperpolarized noble gas MRI laboratory, department of radiology, Harvard medical school)

Figure 2.2 The effect of an RF pulse on M_z . α is the flip angle. ϕ is the phase of the transverse magnetization.

Relaxation

In MRI, relaxation represents the signal decrease with time. In other words, relaxation describes how quickly spins become randomly aligned from the originally oriented status after excitation. This ordered to chaos process can be described in two separate processes, each with their own time constants. T_1 relaxation describes the spins that align back to the longitudinal direction. T_2 describes how the spins disperse in the transverse plane. Depending on the characteristic of the materials T_1 can vary from hundreds to thousands of milliseconds while T_2 varies from tens to hundreds of milliseconds.

$$M_z(t) = M_{z,eq}(1 - e^{-\frac{t}{T_1}}) + M_z(0)e^{-\frac{t}{T_1}} \quad \text{Eq. 2.10}$$

$$M_{xy}(t) = M_{xy}(0)e^{-\frac{t}{T_2}} \quad \text{Eq. 2.11}$$

In an idealized homogeneous magnetic field, all spins precess with the same frequency. However, in real systems, there are minor differences in the local environment, which causes deviation from the ideal. This deviation contributes to spin dispersion in the transverse plane. In fact, this disturbance can dominate and result in spin dephasing in a much faster manner. The corresponding transverse relaxation time constant is often referred to as T_2^* , which is usually much smaller than T_2 .

Since spins in different tissues return to its equilibrium state after excitation by the independent processes, T_1 and T_2 value varies among different tissue types. One distinct benefit is that image contrast between these tissues can be generated and used to distinguish different anatomical structures or pathologies. T_1 weighted images are widely used to study the cerebral cortex, identifying fatty tissue in the abdomen, characterizing myocardial fibrosis in contrast enhanced MRI. T_2 weighted images are

useful for detecting edema, white matter lesions in the brain, and cancer in prostate peripheral zone.

Gradient Fields

In order to create spatial frequency difference for spins at different locations, three gradients are placed on the x, y, and z directions. These gradients vary linearly within a certain range and play an important role in generating spatial frequency encoding of the MR signals. By applying gradients, spins in different spatial locations can have different precessional frequencies and therefore can be identified by detection of that frequency. This process is called spatial encoding. These gradients are generated by large coils placed near the bore of MRI scanners and are often accompanied by loud acoustic noise. There is one point in 3D space where the sum of the gradients in the three directions equals zero. This is called the isocenter of the main magnetic field and is often used as the origin in the 3-dimensional coordinate system. We can define the gradient field as:

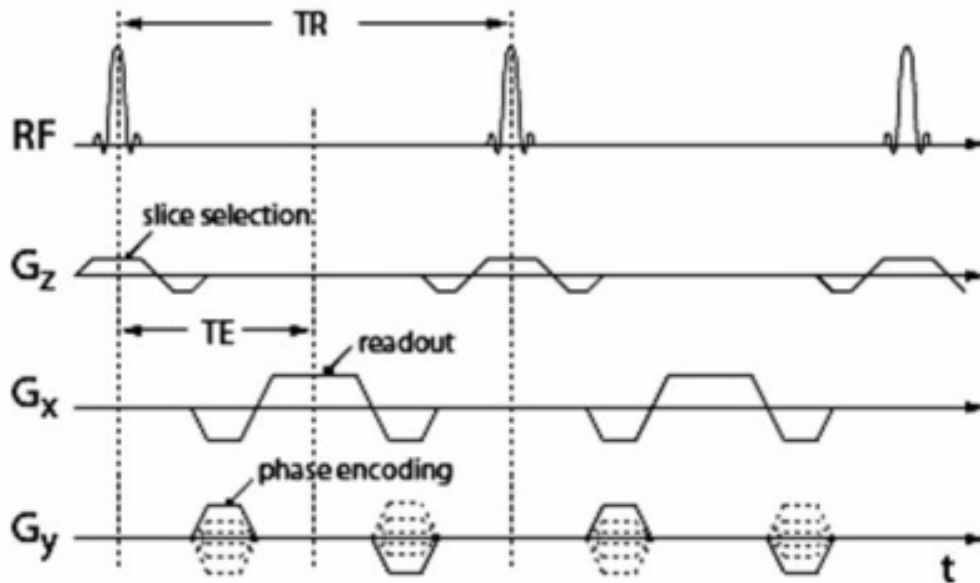
$$G = \frac{\partial B_z}{\partial x} i + \frac{\partial B_z}{\partial y} j + \frac{\partial B_z}{\partial z} k \quad \text{Eq. 2.12}$$

Unlike the main magnetic field, the gradients can be switched on or off while scanning. Typical gradients have trapezoidal or triangular shapes, which provides enough time to ramp up to a higher value or ramp down to zero. The maximum rate that the gradient can increase is called slew rate (G/cm/s).

Spatial frequency encoding

In three-dimensional space, spatial information can be distinguished by allocating different precession frequency for spins at different locations. In MRI, the signal in the frequency domain forms what we called Fourier space or k-space. The original image can be recovered by taking an inverse Fourier transformation of the k-space data. To be convenient we use previously defined x,y,z coordinate system as an example. To simplify the problem we use Cartesian coordinate system as our sampling scheme and define the z-axis as the slice-selection direction that can be encoded by a slice selection gradient. The x- and y-axes are defined as frequency encoding and phase encoding directions.

To select an imaging slice, both a spatially selective RF pulse and a slice-selection gradient can be used. The RF pulse commonly has a truncated sinc-shaped pulse, which can be used to excite a slice with a certain bandwidth. This is because the Fourier transform of a sinc pulse gives a rectangular shaped profile. The RF pulse bandwidth and the amplitude of the slice selection gradient controls the slice thickness. However the slice selection gradient also creates a linear phase dispersion along the slice direction, which leads to signal loss. To compensate for that a rephasing gradient is usually applied to eliminate the phase dispersion afterwards. (Figure 2.3)



(Matthias W. Seeger. School of computer and communication sciences, Ecole Polytechnique Fédérale de Lausanne)

Figure 2.3 MRI pulse diagram

The phase encoding gradient (G_y) defines the row information in a k-space and the amplitude of G_y varies between different repetition times (T_r), which correlate with the different lines in k-space (Figure 2.3). Although G_y is typically trapezoidal in shape it can potentially be changed to other shapes. As long as the integral of G_y does not change the k_y line number remains the same.

The frequency encoding gradient, which is called readout gradient, is often used to readout single lines of the MRI signal (Figure 2.3). Unlike the phase encoding gradient, the frequency encoding gradient does not usually change between different TRs. There is usually a pre-phase lobe in G_x before the data acquisition to prepare the transverse

magnetization and generate an echo signal. In a simple 2D Cartesian sampling case, G_x collects information along k_x direction. (Figure 2.4)

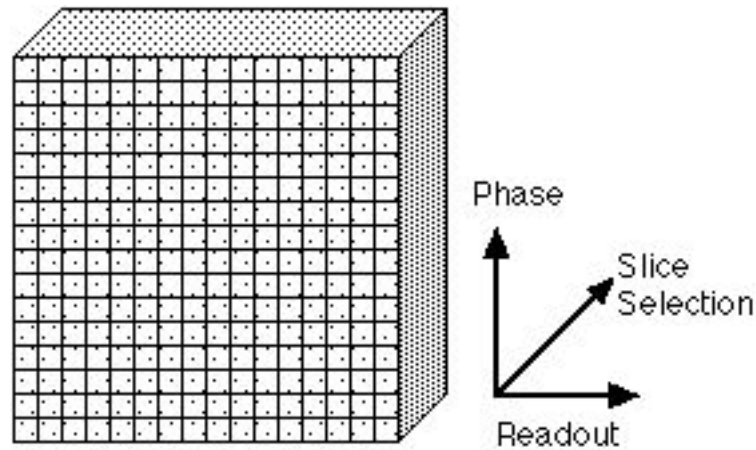
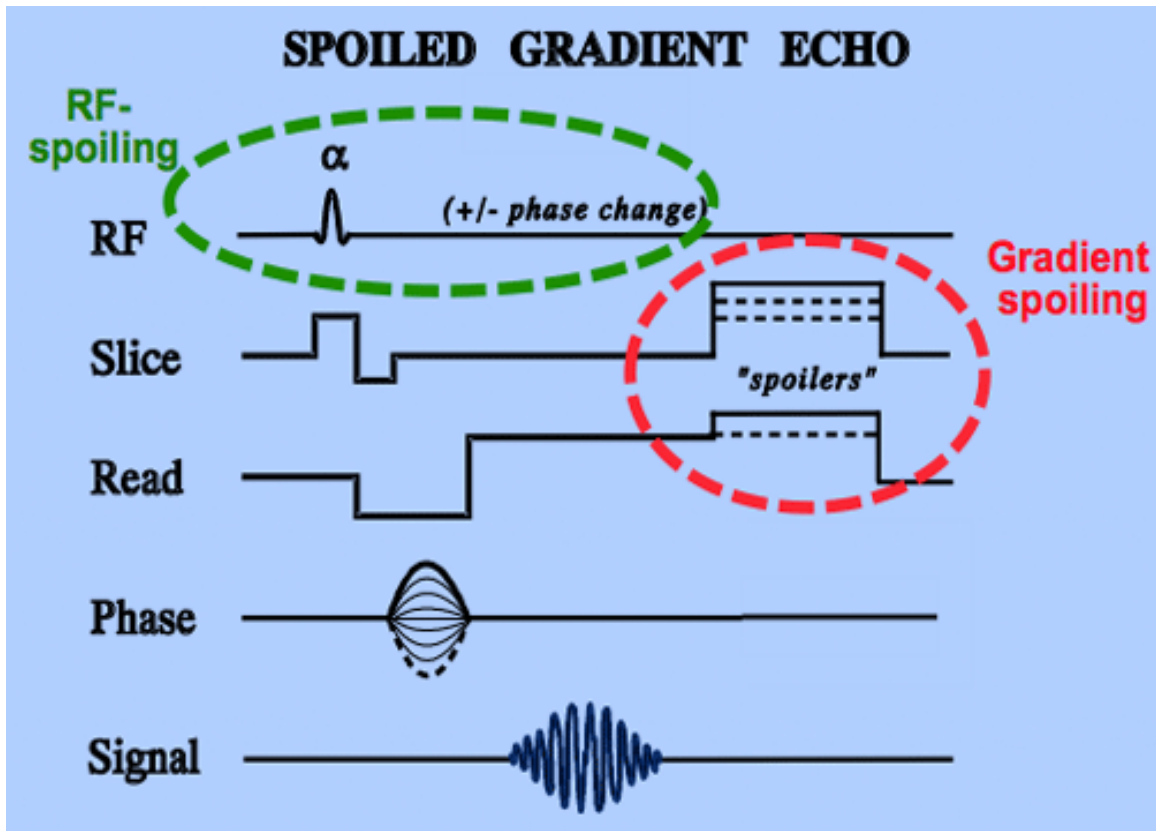


Figure 2.4 k-space diagram

Gradient Recalled Echo Imaging

There are many ways to generate MRI signals and form images using different RF pulses and gradients. More information can be found in *Bernstein et al.*'s "Handbook of MRI pulse sequences" (39). One of the most commonly used sequences is the Spoiled Gradient Readout Echo (SPGR) sequence (Figure 2.5). This sequence and the modified tagging sequence are mainly used in later chapters.



(Allen D. Elster. Division of Radiologic Sciences. Wake Forest School of Medicine)

Figure 2.5 Pulse sequence diagram of spoiled gradient readout echo imaging.

First, an RF pulse with flip angle of α is played together with slice select gradient. This excites spins within a certain slice thickness. A rephasing gradient followed right after the end of RF pulse aligns all the spins in z-direction. Then, a phase encoding gradient creates a linear spatial phase variation along the k_y direction. The overall effect is to encode spatial information orthogonal to the frequency encoding direction allowing the encoding of different k_y lines. A frequency encoding gradient usually has a short prephasing lobe, which prepares the transverse magnetization followed by a long readout gradient with the opposite polarity. The echo peak is formed when the area below the pre-phaser gradient is equal to the area below the

readout gradient lobe(38,39). Usually the integral of the prephasing gradient equals half of the integral of the readout gradient. A large amplitude gradient spoiler is added at the very end of the TR to help dephase the remaining transverse magnetization in a short period of time. The echo signal is received by the receiver coils, which are placed around the subject. The signal is sampled at regular time intervals, Δt , which is also called the dwell time and is the inverse of the readout bandwidth. The signal undergoes an analog to digital convert (ADC) and is eventually stored on a computer.

In this example different ky lines are acquired with different phase encoding gradient steps. The total time to acquire one ky line is called the repetition time (TR). The phase encoding gradient varies between each TR until all ky lines are acquired. Then the k-space data for the whole 2D image has been collected. In some cases not every ky line in k-space is acquired with the idea of shortening the total acquisition time. The missing k-space data is recovered later by using different techniques. The common part of these under sampling scheme is that the center part of k-space, which corresponds to the overall shape and image intensity information, is fully sampled. The outer edge part of k-space, which corresponds to edge sharpness of the anatomical image, is under sampled.

In practice, the 2D image is actually made up of different voxels where each voxel has three dimensions. The spatial size of the image in x and y directions is governed by the Field Of View (FOV). The depth of the voxel is associated with the slice thickness. The signal amplitude from each voxel corresponds the pixel intensity in a 2D gray scale magnitude image. Signal to noise ratio (SNR) of the image is used to describe the overall image quality and is governed by Equation 2.13 (38):

$$SNR \propto \left(\frac{FOV_x}{N_x} \frac{FOV_y}{N_y} \Delta Z \right) \sqrt{\frac{N_x N_y N_{avg}}{BW}} \quad \text{Eq. 2.13}$$

FOV indicates the field of view in different directions, N_x and N_y represent the number of frequency and phase encoding steps, Δz is the slice thickness, N_{Avg} is the average number of times imaging has been performed, and BW is the receive bandwidth.

Cardiac MRI Segments and ECG Triggering

Overall MRI is a slow imaging modality, which suffers from low SNR and motion. Especially in cardiac MR imaging, the heart has motion from both cardiac contraction and respiratory movement, which will cause image blurring. Cardiac motion can be solved by so-called segmented imaging, which is synchronized to the heart's rhythm with ECG triggering. For each heartbeat, k-space is divided into different segments. Each segment acquires part of the required k_y lines. Different k_y lines are then filled up with several consecutive heartbeats and a series of images is acquired (Figure 2.6). The data is combined such that each image is composed of multiple lines collected during each segment. These images can form a movie, which is called CINE image series that describe the cardiac contraction of a typical heartbeat. The number of images within one heartbeat represents different cardiac phases. Temporal resolution is defined by the repetition time of the pulse sequence times the number of k_y lines collected per segment (39,40).

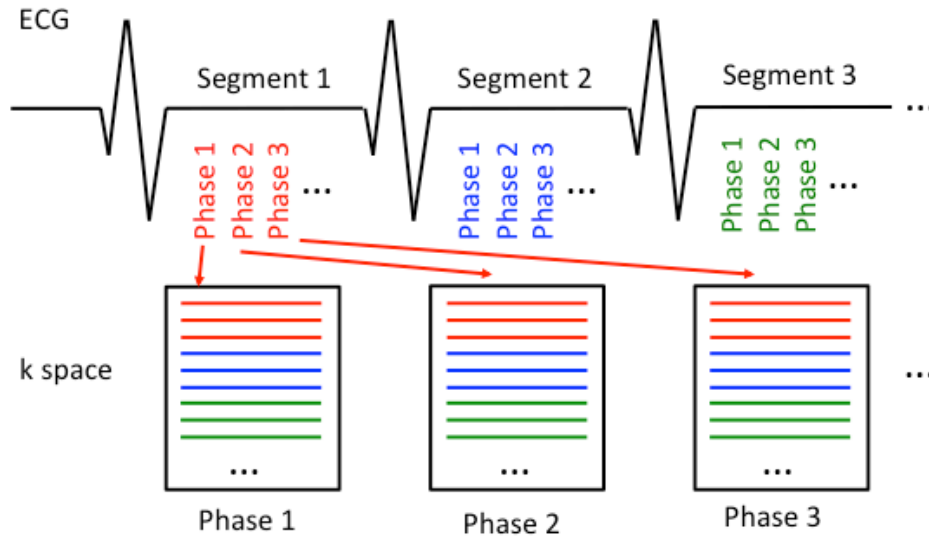


Figure 2.6 Diagram of a segmented MRI scheme. There are multiple images representing multiple cardiac phases obtained within one heartbeat.

As introduced in the first chapter, the ECG signal interprets the electrical activity of the heart during the cardiac cycle. The prominent waves of an ECG are called the QRS complex. In particular the R wave, which represents ventricular depolarization, has the highest peak on the waveform. By detecting the peak of R-wave, the ECG signal can be used to trigger the MRI acquisition between different heartbeats. This process is called cardiac triggering (40). By using this segmented scheme and cardiac triggering a cardiac CINE image series can be acquired without motion corruption.

Breath-Held Imaging and Respiratory Gating

Another predominate motion component is caused by diaphragm movement during respiration. It has been reported that the movement distance of the diaphragm during breathing is 16 ± 1.9 mm in the supine position and 12 ± 1.9 mm in the prone position

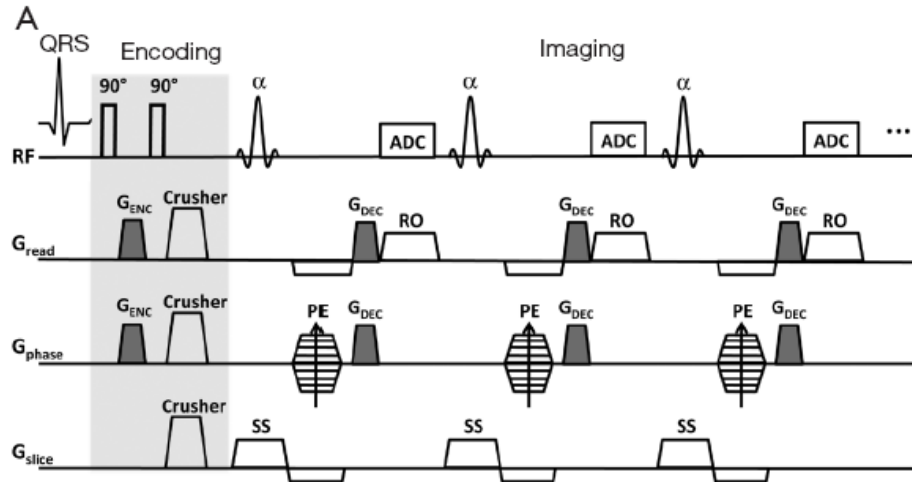
(41). In cardiac MRI respiratory motion causes undesirable image blurring and motion artifacts. In clinical protocols, the most commonly used method to suppress respiratory motion is to ask the subject to hold the breath during the scan. This technique is powerful unless the imaging sequence is too long and surpasses the breath hold limit of the subject. Another free breathing method is respiratory gating, which has similar idea as segmented k-space imaging with ECG triggering. There are many techniques that extract different information that can be used for gating purposes. For example, the navigator sequences are a common method in which a navigator RF pulse is used to excite a narrow column of spins and is usually placed at the interface between the liver and the lung. Similar to the cardiac phases defined by ECG signal gating, respiratory phases are determined by tracing the position of the diaphragm. MRI data is combined from multiple respiratory cycles, thus providing a consistent heart position and allowing free-breathing during the scan(39), but necessitating longer total acquisition times.

Another frequently used free breathing method is respiratory bellows gating. The bellow is a pressure sensitive device, which is placed over the abdomen of the scanning subject. Air pressure changes in the lung between inspiration and expiration has a direct relationship with abdominal movement(42), which is sensed by the bellows transducer and converted into a respiratory waveform used for image acquisition. This minimizes motion artifacts in the images from free breathing(39).

Cardiac Tagging

While it is very important to study the cardiac contraction and especially the its dysfunction, it is difficult to track the myocardium, which appears relatively

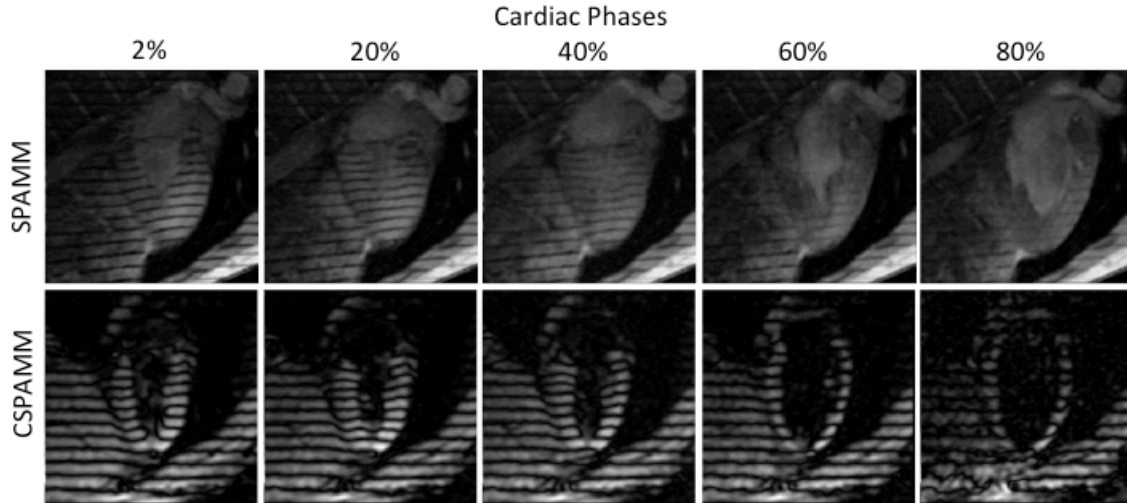
homogeneous in CINE cardiac MRI images. The cardiac tagging technique, which generates stripe or grid landmarks on the myocardium, can be used to visualize and measure cardiac movement. SPAtial Modulation of Magnetization (SPAMM) (43) tagging is the most commonly used tagging technique in clinical and research exams. The pulse sequence can be divided into a tagging preparation step and an imaging step. For example, in Figure 2.7, the tag preparation steps starts with the combination of playing a 90° RF pulse followed by gradients in the readout (x) and phase encoding (y) directions and followed by another 90° RF pulse. The first RF pulse tips the bulk magnetization into the transverse plane. Next, the gradient produces the desired spatial pattern by dephasing the bulk magnetization vector. The second RF pulse rotates the dephased spins back into the longitudinal plane. Crusher gradients eliminate the remaining signal in transverse plane and the longitudinal magnetization M_z is now spatially modulated. The imaging step uses the same scheme as SPGR sequences described above where longitudinal magnetization is tilted into transverse plane to generate numerous echoes. Voxels with high M_z signal correspond to the untagged region and voxels with low M_z signal corresponds to the tag lines (Figure 2.7).



(Kai Jiang et al. Quant Imaging Med Surg. 2014 Oct;4(5):345-57)

Figure 2.7 Pulse sequence diagram of the preparation pulse for Spatial Modulation of Magnetization (SPAMM) cardiac tagging sequence.

Due to T_1 relaxation effects, tag contrast last only for several hundred milliseconds (44). Complementary SPATial Modulation of Magnetization (CSAPMM) was introduced by Fischer *et al.* (45) to enhance tag contrast and increase the apparent tag persistence. The combination of CSPAMM with the ramped imaging flip angle technique can maintain uniform tag contrast throughout the different cardiac phases. (Figure 2.8) More details can be found in Chapter 3.



(This image is courtesy of Dr. Daniel B. Ennis *et al.*)

Figure 2.8 SPAMM (left) and CSPAMM (right) of the heart in long axis view.

The ramped imaging flip angle can be calculated using the following recursive formula(46):

$$\alpha_{k-1} = \alpha \tan \left(\sin(\alpha_k) e^{\frac{-\Delta t}{T_1}} \right) \quad \text{Eq. 2.14}$$

where α represents the flip angle, k represents the cardiac phase number, Δt indicates the duration of time between the RF imaging pulses, and T_1 indicates the relaxation time of myocardium (~ 1050 ms at 1.5T). It has been shown that for short repetition times and cardiac T_1 values, $\alpha_k = 21^\circ$ produces the best contrast (46).

Chapter 3 Complementary Radial Tagging for Improved Myocardial Tagging

Contrast

Cardiac magnetic resonance imaging is a proven technique for the evaluation of myocardial structure and function. In particular, MRI tagging can be used to non-invasively generate tissue landmarks, which facilitate the qualitative and quantitative assessment of left ventricular (LV) myocardial deformation in both research and clinical settings (43,47). The first demonstration of myocardial tagging by Zerhouni *et al.* (47) employed radial saturation bands. Therein, several thin tagging planes were generated perpendicularly to the imaging plane. During imaging, the tagging planes appear as dark lines within the imaging plane and the tag pattern deformation reflects the underlying myocardial motion. This method of tag generation was surpassed by Cartesian line or grid tagging patterns, which can be generated by SPAtial Modulation of Magnetization (SPAMM) (43). T_1 relaxation effects, however, contribute to tag fading, which typically result in the tags only being detectable for the first ~500ms of the cardiac cycle at 1.5T(44). Complementary SPAtial Modulation of Magnetization (CSAPMM) was introduced by Fischer *et al.* (45) to enhance tag contrast and increase the tag persistence in late cardiac phases.

Recently, Nasiraei-Moghaddam *et al.* (48) developed a new pulse sequence, which uses time-varying sinusoidal-shaped RF pulse and gradients to generate radial tags efficiently. Whereas previous radial tagging techniques used multiple discrete RF pulses within a relatively long tag preparation time, this radial tagging sequence uses continuous RF pulses and gradient waveforms. Due to the contribution of both on-

resonance excitation and off-resonance excitation, this radial tagging method has lower Specific Absorption Rate (SAR) and can be generated in a shorter period of time compared to previous radial tagging sequences.

Radial tagging patterns have the potential advantage of better conforming to the annular geometry of the LV in the short-axis view, but no radial tagging technique has been presented that produces contrast similar to CSPAMM. Hence, in this study we define the principles that govern combining the CSPAMM concept with radial tag encoding to create complementary radial tags (CRT); demonstrate left ventricular (LV) short-axis (SA) images acquired in healthy subjects; and discuss the requirements for obtaining high quality CRT images. The in vivo tag contrast is also compared with theoretical simulation results. Furthermore, with the CRT technique used herein the scanner table is translated to an optimal table position relative to the isocenter of the main magnetic field to improve the uniformity of the radial tag pattern. Lastly, we use the Cardiac Atlas Project (49) to retrospectively calculate the optimal table position of LV SA images from a large population of patients and demonstrate that the new CRT technique can be used in the majority of clinical cases.

Theory

Complementary Radial Tagging

We combine the principle of CSPAMM (45) with the radial tag encoding technique (48) to generate CRT images. Two series of RT images are encoded to generate phase shifted tag patterns followed by a spoiled gradient (SPGR) imaging sequence. The pixel intensity in a RT image can be expressed by the sum of the image contrast profile

(I_{image}) and the tag contrast profile (I_{tag}) (5). The tag profile is more easily expressed in polar coordinate system with the tag center as the origin, r as radius, θ as the polar angle and t as time

$$I_{\text{total}}(r, \theta, t) = I_{\text{image}}(r, \theta, t) + I_{\text{tag}}(r, \theta, t) \quad \text{Eq. 3.1}$$

Two RT image sets have the same I_{image} ($I_{\text{image},1} = I_{\text{image},2}$). The subtraction of two RT image sets generates CRT images that contain only tag information.

$$I_{\text{total},1}(r, \theta, t) - I_{\text{total},2}(r, \theta, t) = I_{\text{tag},1}(r, \theta, t) - I_{\text{tag},2}(r, \theta, t) \quad \text{Eq.3.2}$$

Two series of images are acquired with the same RF pulse, but sinusoidal gradients with different phases. The requisite phase shift (φ) between the gradients is:

$$\varphi = \frac{\pi}{2N_{\text{tag}}} \quad \text{Eq. 3.3}$$

N_{tag} is the number of tag lines. Consequently, the two tag profiles exhibit similar, but rotated tag patterns:

$$I_{\text{tag},1}(r, \theta, t) = I_{\text{tag},2}(r, \theta + \varphi, t) \approx -I_{\text{tag},2}(r, \theta, t) \quad \text{Eq. 3.4}$$

The two tag profiles have opposite signs and the tag contrast is therefore enhanced after subtraction.

$$I_{\text{total},1}(r, \theta, t) - I_{\text{total},2}(r, \theta, t) \approx 2 I_{\text{tag},2}(r, \theta, t) \quad \text{Eq. 3.5}$$

Due to T_1 relaxation tag contrast gradually decreases and eventually becomes 0. Further application of ramped imaging flip angle scheme on CSPAMM (45) images generate constant tag contrast throughout the entire cardiac cycle. In this study, VFA technique is also accommodated during imaging acquisition steps.

We use five half-sinusoid lobes for the RF pulse to generate a total of ten intersections with the LV and twenty CRT line intersections after subtraction (Figure

3.1). RF pulse not only excites the spins in the on-resonance plane to form a radial tag line, but also contributes to circumferential adjacent lines, which sharpens the tag profile and leads to lower SAR of the preparation sequence compared to Zerhouni's methods. Also note that the CRT approach requires fewer lobes compared to Nasiraei-Moghaddam's method to achieve the same number of tags.

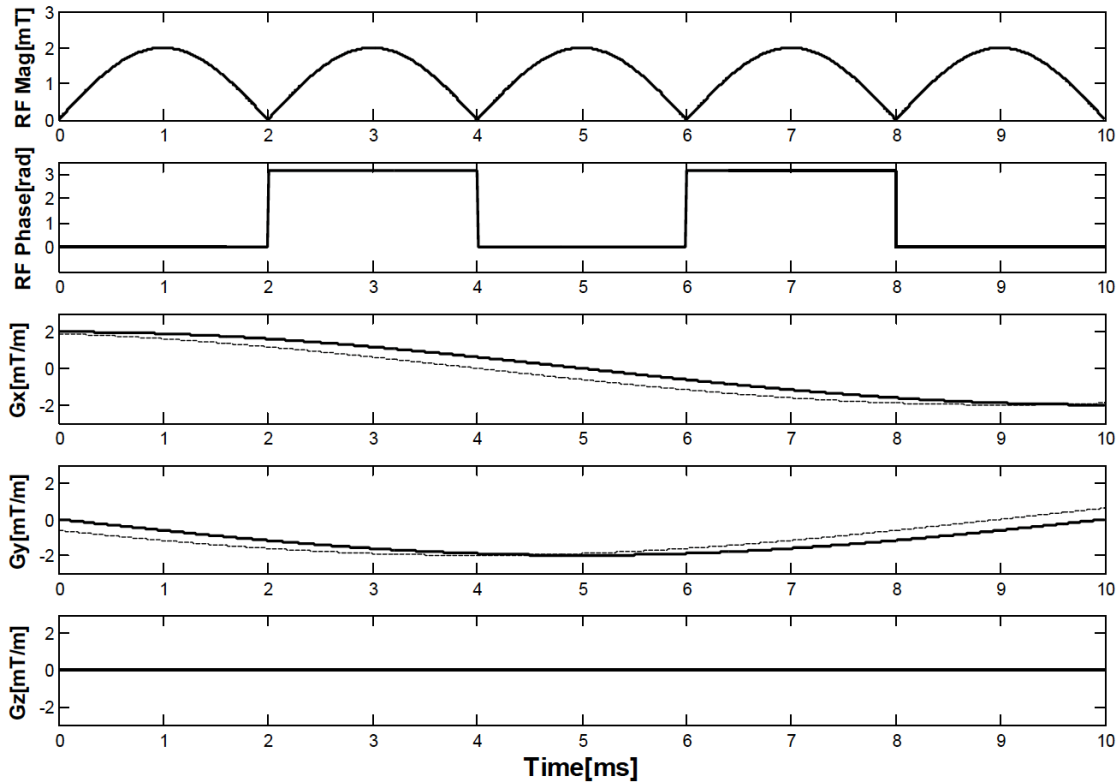


Figure 3.1: RF pulse (magnitude and phase) and gradient waveforms for the complementary radial tagging pulse sequence. Sinusoid-shaped gradients generate one set of radial tags (solid line), while phase-shifted G_x and G_y gradients (dashed line) generate the complementary set of radial tags. The five sinusoidal lobes in the RF pulse create five radial tagging lines and ten radial tags intersections with the left ventricular wall. The number of tag intersections doubles again after CRT image subtraction.

Optimal Table Position

RT technique uses a combination of sinusoidal gradients and RF pulse envelopes to select an on-resonance plane, which rotates about the applied gradient direction (\mathbf{g} , unit vector, Figure. 3.2). The hardware design for modern MRI machines requires \mathbf{g} pass through the iso-center (O) of the main (B_0) magnetic field. The intersection of \mathbf{g} on the imaging plane defines the location of the radial tag center (C_{tag}). In general, the imaging plane can be described by a normal vector (\mathbf{n} , unit vector), which can be selected independent of \mathbf{g} .

Once a subject is positioned inside the MR scanner, the LV short-axis plane's normal vector (\mathbf{n}) is defined relative to the scanner's coordinate system. If the angle (α) between \mathbf{n} and \mathbf{g} is minimized, then the intended radial tag pattern is generated, but the center of the radial tagging pattern is not guaranteed to coincide with the LV cavity center (C_{LV}) (Figure 3.2A). If, however, \mathbf{g} is chosen to point to C_{LV} , but is not coaxial with \mathbf{n} , then α is not be minimized. Consequently, tagging will be centered correctly ($C_{tag} = C_{LV}$), but with non-uniform profile (Figure 3.2B). The ideal radial tagging pattern is only generated when both \mathbf{g} and \mathbf{n} pass through C_{LV} , which requires: 1) \mathbf{g} and \mathbf{n} point to $C_{LV} = C_{tag}$. 2) minimizing the angle (α) between \mathbf{n} and \mathbf{g} (Figure 3.2B).

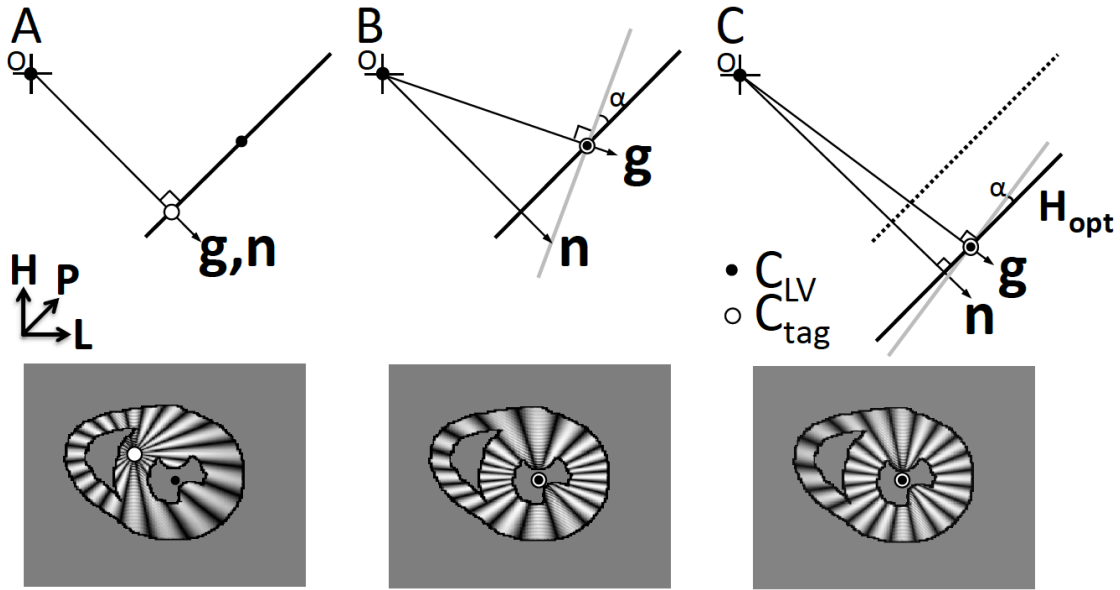


Figure 3.2: Optimization of the position of the LV short-axis imaging plane (thick black line) and orientation of the tagging plane relative to the B_0 isocenter (O) to achieve the uniform radial tag pattern for the LV short-axis. (A) Subsequent to landmarking the gradient direction (\mathbf{g}) used for tagging and the short-axis image plane normal (\mathbf{n}) coincide, in general, but the center of the tags (C_{tag}) may not be coincident with the center of the LV (C_{LV}). (B) \mathbf{g} is updated to pass through the center of the LV (C_{LV} coincides with C_{tag}) and the tagging pattern is uniform on the tagging plane (gray line), but not on the short-axis imaging plane. (C) Calculation of an optimal table shift ($H=H_{opt}$) is achieved by minimizing α , which results in \mathbf{g} intersecting C_{LV} and the optimum tagging pattern is generated on the short-axis imaging plane.

To satisfy requirement 1), C_{tag} is forced to coincide with C_{LV} by tilting the \mathbf{g} away from the image plane normal \mathbf{n} such that $\mathbf{g} = M_{rot} \cdot \mathbf{n}$ where M_{rot} is a rotation matrix

determined by the imaging plane parameters. This generates a projection of the radial tag pattern on the short-axis imaging plane (Figure 3.2B).

To satisfy requirement 2) The scanner table can be moved away from the iso-center to an optimal table position (H_{opt}) to improve the tag profile. As indicated in Figure 3.2C, at the new table position, a uniform tag pattern is generated on a new oblique plane with a smaller α .

The ideal tag profile can be achieved when $\alpha = 0^\circ$, however, the MRI scanner table can only be moved along the head-foot direction ($\pm H$ direction). In practice, for an arbitrary imaging plane in 3D space, α may only be reduced to a minimum, non-zero value.

$$H_{opt} = \operatorname{argmin} \langle \alpha \rangle \quad \text{Eq. 3.6}$$

The angle α between \mathbf{g} and \mathbf{n} and can be expressed as:

$$\alpha = \arccos (\mathbf{g} \cdot \mathbf{n}) \quad \text{Eq. 3.7}$$

Once the imaging slice is defined, the image normal \mathbf{n} is known:

$$\mathbf{n} = \begin{bmatrix} n_1 \\ n_2 \\ n_3 \end{bmatrix} \quad \text{Eq. 3.8}$$

\mathbf{g} can be derived if C_{tag} is equivalent to C_{LV}

$$\mathbf{g} = \frac{1}{\sqrt{L^2 + P^2 + H^2}} \begin{bmatrix} L \\ P \\ H \end{bmatrix} \quad \text{Eq. 3.9}$$

L (left-right), P (anterior-posterior) and H (head-foot) indicate the subject's C_{LV} relative to isocenter (O). Substitution of Equation 3.8 and Equation 3.9 into Equation 3.7 results in the following:

$$\alpha = \text{acos} \left(\frac{n_1 L + n_2 P + n_3 H}{\sqrt{L^2 + P^2 + H^2}} \right) \quad \text{Eq. 3.10}$$

n_1 , n_2 , n_3 , L , and P are fixed, while H remains the only variable. Take the derivative of Equation 3.10 and set it to zero. H_{opt} can be derived as:

$$H_{opt} = \text{argmin} \langle \alpha \rangle = \frac{n_3(L^2 + P^2)}{n_1 L + n_2 P} \quad \text{Eq. 3.11}$$

Methods

Complementary Radial Tagging Bloch Simulations

Radial tagging involves a highly nonlinear excitation of spins, wherein the pulse duration t , maximum RF amplitude $B_{1,max}$, maximum gradient amplitude G_{max} and N_{tag} contribute together to generate the radial tagging pattern (48). To better visualize and analyze the tagging pattern simulated results were generated with a Bloch equation simulator (<http://mrsrl.stanford.edu/~brian/bloch/>) using MATLAB (The MathWorks, Natick, MA).

LV CRT images in the SA plane were simulated with the $T_1=1000$ ms (9), $T_2=60$ ms (50,51) representing myocardium at 1.5T. The magnetization of the myocardium at thermodynamic equilibrium was set to one. Based on the average size of a normal human heart (52) an annulus of myocardium in the SA plane was defined with an inner diameter of 3cm and an outer diameter of 5cm. The following parameters were also used: 350mm×350mm FOV, 1.8mm × 1.8mm pixel spatial resolution, $B_{1,max} = 5\mu\text{T}$, $G_{max} = 10\text{mT/m}$ and total tag preparation duration of 10ms. The results were used to evaluate the tag pattern seen in Figure 3.2. Tag contrast ratio in RT and CRT simulations were calculated and compared with in vivo data in Figure 3.3.

Phantom Imaging Experiments

A stationary phantom was imaged using a 1.5T Siemens Avanto scanner (Siemens Medical Solutions, Erlangen, Germany). The phantom's T_1 value was measured to be ~970ms using spin echo inversion recovery. Similar to the traditional line or grid tag acquisitions, the CRT preparation module is played at the beginning of each cardiac cycle followed by SPGR imaging acquisition. This modified SPGR sequence with ECG triggering was used to acquire images with different α for comparison to the simulation result. Imaging parameters were: total tagging preparation duration=10ms, TE/TR=3.75/5.13ms, FOV= 250mm×250mm, receiver bandwidth=200 Hz/pixel, matrix size = 196×196, and 1.3mm × 1.3mm resolution with slice thickness = 6mm. External ECG trigger with RR interval of 1000ms. Image flip angle is set to be 12°.

In the first experiment, tag pattern was generated on an oblique plane with different projection angle α . In the second experiment, C_{tag} was moved away from the C_{LV} with different off-center shift L to test the sensitivity of the correct placement of C_{tag} relative to C_{LV} . In both experiments, the arc length (d) between two adjacent tag lines was calculated and reported as mean \pm standard deviation. The Coefficient of Variation (CV) is calculated as the standard deviation of d (d_{std}) divided by the mean of d (d_{mean}).

In Vivo Imaging Experiments

In accordance with institutional, state, and federal guidelines all subjects were informed about the potential risks and benefits of the study and asked to provide signed statements of informed consent prior to commencing the imaging studies. The local institutional review board approved this study.

The CRT sequence used in the phantom experiment was slightly modified to acquire in vivo images. The new sequence included automated table position adjustments based on Equation 3.11. In vivo images were acquired to demonstrate the CRT pattern in healthy volunteers (N=10, 2 females and 8 males; age 26.5 ± 2.4 years) with no previous history of cardiovascular disease. Volunteers were positioned headfirst and supine. Localizer sequences and functional cine images were first acquired to locate the apical, middle, and basal slices in the cardiac SA plane using a six-element anterior coil array and a six-element posterior coil array. Short-axis basal LV images were acquired at a basal position where the myocardium retains an annular shape for the entire cardiac cycle. Short-axis apical LV images were acquired at the most apical level wherein the blood pool was apparent for all cardiac phases.

The following imaging parameters were used: total tag preparation duration was 10ms, TE/TR=3.75/5.13ms, FOV= 300-350mm×300-350mm, receiver bandwidth=200 Hz/pixel, matrix size = 196×196, and 1.5-1.8mm×1.5-1.8mm resolution with slice thickness = 6mm. Twenty cardiac phases were acquired using 8 k_y -lines per segment for a temporal resolution of 41ms. A 12° constant imaging flip angle was used for the RT sequences to calculate the tag CNR and compared with tag contrast in simulation data. A ramped image flip angle with a final flip angle of 20° (46) was used for the CRT sequence to demonstrate the a rather uniformed tag contrast throughout the entire cardiac cycle. The acquisition window was adjusted to cover ~90% of the R-R interval for each volunteer. Parallel imaging with rate-2 GRAPPA (53) and $\frac{3}{4}$ partial Fourier imaging were used to reduce the total breath hold time to be 11-13 seconds and 22-26 seconds for the RT and CRT sequences respectively.

Both the phantom and in vivo CRT images were reconstructed offline using MATLAB. The CRT images were reconstructed by taking the complex difference of the two RT images for each cardiac phase.

Basal and apical LV SA tagged images were acquired from 10 healthy volunteers with Off Resonance Insensitive SPAMM (ORI-SPAMM) line tags (54) and CRT tags. LV twist from line and CRT tagged images was calculated using Fourier Analysis of STimulated Echoes (FAST) (55). LV twist was calculated as the rotational difference between apical and basal LV images (56) for each cardiac phase.

Tag contrast-to-noise ratio measurement

The tag contrast-to-noise ratio (T_{CNR}) for RT and CRT in vivo images were measured in a subset of 5 healthy volunteers. Small regions-of-interest (ROIs) were placed on the tagged and untagged myocardium. The ratio of T_{CNR} between RT and CRT images was calculated and compared to the tag contrast (T_C) ratio acquired from noise-free simulation results. T_C and T_{CNR} are defined(44):

$$T_C = (SI_{myocardium} - SI_{tag}) \quad \text{Eq. 3.12}$$

$$T_{CNR} = \frac{(SI_{myocardium} - SI_{tag})}{\sigma_c} \quad \text{Eq. 3.13}$$

where $SI_{myocardium}$ and SI_{tag} are the mean ROI signal intensities for the untagged and tagged myocardial tissue and σ_c is the noise standard deviation (SD) measured from the background ROI and corrected by Dietrich et al 's method (57).

Retrospective Analysis of Optimal Table Position Shifts

Though the hardware design varies among different MRI manufactures, the scanner table for modern MRI machines can only be moved within a limited range while maintaining image quality because of both the field homogeneity and the limits of gradient linearity. A previous study indicated images acquired out of this range ($\pm 100\text{mm}$) suffer from severe gradient non-linear distortion and the image quality can be affected dramatically (58). However, whether the optimal table position for a particular SA imaging slice falls within the gradient linearity range for most patients is unknown. Therefore, in order to evaluate the ability to acquire acceptable radially tagged images in clinical practice the optimal table position shifts for a large number of subjects was retrospectively evaluated using images from the Cardiac Atlas Project database (49).

We retrospectively evaluated the H_{opt} and α values for 500 patients and 1537 LV SA images obtained from the Cardiac Atlas Project database. Patient-specific image information was extracted from the DICOM header file of each image including the normal of the image plane (\mathbf{n}), the pixel spacing value (pixel/mm), and the top-left pixel location (L, P, H). C_{LV} was manually identified for each image and transformed to scanner coordinates using information in the DICOM header. The image normal vector (\mathbf{n}) was obtained from the cross product of the two unit vectors along the image edge directions. The optimal table position and corresponding α_{min} for each patient and each SA plane was then calculated according to Equation 3.11.

Results

T_C and T_{CNR} results

Figure 3.3A shows the tag contrast (T_C) as a function of time for RT with Constant Flip Angle (CFA), CRT with CFA, and CRT with Ramped Flip Angles (RFA) from simulations. Fig. 3B shows the mean T_{CNR} measured from in vivo images (N=10). The simulation results show that the CRT+RFA maintains a constant T_C throughout the cardiac cycle. For the in vivo CRT measurements, subtraction of two image sets reduced the noise SD and further increased the T_{CNR} by a factor of about $\sqrt{2}$ compared to the RT sequence.

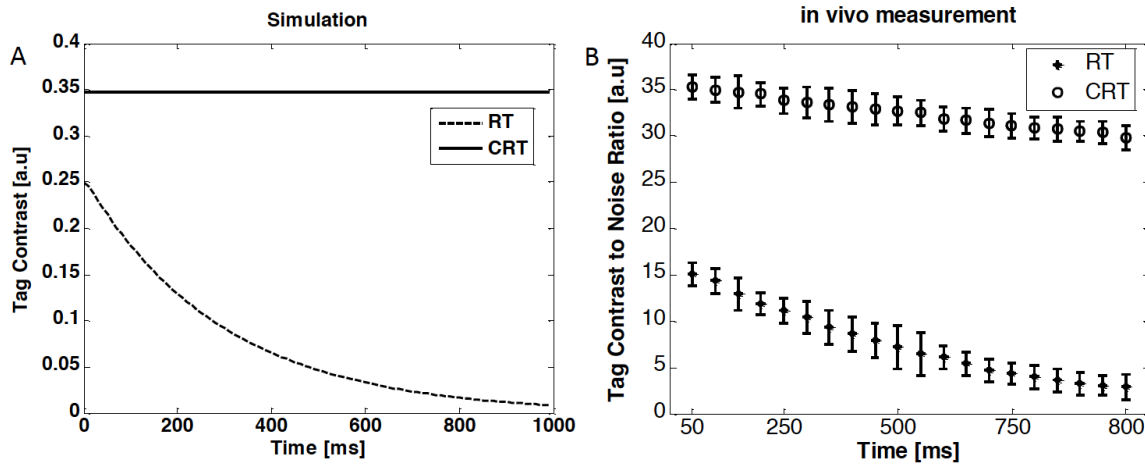


Figure 3.3: A. Tag contrast in RT+CFA (dashed), CRT+CFA (dash dotted) and CRT+RFA (solid) images was calculated from simulation data. B. Tag contrast to noise ratio was measured in RT+CFA (dashed), CRT+CFA (dash dotted) and CRT + RFA (solid) in vivo images from 10 healthy volunteers. Error bars reflect the standard deviation for each cardiac phase.

In vivo images

Figure. 3.4 shows the CRT images at different table positions acquired in a healthy subject at ~40% of the cardiac cycle. Fig. 4A shows the non-uniform CRT pattern acquired 60mm away from the optimal table position. The tag pattern improves as the table position approaches H_{opt} ($\Delta H = 0$) (Figure. 3.4B). The best CRT pattern is achieved when imaging at H_{opt} (Figure. 3.4C) and degrades beyond H_{opt} (Figure. 3.4D-E).

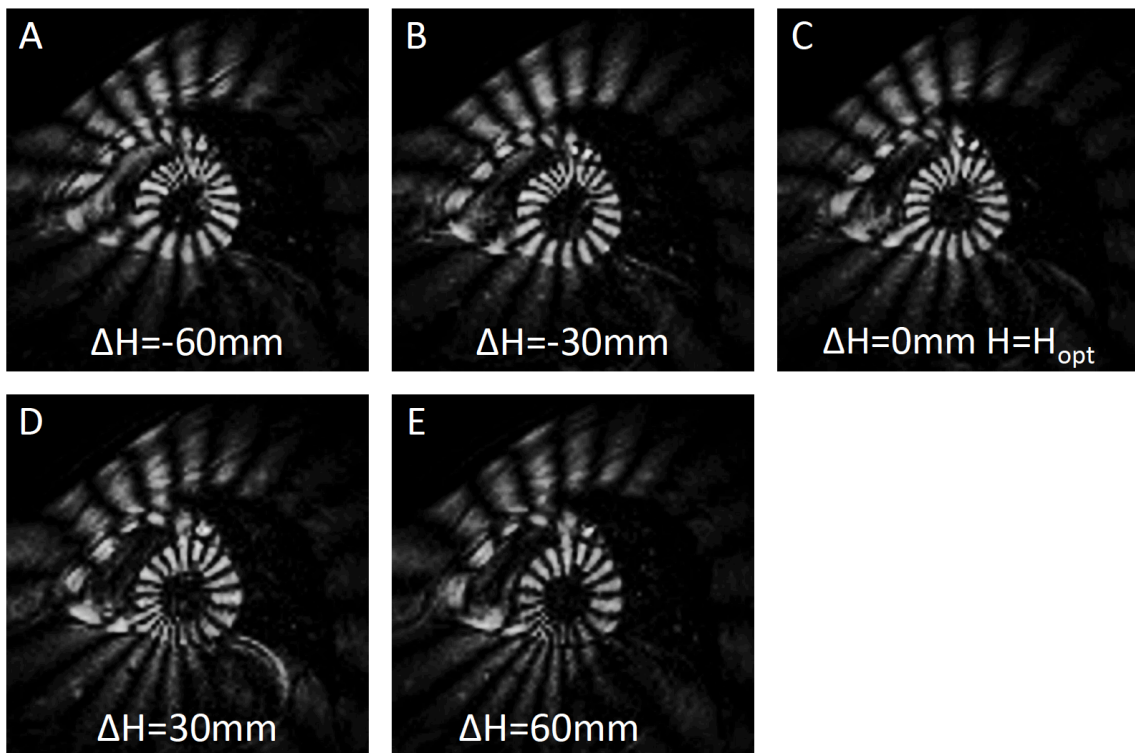


Figure 3.4: Complementary radial tagging images acquired with a range of non-optimal table position shifts. ΔH (mm) is defined as the table shift away from the optimal position. Note the tag pattern improvement in C where $\Delta H = 0\text{mm}$ and $H = H_{opt}$.

Figure 3.5 shows a comparison of the RT and CRT tag contrast different cardiac phases. LV SA images were acquired at the apical and basal levels. The dense tagging pattern combined with flowing blood results in the loss of tag information inside the LV cavity during all cardiac phases for both techniques. Additional blood pool suppression in the CRT images results from image subtraction. CRT technique combined with ramped imaging flip angle is used to obtain rather uniform tag contrast throughout the entire cardiac cycle. The tags in the radial tagging images start to fade and become more difficult to observe in late cardiac phases, while the tag contrast is relatively preserved in the CRT images. Note also, that due to tag fading in tissues outside the heart there is significant background tissue suppression in CRT, which aids visualization of cardiac function.

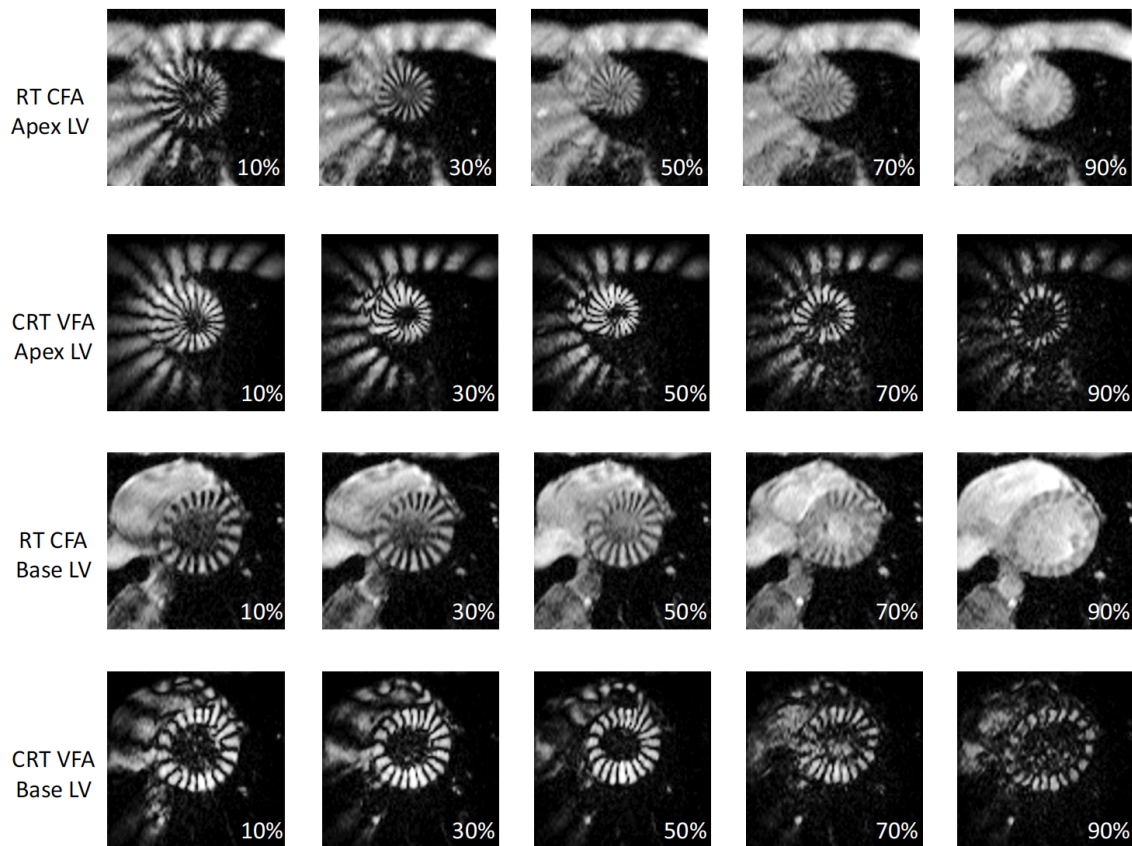


Figure 3.5: Comparison between RT images and CRT images in a healthy

human subject. For RT and CRT images, apical and basal LV images in the SA view are annotated as RT Apex, CRT Apex, RT Base and CRT Base. The tag lines fade in RT images, but retain higher contrast in the CRT images, especially in the later cardiac phases.

Phantom Analysis

Equation. 11 shows in some cases, α can be only minimized to a non-zero value. However, if α_{min} remains very large the tag profile is still significantly affected. The CRT profiles acquired in a stationary phantom with different projection angles are shown in Figure. 3.6A. The white circle indicates the approximate LV myocardial position in a SA image. Results are reported in Table 3.1.

Projection Angle						
α (°)	0	10	20	30	40	50
d (mm)	6.7± 0.1	6.7± 0.3	6.7± 0.6	6.8± 1.3	6.8± 2.0	6.8± 2.8
CV	1%	4%	9%	20%	30%	41%
Off-center Distance						
L (mm)	0	2	4	6	8	10
d (mm)	6.7± 0.1	6.7± 0.5	6.7± 0.9	6.7± 1.4	6.7± 1.8	6.7± 2.3
CV	1.5%	4.5%	9.0%	20%	27%	34%

Table 3.1: Measured distance between adjacent radial tag lines for a range of projection angles (α) and off-center distances (L) of the radial tags' center (CV: coefficient of variation).

The in-plane image resolution for CRT in vivo images was 1.5-1.8mm x 1.5-1.8mm. Images with $\alpha \leq 30^\circ$ have excellent tag profiles that are only subtly different from the ideal

uniform tag profile ($CV \leq 20\%$, $d_{std} < 1$ pixel). For $30^\circ < \alpha \leq 40^\circ$ the tag profiles are affected, but still qualitatively acceptable ($CV \leq 30\%$, $d_{std} \approx 1$ pixel). When $\alpha > 40^\circ$ a distinguishable pattern of more closely and more distantly spaced tags is apparent ($CV > 30\%$, $d_{std} > 1$ pixel). Based on these images we conclude that $\alpha \leq 30^\circ$ produces an excellent tag pattern, while $\alpha \leq 40^\circ$ produces an acceptable tag pattern, but $\alpha > 40^\circ$ produces an unacceptable tag pattern.

In Figure 3.6B C_{tag} was moved away from C_{LV} with different off-center shifts L , d is calculated for each L in Table 1. When the C_{tag} doesn't coincide with C_{LV} we find that $d_{std} 1.4$ (< 1 pixel) and the $CV \leq 20\%$ if $L < 6$ mm and that the tag pattern is more variable for $L > 6$ mm.

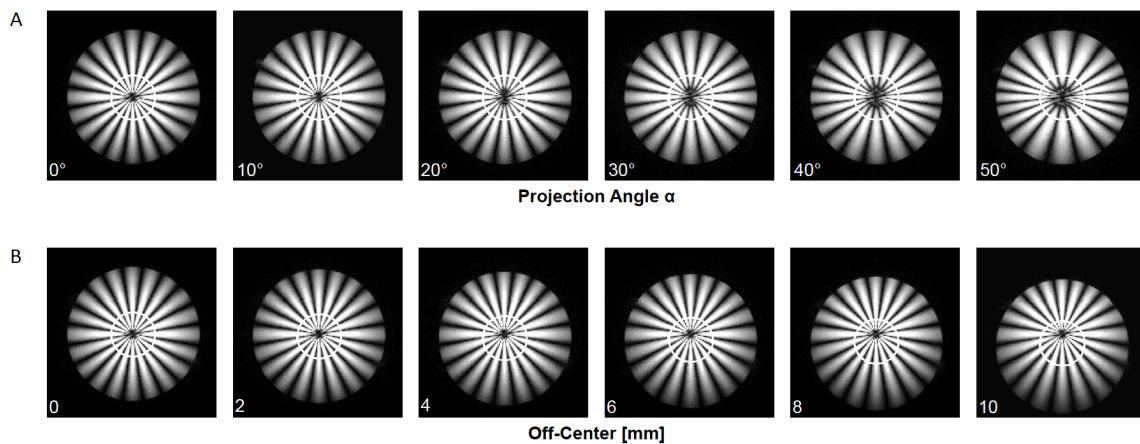


Figure 3.6: A. CRT images with different projection angles α (0° 10° 20° 30° 40° 50°) were acquired in a stationary phantom. B. CRT images with the tag center moved away from the LV cavity by a distance L (0mm 2mm 4mm 6mm 8mm 10mm). The white circle indicates the approximate myocardium location in LV short-axis image.

Retrospective Analysis

Figure. 3.7 shows a two-dimensional histogram from the retrospective analysis of patients (N=500) in the Cardiac Atlas Project database. The x-axis shows the absolute value of the optimal table position ($|H_{opt}|$) and the y-axis shows the corresponding minimum projection angle (α_{min}). Analysis of the 2D histogram demonstrates that 90% (1383/1537) of the clinical cases fall within $\alpha_{min} \leq 30^\circ$ and $|H_{opt}| \leq 55\text{mm}$ (Figure. 3.7 solid white line), which should produce an excellent CRT pattern. An acceptable tag pattern can be generated in 99% (1521 of 1537) of the clinical cases (Figure. 3.7 dashed white line) when $\alpha_{min} \leq 40^\circ$ and $|H_{opt}| \leq 70\text{mm}$.

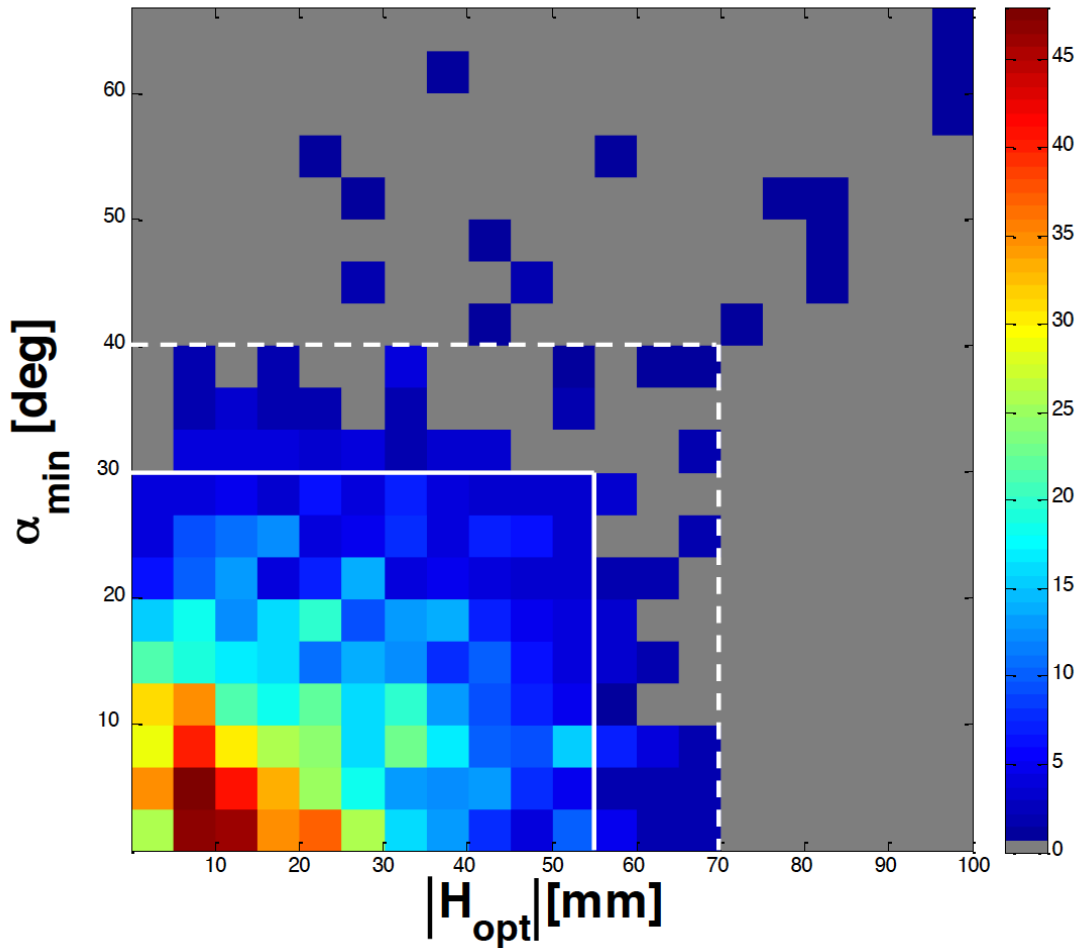


Figure 3.7: Two-dimensional histogram of the optimal table position shift ($|H_{opt}|$) and minimum projection angle (α_{min}) for 1537 short-axis images retrospectively

analyzed from patients (N=500) in the Cardiac Atlas Project database. A cut-off of $|H_{opt}|$ is applied. $\alpha_{min} \leq 30^\circ$ and $|H_{opt}| \leq 55\text{mm}$ (solid white line) indicates 90% clinical cases could have been imaged with an excellent radial tagging profile. $\alpha_{min} \leq 40^\circ$ and $|H_{opt}| \leq 70\text{mm}$ (dashed white line) indicates 99% clinical cases would have an acceptable radial tagging profile.

LV Twist Analysis

Figure 3.8 demonstrates the LV twist measurement using the FAST method for ORI-SPAMM line tagged and CRT tagged images in 10 healthy volunteers. t-test between the two measurement results show no statistical differences ($p=0.28$). Linear regression results in a correlation coefficient of $r = 0.99$. Figure 3.9 shows the Bland-Altman analysis with a measured bias of -0.13° and a 95% confidence interval of $\pm 0.98^\circ$. There are small apparent differences in mid-diastasis and late diastolic phases between the two tagging methods compared with the subtle apparent differences during systolic.

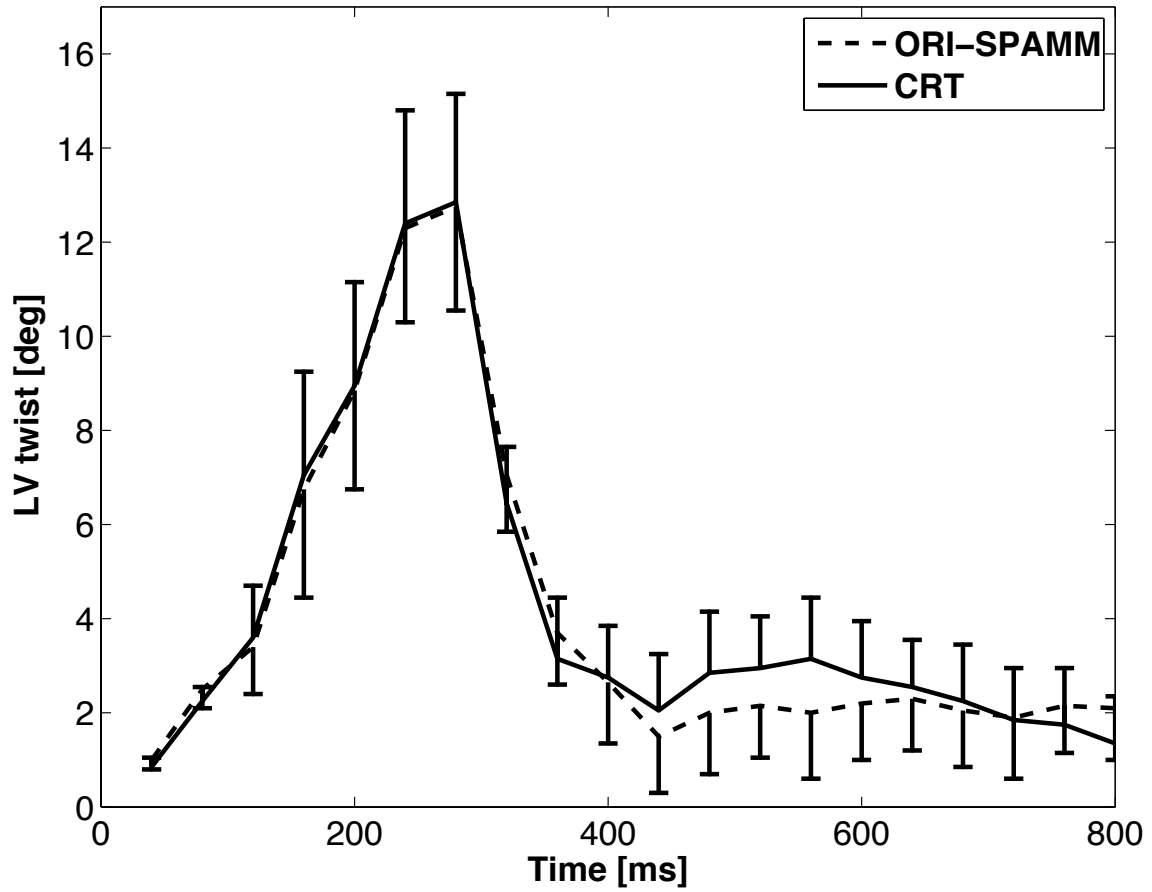


Figure 3.8: LV mean twist measurement from 10 healthy volunteers using FAST method for CRT (solid) and ORI-SPAMM line tagged images (dashed). The one-sided error bars reflect the standard deviation for each cardiac phase.

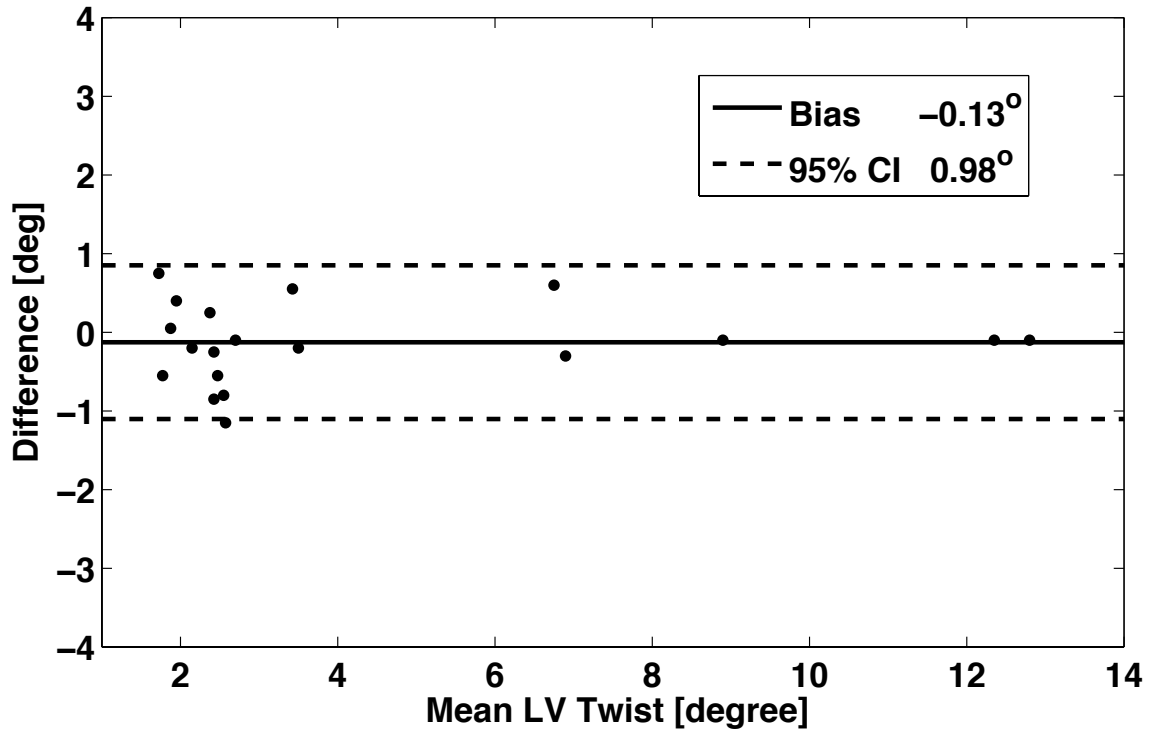


Figure 3.9: Bland-Altman plot comparing the LV twist measurements obtained using the ORI-SPAMM and CRT methods.

Discussion

In this study we defined the theory, demonstrated simulation and phantom results, and evaluated in vivo images using complementary radial tags. CRT extends tag contrast throughout the cardiac cycle and affords the potential advantages of a tagging pattern that is more closely matched to the annular geometry of the left ventricle.

Simulation results show that the magnetization pattern near the tag center is complex and difficult to predict. In practice, the center of the radial tag pattern is placed in the LV blood pool and subsequent convection mixes the blood signal and eliminates any tag pattern inside the LV cavity. In the CRT images the LV blood pool tag signal is

further reduced by image subtraction, which produces dark blood LV images while the radial tagging pattern remains apparent in the myocardial wall throughout the cardiac cycle.

As described in Equation 3.1 RT images contain both tag and image information while CRT images contain only enhanced tag contrast information. With the additional use of the RFA scheme, the CRT tag contrast remains relatively constant throughout the entire cardiac cycle.

CRT also suppresses background tissues outside the heart as a consequence of image subtraction and the shallow tagging pattern, which fades quickly. This contrast property is being further explored as a means for enabling segmentation of the heart for quantitative evaluation of LV function.

Both RT and CRT tag profiles are affected by the RF pulse duration, tag number, amplitude of the RF pulse and gradients lobes. In this study these parameters were particularly chosen to make sure spins at the LV myocardial radius have the highest tag contrast, while the contrast for other tissues still follows the approximation in Equation 3.4 and Equation 3.5. The relationship of the tag profile as a function of the above parameters needs to be further studied.

The center of the radial tags should be at the center of the LV cavity in order to obtain the best radial tagging pattern. This can be achieved by moving the table to an optimal position. However, image quality decreases dramatically if the images are acquired outside of the gradient linearity range. A retrospective analysis of the clinical data shows that our sequence can generate acceptable tag pattern quality for a majority

of patients (over 99%). Even with observable tag pattern imperfections, CRT may still provide useful landmarks for the assessment of cardiac function.

CRT images can be generated from the subtraction of the two sets of radial tagging images in several ways. We initially used an inversion pulse after the radial tags and subtracted the two sets to generate CRT images. However, this resulted in a blurry tag edge profile due to the asymmetric pattern of the inverted and non-inverted magnetization. Our current method using a phase shift between the two sets of tag profiles, on the other hand, produces shaper tag profiles and results in better quality CRT images.

CRT images require the subtraction of the two sets of radial tagged images, which are acquired in a single breath hold. Our current sequence scheme acquires the first set of images completely before acquiring the second set of images. Therefore, high image quality depends on the subject's breath hold stability. A small movement of the diaphragm during the breath hold can result in poor tag and image quality after image subtraction. This may be improved by interleaving the two sets of radial tagging acquisitions to further minimize the potential subtraction error. Currently, the acquisition duration for the CRT sequence is ~20 seconds. While it is not a difficult task for a healthy adult, this can be challenging for patients and children with impaired cardiac or respiratory function.

The CRT method generates a tag pattern with enhanced tag contrast that better matches the annular shaped LV myocardial wall in SA images. These properties may enable more accurate measurements of the LV rotational mechanics, including LV twist and torsion or measures like circumferential strain, especially in mid-diastasis and late

diastolic cardiac phases. Currently, the FAST analysis method is validated for line tagged images to provide a global LV twist measurements, but needs to be further evaluated for application to CRT patterns. A previous study also indicates that the RT technique can estimate regional LV rotation (59) and an extension to CRT should be evaluated. Future work involves developing a faster and robust analysis method, then evaluating accuracy, precision, and reproducibility in a clinical setting.

Conclusion

In conclusion, the CRT technique is a novel myocardial tagging method that generates high tag contrast in the later cardiac phases. It can be potentially used for evaluating cardiac function and performing quantitative analysis of left ventricular rotational function.

Acknowledgement

This work was supported, in part, by funding from the American Heart Association and Siemens Medical Solutions to Dr. Daniel B. Ennis.

Chapter 4. The Effect of Myocardial Fibrosis in Left Ventricular Rotational Mechanics in Duchenne Muscular Dystrophy

Duchenne muscular dystrophy (DMD) is a genetic disease affecting 1 in 3500 male births(60). The disease results from the expression of a dysfunctional dystrophin complex or a complete lack of dystrophin protein(30), which binds the actin-myosin contractile apparatus to the cell's sarcolemma. Without the correct dystrophin complex the mechanical stress induced by contraction damages both cardiac and skeletal muscle(32). Ultimately, fibro-fatty tissue replaces damaged muscle cells and results in progressive cardiomyopathy, a major contributor to morbidity and mortality in patients with DMD(61,62).

Clinically, cardiomyopathy is detected early in the second decade of patients' lives and is universal by the end of the second decade(63). Electrocardiography can detect cardiac changes before symptoms become apparent, highlighting the importance of monitoring cardiac function at a young age so that abnormalities can be addressed before clinically manifest(63).

Electrocardiographic measure of cardiomyopathy, such as reduced ejection fraction (EF), however, are actually late markers of cardiomyopathy(23). Although tissue Doppler can help detect markers that precede EF abnormalities, its use is also limited due to poor acoustic imaging windows, low SNR(64-66), and operator dependent image quality. Currently, however, even with these drawbacks, two-dimensional echocardiography, not MRI, is still the standard clinical imaging technique used to diagnose hypertrophic cardiomyopathy(67).

Indeed, unlike echocardiography, CMR offers high spatial resolution and high contrast images throughout the heart, which lead cardiac MRI to be the research and clinical “gold standard.” The systematic and direct views afforded by a cardiac MRI exam forego the need to use geometric assumptions as in electrocardiographic measurement of the LV(67). MRI, on the other hand, permits directly summing volume information from adjacent and parallel imaging slices and subsequent summation of the imaged sections of the LV myocardium yields both accuracy and consistency in its results(67). Indeed, patients with DMD often present with obesity or scoliosis, posing particular disadvantages for echocardiography, but not MR imaging windows(68,69)

Another significant barrier to obtaining quantitative measures of cardiac function is the lack of natural landmarks within myocardium, which can help track intramural myocardial movement. MRI, however, can overcome this challenge by creating patterns in the bulk magnetization using a pattern of choice that then visibly tracks myocardial contraction and relaxation. Because no contrast agents are necessary, such tagging poses no additional hazards for patients.

Echocardiographic speckle tracking has also emerged as a new method for measuring myocardial regional function (70). Echocardiography is well regarded clinically because of its low-cost and ease-of-use, but it does generally lack flexibility in soft-tissue contrast mechanisms. MRI on the other hand has well-established methods for measuring focal fibrosis using the late gadolinium enhancement (LGE) (71,72) technique or T₁-mapping approaches for estimating diffuse fibrosis (73).

Changes in conventional estimates of cardiac function (e.g. ejection fraction, EF) typically occur late in Duchenne and Becker muscular dystrophy (DMD/BMD). Cardiac

MRI tagging is a noninvasive imaging biomarker for quantifying ventricular dysfunction in DMD/BMD cardiomyopathy. In particular, estimates of ventricular rotational mechanics (e.g. peak twist or normalized untwisting rate) may provide insight to early ventricular dysfunction before patients become overtly symptomatic. Using the Fourier Analysis of Stimulated Echo (FAST) (55) technique to analyze tagged MR images, we can accurately, quickly, and quantitatively obtain measures of global rotational mechanics. This may enable the diagnosis of cardiomyopathies long before symptoms present clinically, especially in boys with DMD for whom the early signs of cardiomyopathy are often masked by the inability to exert themselves substantially as their ambulation becomes increasingly limited.

Furthermore, myocardial fibrosis in DMD/BMD patients is frequently reported and could significantly impact LV rotational mechanics. However, the functional consequences of myocardial fibrosis in these patients are incompletely understood. The **objective** of this study is to quantify LV rotational mechanics in pediatric DMD/BMD patients with normal EF (N-EF) or low EF (L-EF) and with (f+) or without (f-) fibrosis. Of course, the measures we have studied herein to identify cardiomyopathy in the DMD patient population can also be used to help guide clinicians in the diagnosis and treatment of other cardiomyopathies.

Methods

Patient Demographics

Seventeen (N=17) male pediatric subjects (13.7±4.5 years old) genetically diagnosed with DMD/BMD provided assent to participate in an IRB approved study and

their parent or guardian permission to participate. Each pediatric subject underwent a cardiac 3T MRI exam that included evaluation of functional status with cine MRI, cardiac tagging MRI, and ventricular scar evaluation with late gadolinium enhancement (LGE) MRI. Ten (M=10) non-aged-matched (29 ± 4.3 years old) healthy volunteers were also evaluated to provide context for interpreting the pediatric data.

Image Acquisition

A cardiac gated spoiled gradient echo sequence was modified to support 1-1 binomially weighted ORI-SPAMM (54), which was developed to eliminate the effects of off-resonance accrued during motion encoding. Tagged images of the LV short-axis were acquired at the most basal and apical slice locations for which the myocardium retained an annular shape during the entire cardiac cycle. The following parameters were used: 280-330x280-330mm field-of-view, 6mm slice thickness, 192x192 acquisition matrix, 395 Hz/pixel receiver bandwidth, TE/TR =2.33-2.39/4.71-4.83 ms, 8 phase encode lines per segment, 12° imaging flip angle, 8 mm tag spacing and two-fold GRAPPA.

Data Analysis

LV mass, LVESV, LVEDV, and LVEF were calculated from the cine MR images. LV twist was calculated using the Fourier Analysis of STimulated echoes (FAST) method(55). The normal EF cut-off was >55.9% for 8-15 year-olds (74) and >53.2% for 16-20 year-olds(75). The presence or absence of myocardial fibrosis was determined by consensus agreement between a radiologist and a cardiologist. Comparisons were

made using t-tests with Holm-Sidak correction. Peak LV twist (LV-PT) was defined as the difference in rotation angle (ϕ) between the apex and the base.

$$LV \text{ Peak Twist} = \max (\phi_{apex} - \phi_{base}) \quad \text{Eq. 4.1}$$

Normalized LV untwist rate (LV-NUR) was defined as:

$$LV \text{ NUR} = \frac{Max(\Delta\text{Twist})}{LV-PT} \quad \text{Eq. 4.2}$$

where ΔTwist is the LV twist difference between two adjacent cardiac frame during untwist process.

Results

The volunteers had mean LV peak twist of $12.2 \pm 2.6^\circ$ and LV normalized untwist rate $-12.5 \pm 2.1 \text{ s}^{-1}$. The table shows lower LV-PT and LV-NUR in the EF-n/f- group compared to non-age matched healthy volunteers. LV-PT and LV-NUR significantly decreased in the N-EF/f+ group. LV-PT and LV-NUR were further decreased in the L-EF/f+ and were lowest in the L-EF/f+ group. T-tests with Holm-Sidak correction showed significant difference between L-EF/f- and L-EF/f+ in LV-PT. No significant difference was detected for LV-NUR. (Table 4.1)

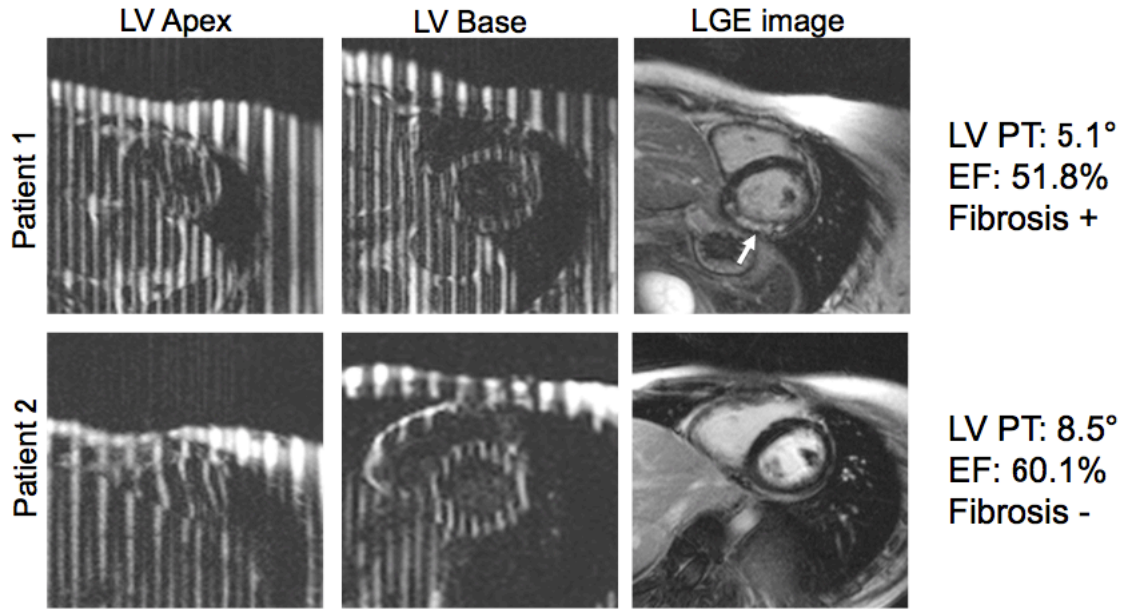


Figure 4.1 ORI-SPAMM tagged images at the LV apex and base in the short-axis view and LGE images from two patients with DMD. Patient 1 has reduced LV peak twist (LV PT), reduced ejection fraction (EF), and conspicuous fibrosis compared to Patient 2.

	Normal (EF-N)		Abnormal (EF-L)	
Fibrosis (-)	LV-PT: $9.3 \pm 2.2^\circ$	N=6	LV-PT: $8.7 \pm 1.4^\circ$	N=2
	LV-NUR: $-11.1 \pm 3.2^\circ \text{ s}^{-1}$		LV-NUR: $-10.5 \pm 1.2^\circ \text{ s}^{-1}$	
Fibrosis (+)	LV-PT: $7.8 \pm 2.2^\circ$	N=6	LV-PT: $5.3 \pm 0.5^\circ$	N=3
	LV-NUR: $-9.1 \pm 2.2^\circ \text{ s}^{-1}$		LV-NUR: $-8.3 \pm 0.5^\circ \text{ s}^{-1}$	

Table 4.1

Discussion

It is widely known that patients with DMD frequently exhibit myocardial fibrosis and that both myocardial fibrosis and the DMD disease process can cause decreased LV-PT. Previous studies, however, did not consider the two factors separately. Our result shows that patients with DMD and without fibrosis have a decreased LV-PT and LV-

NUR and that the presence of fibrosis decreases these values even further. Fibrosis and DMD appear to have combined effect on LV dysfunction. Since fibrosis has a non-negligible effect, future DMD studies should take in consideration the specific role of fibrosis alone. Meanwhile, the size (e.g. volume or area) of fibrosis and the type of fibrosis (diffusive or non-diffusive) need to be further addressed. Moving forward, T_1 mapping can be used to estimate the myocardial extracellular volume (ECV), which reflects diffuse fibrosis (76). The current DMD protocol can easily be modified to accommodate this sequence.

In this study group of patients with DMD was divided into four groups (EF-N, EF-L, f+ and f-). Our results indicate that both LV-PT and LV-NUR are lower in patients with DMD/BMD despite normal EF, compared to non-age matched healthy volunteers. Both low EF and the presence of fibrosis are associated with further decreases in LV-PT and LV-NUR.

Overall, while it is known that EF changes late in the disease process, LV-PT may serve as a sensitive biomarker for the early detection of worsening disease. The presence of fibrosis and decreased LV twist should be added to current clinical protocols as possible early measures of cardiac function in patients with DMD. Due to the limited sample size and lacking of age-matched controls, no ANOVA test was performed and significantly more data is needed to establish firm conclusions in the future.

Acknowledgements

This work was supported, in part, by research support from the American Heart Association AHA 13BGIA14530010 to Daniel B. Ennis and AHA 11PRE6080005 to Meral L. Reyhan and UCLA's Center for Duchenne Muscular Dystrophy to Daniel B. Ennis.

Chapter 5 – The Effect of Free-breathing on Left Ventricular Rotational Mechanics in Normal Subjects and Patients with Duchenne Muscular Dystrophy

Introduction

Cardiac MRI exams increasingly include the evaluation of quantitative metrics of ventricular performance(77). Quantitative measures of cardiac function including, for example, strain and twist measures obtained from MRI tagging (29), HARP(78), DENSE(79), or FAST(55), can be used to stage disease progression and monitor the response to therapy. Conventional cardiac MRI exams, however, require repeated breath holding, which places a burden on some clinical patients. This breath hold paradigm presents two problems for patients with Duchenne Muscular Dystrophy (DMD) who develop progressive respiratory impairment and the signs and symptoms of cardiac involvement at an early age(80).

Firstly, breath holding imparts subtle shifts in the hemodynamic loading of the heart, which consequently impacts quantitative measures of global and regional Left Ventricular (77) function(81). In fact, free-breathing may provide a better estimate of normal, ambulatory physiology, whereas breath holding causes subtle Valsalva(82) or Mueller(83) maneuvering, which alters cardiac function.

Secondly, while breath hold studies may be readily obtained when the disease is mild, the studies become more challenging as the disease progresses. Hence, for longitudinal studies it may be judicious to use free-breathing strategies at all time points in anticipation of declining respiratory function. For DMD patients, when

breath held imaging is not feasible, free-breathing techniques, such as navigator gating(84), respiratory bellows gating(85), and multiple signal averages (86) can be used to minimize respiratory motion artifacts. Hence, the objective of this study was to evaluate the effect of free-breathing on quantitative measure of left ventricular (77) rotational mechanics first in healthy subjects, then in patients with DMD.

Materials and Methods

MRI Protocol

The local institutional review board approved this study and all adult subjects provided signed statements of informed consent. Sixteen healthy human subjects (N=16) with no history of cardiovascular or respiratory disease (1 female, 27.8±3.9 years) were scanned. In a subsequent study, consent was obtained from parents or legal guardians for pediatric patients with DMD. Five (N=5) patients with DMD were also scanned (all male, 11.3±3.7 years). The demographics for each group are summarized in Table 1.

	Normal	DMD
Age [yrs]	27.8±3.9	12±4.3
Weight [kg]	73.1±12.6	35.1±10.6
Gender [Male/Female]	15/1	5/0
Heart Rate [bpm]	59.3±8.3	69.3±8.9

Table 5.1. Demographics of healthy volunteer and patients with Duchenne muscular dystrophy.

All subjects were oriented on the scanner table in a headfirst and supine position. All images were acquired using a six-element anterior coil array and a six-element posterior coil array with ECG gating using end expiratory breath holds on a 3.0T scanner (TIM Trio, Siemens Healthcare, Erlangen, Germany). Localizer sequences were used to identify the apical and basal slices in the cardiac short-axis (SA) plane. Global LV function was measured using balanced steady-state free precession (bSSFP) cine images collected with a 6 mm slice thickness and a 4mm gap between slices, in parallel LV SA planes.

A cardiac gated spoiled gradient echo sequence was modified to support 1-1 binomially weighted ORI-SPAMM(54), which was developed to eliminate the effects of off-resonance accrued during motion encoding. ORI-SPAMM modifies the original SPAMM tagging prep to include a 180° refocusing pulse and a split motion encoding gradient. This 180° pulse refocuses off-resonance accrued during the tagging preparation, which can lead to errors in quantitative measures of LV strain measured by DENSE and/or rotation. ORI-SPAMM tagged images of the LV short-axis were acquired at the most basal and apical slice locations for which the myocardium retained an annular shape during the entire cardiac cycle. The following parameters were used: 280-330x280-330mm field-of-view, 6mm slice thickness, 192x192 acquisition matrix, 395 Hz/pixel receiver bandwidth, TE/TR =2.33-2.39/4.71-4.83 ms, 8 phase encode lines per segment, 12° imaging flip angle, 8 mm tag spacing, two-fold GRAPPA (53) based parallel imaging acceleration (24 reference lines). Cine ORI-SPAMM tagged images were acquired using both horizontal and vertical tagging in separate acquisitions for each subject during breath holding (BH), free-

breathing with averaging (AVG), and free-breathing with respiratory bellows gating (BEL). The BH scans were acquired during an end expiratory breath hold of 15 heartbeats (12.5 ± 2.1 seconds depending upon heart rate). The FB images were acquired during free breathing with four signal averages. The BEL scans were acquired prospectively during free breathing with the respiratory bellows gating set to acquire during the window of 30-40% expiration. Total scan time for the BEL sequence was 45 to 65s. The scan order for horizontal and vertical tagging of the apex and base was randomized for each set of scans for each subject, to minimize the order effects.

Fourier Analysis of Stimulated echoes (FAST)

FAST analysis is a semi-automated image processing method designed to quantify global LV rotation from tagged MR images. The main principle of the FAST method is that rotation in image space has a one to one correspondence with rotation in Fourier space, but in Fourier space the tagging information is focused into stimulated echoes, which are simpler to track than multiple tag lines. FAST has been shown to compare favorably to conventional estimates of LV twist from cardiac tagged images, but with significantly reduced user interaction time during post-processing(55).

FAST was applied to images collected at both the apex and base of the heart to measure the apical (Φ_{apex}) and basal (Φ_{base}) rotation in degrees. The difference between Φ_{apex} and Φ_{base} is defined as twist. The FAST method has been described in more detail and previously validated using both SPAMM and CSPAMM images in

healthy volunteers(87). LV twist was defined as the difference in rotation between the apex and the base (Equation 1.1). The LV circumferential-longitudinal shear-angle (CL-shear angle) was also measured and is defined as (Equation 1.2).

Estimates of apical and basal epicardial radii were made from averaging the end systolic semi-major and semi-minor axes of the ellipses used to mask the LV during FAST processing. Peak CL-shear angle was calculated as an alternate measure of LV function that normalizes for heart size and selection of imaging planes(22).

Statistical Analysis

The Wilcoxon signed rank test was used to test for the difference in peak LV twist between the two groups. Bland-Altman analysis was used to compute the bias and 95% confidence intervals for peak LV twist and peak LV CL-shear angle for comparisons of each respiratory motion compensation technique. The Bland-Altman bias (median of the difference between groups) and 95% confidence intervals were calculated using bootstrap sampling 1000 times with replacement due to the limited sample size and non-Gaussian distribution.

Results

Image Quality

Figure 5.1 demonstrates the ORI-SPAMM tagged image quality in the LV short-axis view for healthy volunteers (Figure 5.1A-C) and DMD patients (Figure t.1D-F). For the healthy volunteer the image quality is good and the BH (A) and BEL(C) images are comparable. Figure 5.1D is a typical case wherein the patient with DMD

can not breath hold well, resulting in blurred images, whereas AVG (Figure 5.1E) partially mitigates motion blurring and BEL (Figure 5.1F) demonstrates substantially improved image quality.

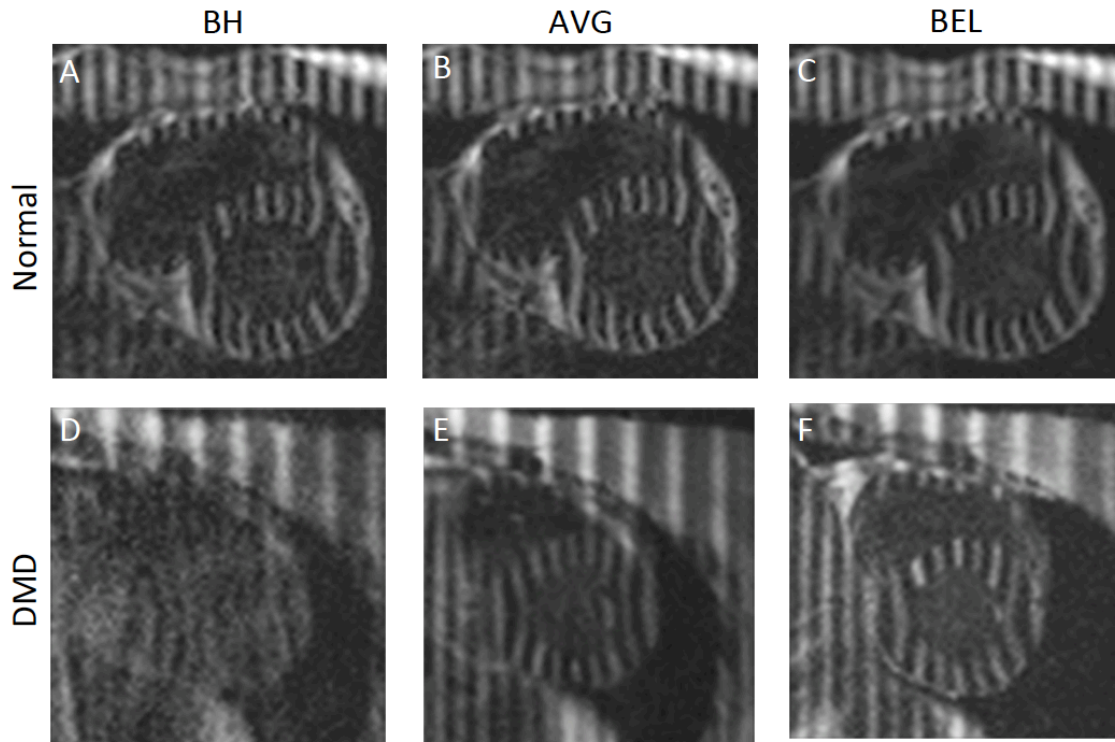


Figure 5.1 Tagged LV images in the short-axis view for a healthy volunteer (A-C) and a patient with DMD (D-F) acquired with BH (A and D), AVG (B and E) and BEL (C and F) respiratory motion compensation.

LV Rotational Mechanics

Figure 5.2A demonstrates the mean LV twist curve from five DMD patients in the subsequent study. For patients with DMD the mean peak LV twist measurements were $10.5 \pm 3.6^\circ$ (BH), $9.3 \pm 3.4^\circ$ (AVG), and $8.5 \pm 3.6^\circ$ (BEL); and BEL was 19.0% lower and significantly different than BH ($P=0.004$).

Figure 5.2B demonstrates the mean LV twist curve from 16 healthy volunteers for BH, AVG, and BEL data. Errors bars represent one standard deviation and characterize within group physiologic variance. For healthy volunteers the mean peak LV twist measurements were $12.9 \pm 2.3^\circ$ (BH), $11.3 \pm 3.8^\circ$ (AVG), and $10.0 \pm 3.6^\circ$ (BEL). BEL estimates of peak LV twist were 22.5% lower and significantly different than BH estimates ($P=0.003$).

Hence, a similar trend was observed in both healthy volunteers and patients with DMD wherein BH had the highest peak LV twist values, AVG had intermediate peak LV twist values, and BEL had the lowest peak LV twist values. The LV rotational and geometric measures used to estimate LV twist and CL-shear are summarized in Table 5.2.

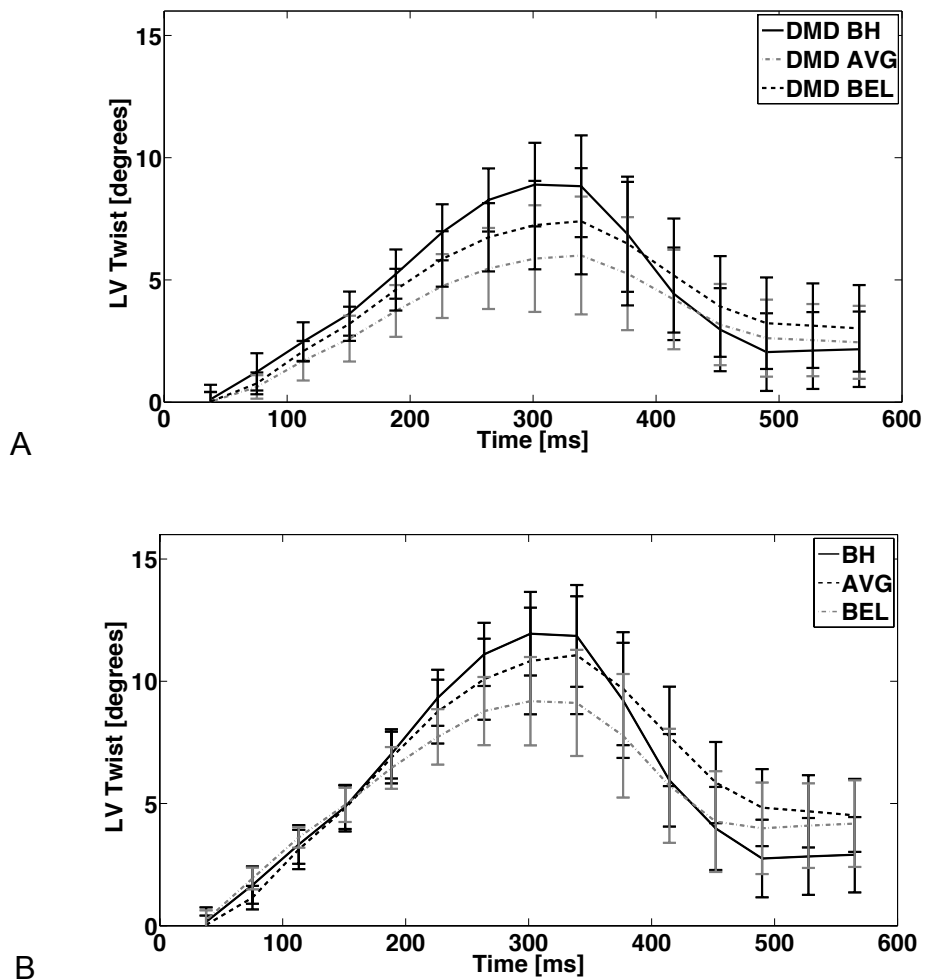


Figure 5.2. Mean LV twist for (A) healthy volunteers and (B) patients with DMD for breath-held (BH, solid), free-breathing with averaging (AVG, dashed) and bellows gated (BEL, dash-dotted) respiratory motion compensation. Error bars are standard error of the mean for clarity and characterize within group physiologic variance. BH LV twist is generally higher compared to AVG or BEL, especially at its peak.

	Normal			DMD		
	BH	AVG	BEL	BH	AVG	BEL
Mean Peak LV Twist [deg]	12.9±2.3	11.3±3.8	10.2±3.6*	10.5±3.6	9.3±3.4	8.6±3.6*
Mean Peak CL-Shear Angle [deg]	6.4±1.7	6.2±1.4	5.9±1.6	5.9±1.7	5.7±1.4	5.6±2.1
Mean Peak Apical Rotation [deg]	8.9±2.9	8.1±3.0	7.2±3.8*	7.1±3.1	6.4±3.4	5.8±3.7
Mean Peak Basal Rotation [deg]	-4.4±1.8	-3.2±2.4	-3.0±1.6	-3.4±1.7	-2.9±2.3	-2.8±1.7
LV Apical Epicardial Radius [mm]	23.3±2.5	25.0±3.1	25.9±3.4*	17.1±3.1	18.4±3.5	20.2±4.6*
LV Basal Epicardial Radius [mm]	32.3±2.3	32.9±2.4	33.1±2.5*	27.0±3.0	28.7±3.3	30.4±4.1*
Distance between Apex and Base [cm]	5.0±1.9			4.0±1.2		

- *Indicates statistical difference compared to BH (P<0.05)

Table 5.2. Measurements of left ventricular rotational mechanics in healthy volunteers and in patients with Duchenne muscular dystrophy.

Bland-Altman analysis of peak LV twist between each group are summarized: BH versus AVG analysis resulted in a bias of 1.5° [0.1°, 2.9°] and AVG versus BEL resulted in a bias of 1.2° and [0.1°, 2.3°] indicating moderate agreement between the two groups. Notably, BH peak LV twist was greater than BEL peak LV twist for all subjects. A similar trend was seen for AVG versus BEL. BH versus BEL results for the pool of healthy volunteers (dot) and DMD patients (diamond) are demonstrated in Figure 5.3. It shows a median bias of 2.7° and 95% CI [0.1°, 5.3°] indicating a non-negligible increase of BH peak LV twist compared to BEL.

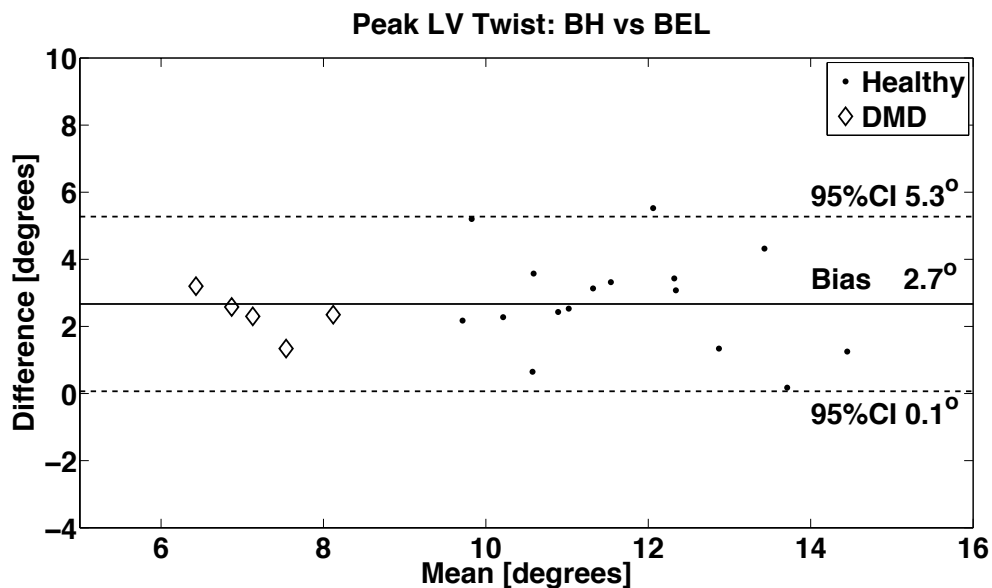


Figure 5.3. Bland-Altman analysis of peak LV twist derived from breath held (BH) versus free-breathing with bellow (BEL) indicates non-negligible difference, with a bias of 2.7° and a 95% confidence interval of [0.1°, 5.3°]. The difference likely arises from respiratory induced changes in loading conditions between BH and BEL.

Left Ventricular Geometry

The mean apical and basal epicardial radii measured in an end-systolic cardiac frame were reported in Table 5.2. The only significant differences observed in the radius data were between the decreased apical epicardial radii for BH compared to BEL ($p=0.007$) and the similarly decreased basal epicardial radius for BH compared to BEL ($p=0.006$); all other differences were not significant with $p>0.05$ despite an apparent trend for an increase in radii from BH to AVG to BEL.

CL-Shear Angle

The peak LV CL-shear angle measurements were $6.4\pm 1.7^\circ$ (BH), $6.2\pm 1.4^\circ$ (AVG), and $5.9\pm 1.6^\circ$ (BEL) for healthy volunteers and were not significantly different. Similarly, for patients with DMD the peak LV CL-shear angle measurements were $5.9\pm 1.7^\circ$ (BH), $5.7\pm 1.4^\circ$ (AVG), and $5.6\pm 2.1^\circ$ (BEL) and were not significantly different. Bland-Altman analysis of the pooled peak CL-shear data for BH versus AVG resulted in a bias of 0.1° [-0.5° , 1.6°], BH versus BEL resulted in a bias of 0.8° [0.4° , 2.1°], and AVG versus BEL resulted in bias of 0.6° [0.1° , 1.6°]. These results indicate good agreement for estimates of peak LV CL-shear between the different respiratory motion compensation methods.

Discussion

Breath holding alters cardiovascular loading conditions compared to free-breathing, likely as a consequence of subtle changes in intrathoracic pressure. Cardiac MRI performed during free-breathing conditions may produce measurements that are less prone to measurement bias as a consequence of

inadvertent, irreproducible, and subtle Valsalva(82) or Mueller(83) maneuvers. Notably, the differences in peak LV twist between and BEL are larger than those observed in a previous intra-exam reproducibility study(87), which showed differences of -0.6° compared to 2.3° found in this study. This indicates that breath hold conditions are an important consideration in longitudinal studies. In patients with DMD, due to progressive muscle weakness, breath holding becomes increasingly difficult. Because the quality of breath holding cannot be controlled at each time point in a longitudinal study in DMD patients, free breathing approaches are a judicious consideration. Alternately, since measures of peak LV CL-shear appear to be less effected by the breath hold conditions, this measure may be a more consistent measure of LV rotational mechanics in these patients.

This study demonstrated that BEL estimates of peak LV twist were significantly smaller than BH estimates, however AVG peak LV twist estimates were only slightly lower than BH peak LV twist. This trend in mean peak LV twist values is evident in Table 2. Similarly, quantitative measures like radial, circumferential, and longitudinal strain derived from navigator-gated 3D cine DENSE have been shown to correlate well with, but are lower than breath-held strain values(84). Likewise, HARP strain estimates during free-breathing are decreased compared to breath-holding values(88). These differences all likely arises from respiratory induced differences in loading conditions.

The observed increase in end systolic epicardial radius during BEL compared to is consistent with an increase in afterload, which has previously been shown to accord with a decrease in torsion (35) – consistent with the results herein. The concomitant

change in loading conditions and LV volumes (i.e. radii) underlies the differences observed between breath-held and free-breathing peak LV twist measurements, but also contributes to the fact that there was no significant difference in the peak CL-shear angle data between the different respiratory motion compensation methods. This indicates that CL-shear angle is less sensitive than LV twist to differences in the method of respiratory compensation and CL-shear may be a better measure of rotational mechanics for longitudinal studies when breath hold conditions can't be controlled longitudinally. Nevertheless, there was a trend toward reduced CL-shear values with BEL compared to BH. Hence, the best standard for a longitudinal evaluation of LV rotation mechanics may be a free-breathing evaluation of CL-shear.

In conclusion, breath holding directly affects estimates of peak LV twist, but not CL-shear. When using quantitative imaging biomarkers of LV rotational mechanics to monitoring disease progression or the response to therapy, especially in patients with DMD for whom decline in respiratory function is certain, it will be important to use a free-breathing strategy for all studies to facilitate intra-subject longitudinal comparisons.

Limitations

The study occurred in two stages wherein healthy subjects were evaluated first and we subsequently evaluated a cohort of patients with DMD. Hence, direct comparisons between the two groups were not made. Nevertheless, very similar trends are seen in both groups for peak LV twist as a function of breath holding condition. Peak LV twist values were observed to be lower in patients with DMD, but

there is also a notable age difference between the two groups and preliminary work(89) indicates that LV twist increases with age, whereas CL-shear is relatively constant over five decades. Ideally, a group of age-matched pediatric controls would be enrolled for a comparative study, but this has proven to be challenging.

Although not widely available at all imaging centers nor for all MRI pulse sequences respiratory motion compensation with navigator echoes is an attractive option, but was not available for this study. Moving forward consideration will be given to image-based navigators(90), which can avoid the set-up time associated with both bellows and navigator echoes.

The effects of through-plane motion should also be considered as a possible confounder. Stuber et al. previously presented a slice-following method to account for through plane motion (46), which could be considered in a future implementation. However, a study, which compares 2D and 3D peak LV torsion, shows that only very small differences are detected when through-plane motion is corrected(91).

While LV twist and CL-shear were evaluated in this study several previous studies of patients with DMD have used strain as a measure of regional ventricular function(92,93). An important goal of this line of investigation is to identify the earliest indications of impending dysfunction, for which a more comprehensive, longitudinal study is needed.

Acknowledgements

This work was supported, in part, by research support from the American Heart Association to MRL and to DBE and UCLA's Center for Duchenne Muscular Dystrophy to DBE.

Chapter 6 – Left Ventricular Twist and Shear in Patients with Primary Mitral Regurgitation

Primary mitral regurgitation (MR) is a common valvular disorder that foments left ventricular (LV) dysfunction (94). Primary MR is characterized by an incomplete closure of the mitral valve, which permits the flow of blood across the mitral valve during systole (decreased afterload) and leads to increased end-diastolic volume (increased preload). Additionally, chronic MR is known to deleteriously impact the rotational dynamics of the LV (95-97). There exist several measures of the rotational mechanics of LV performance, but it remains unclear, which measures are best for characterizing deleterious changes in LV function (33,34,98). The twisting motion of the heart arises from transmural differences in the local myofiber orientation, which is thought to minimize transmural stress gradients(99). Hence, alterations in the twisting mechanics may be indicative of incipient worsening disease. Several measures of rotational mechanics are suggested as imaging biomarkers for LV dysfunction (13,22), including twist, twist-per-volume, and shear angle.

LV twist is the preferred nomenclature for the measurement defined as the difference in the rotation of the apex relative to that of the base of the heart(22). A decrease in LV twist during the progression of MR has previously been evaluated with ultrasound (95-98) in human subjects and implanted radiopaque markers in animal studies(33,34). Twist-per-volume slope normalizes for the volume of ejected blood. Therefore a change represents a disruption of the fundamental connection between myofiber shortening and ejection. CL-shear is a measure of rotational mechanics that

accounts for changes in LV ventricular dimensions, which is reported to increase with MR (100).

LV rotational mechanics is a potentially valuable biomarker of LV dysfunction evaluation. Traditional analysis methods like FindTags (101) require significant user interaction time (~1 hour) and the best alternatives typically require several tens of minutes, which significantly limits their clinical adoption. Fourier Analysis of STimulated Echoes (FAST) is a new MRI tissue tagging method that has recently been shown to compare favorably to conventional estimates of left ventricular (77) twist from cardiac tagged images, but with significantly reduced user interaction time (2-3 minutes primarily for study selection) (55). FAST was applied to grid tag images acquired from patients with moderate and severe degenerative isolated MR to evaluate LV twist, CL-shear angle, and systolic twist-per-volume slope. We hypothesized that LV systolic twist-per-volume slope would decrease with increasing severity of MR because it accounts for decreases in both rotational mechanics and increases in stroke volumes.

Methods

The local institutional review board approved this study and all subjects provided written informed consent. Moderate MR patients (n=29) and severe MR patients (n=54) with degenerative isolated MR were studied with MRI. Clinicians judge categories of moderate or severe MR by color flow Doppler, LV EF of more than 55%, LV end-systolic dimension of 40 mm, echocardiographic thickening of the mitral valve leaflets and prolapse.

Healthy normal subjects (n=54) with no history of cardiovascular disease were studied as age matched controls for the MR patients. MR severity was diagnosed qualitatively with echocardiography and Doppler studies and quantitatively with cine MRI. Subject demographics are summarized in Table 1. Data from patients in the normal subject and severe MR subject groups have been presented in a previous study (100).

Breath-held ECG triggered images were acquired for all subjects on a 1.5T scanner (Signa, GE Healthcare, Milwaukee, WI). Prospectively triggered balanced steady-state free precession (bSSFP) cine images were collected in parallel left ventricular (77) short-axis planes using the following typical parameters: 40x40 cm field of view, 256x128 matrix size, 8mm slice thickness, 45° flip angle, 1.6/3.8 ms echo/repetition times, 977 Hz/pixel receiver bandwidth, and 20 cardiac phases per slice in a single breath-hold.

A prospectively triggered spoiled gradient echo sequence was used to acquire short-axis tagged images of the LV with the following typical parameters: 40x40cm field-of-view, 256x128 acquisition matrix, 8mm slice thickness, 10° imaging flip angle, 4.2/8.0ms echo/repetition times, 244Hz/pixel receiver bandwidth, 20.4 to 51.1 ms temporal resolution, and 20 cardiac phases per slice in a single breath-hold. Grid tags were oriented 45° relative to the frequency encoding axis with 7 mm tag spacing.

An experienced trainee used the following criteria to select short-axis slices and derive LV twist measurements: 1) the most apical slice containing the presence of the blood pool throughout the entire cardiac cycle; and 2) the most basal slice in which the

LV myocardium maintained a continuous annular shape during the entire cardiac cycle were selected.

Fourier Analysis of Stimulated echoes (FAST)

FAST(55) is a semi-automated and validated image processing method that only requires 2-3 minutes of user interaction time (mostly for study selection) to quantify LV rotational mechanics. FAST determines object rotation in Fourier space, where rotation in tagged MR images is easier to track. User defined contours of the epicardium in an end-systolic cardiac frame and endocardium in an early systolic cardiac frame were used to isolate the LV myocardium. The central frequency information in Fourier space was nulled and the Fourier image was symmetrically cropped in k-space beyond the first harmonic Fourier peak to reduce computational times, then cumulative rotation of the ventricle was determined with two-dimensional cross-correlation (102). This series of image processing steps was applied to both the apical and basal images of the heart, and the difference between the two rotations was defined as twist. The FAST method was previously validated using line tag images in healthy volunteers(55). Peak twist was defined as the maximum difference in degrees of rotation (Φ) between the apex and the base (Equation 4.1). The systolic twist-per-volume slope was defined as peak LV twist divided by the difference between LV end-systolic volume and end-diastolic volume.

$$\text{Twist-per-volume} = \frac{\text{Peak Twist}}{LVESV - LVEDV} \quad \text{Eq 6.2}$$

The circumferential-longitudinal shear-angle (CL-shear angle) was defined as (21,22) (Equation 1.2)

CL-shear angle is proposed as a measure of LV rotational mechanics that accounts for differences in heart size and the location of the apical and basal slices used for analysis (103). Estimates of apical and basal epicardial radii were made from averaging the semi-major with the semi-minor axes of ellipses fit to the user-defined epicardial contours. The twist rate was defined as the discrete derivative of twist with respect to time with units of degrees-per-second (deg/s). Peak twist rate was defined as the maximum twist rate. Peak untwist rate was defined as the minimum twist rate. Peak normalized untwist rate was defined as the minimum twist rate divided by peak twist as per Thompson et al (77). During ejection the volume of the LV decreases, while twist increases, which leads to a negative systolic twist-per-volume slope(34).

Estimates of LV volumes were obtained from epicardial and endocardial contours manually traced at end-systole and end-diastole from the bSSFP images by a trainee with more than 3 years experience. Papillary muscles were included in the LV volume. The contours were then propagated to the rest of the temporal frames with a dual propagation technique (104). LV volumes were computed by summing the areas defined by the endocardial contours in each short-axis slice multiplied by slice thickness(104). LV mass was computed by summing the areas between endocardial and epicardial contours multiplied by slice thickness and myocardial density (1.05 g/ml) (13).

Statistical Analysis

Summary statistics of the rotational mechanics measurements were reported for each group. ANalysis Of Variance (ANOVA) was used to test for differences in peak twist, apical rotation, basal rotation, systolic twist rate, diastolic untwisting rate, systolic twist-per-volume slope, distance between apical and basal slices, and apical and basal epicardial radii between normal, moderate MR, and severe MR groups while adjusting for the covariates of age, weight, height, and gender. A similar analysis was also performed for peak CL-shear angle (due to some subject height and gender not being recorded an additional ANOVA test was performed without subject and gender as part of the sensitivity check). Additionally, a one-way ANOVA with three groups (normal, moderate MR, and severe MR) was used to assess differences in time to peak twist, peak normalized untwisting rate, endocardial radii, and the demographic values in Table 6.1. Multiple comparisons (Tukey's least significant difference (LSD) procedure) were applied to each measurement to determine which groups were significantly different from each other. A value of $P < 0.05$ was considered statistically significant. All statistical analyses were performed with Matlab version 7.10.

Results

Patient Demographics

Patient demographics are summarized in Table 6.1. Significant differences between the age, gender, height, end-systolic volume, end-diastolic volume, and LVED mass of the normal, moderate MR, and severe MR subjects were detected with a three group one-way ANOVA. No significant differences were noted in weight and heart rate with

95% confident intervals. Significant increases in end-systolic volume, end-diastolic volume, and LVED mass were expected and observed for MR patients.

	Normal	Moderate MR*	Severe MR	ANOVA P-Value
Number of Subjects	54	29	54	-
Age [years]	44.9±14.4	50.2±12.2	54.4±11.7	P=0.01
Age Range [years]	20-70	21-69	25-79	-
Male/Female	23/31	3/21	38/16	P<0.001
Weight [kg]	74.9 ±18.4	74.2 ±16.6	81.3 ±14.9	P=0.08
Height [cm]	171.5±9.4	165.8±9.9	172.9±11.2	P=0.03
Heart Rate [bpm]	65.3±11.9	70.3±12.4	68.9±12.1	P=0.14
End-Systolic Volume [mL]	47.8±12.0	53.6±21.4	77.2± 24.0	P<0.001
End-Diastolic Volume [mL]	131.3±24.5	146.3±43.5	212.2±53.7	P<0.001
LVED Mass [g]	96.0±24.6	91.5±23.0	136.9±36.1	P<0.001

* Height/Gender information is not recorded for 8/5 subjects

Table 6.1: Patient Demographics

Image Quality

Figure 6.1 represents the typical tagged image quality from normal, moderate MR, and severe MR subjects at the time of peak twist for the apex and base. The peak twist, apical rotation, and basal rotation corresponding to the images are also reported within the figure. Due to T_1 relaxation tag contrast fades at middle and late diastolic phases, making the measurement of LV diastolic rotational mechanics challenging.

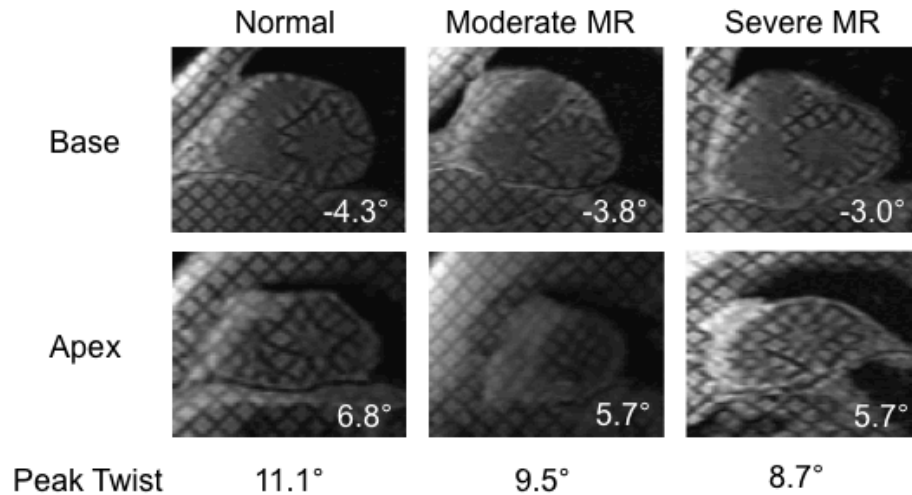


Figure 1. Representative tagged images from a normal subject and patients with moderate MR and severe MR. The basal and apical frames capture the time of peak LV twist. Individual LV rotation values are noted within the frame and peak LV twist values below the frame.

Temporal Resolution

The temporal resolution for normal subjects, patients with moderate MR and patients with severe MR are 33.2 ± 7.2 ms, 30.9 ± 5.2 ms and 31.6 ± 5.9 ms respectively and are not significantly different per ANOVA.

LV Rotation

LV apical and basal peak rotation measures are summarized in Table 6.2. Mean peak apical rotation for normal subjects, moderate MR patients, and severe MR patients were: $7.5 \pm 3.6^\circ$, $5.8 \pm 2.7^\circ$, and $6.2 \pm 2.8^\circ$ respectively. The ANOVA of peak apical rotation between the groups showed differences among the groups ($p=0.004$) and with respect to the covariate of age ($p=0.005$). LSD for apical rotation showed a significant difference

between the normal subject group and the moderate MR patients and between the normal subject group and the severe MR patients.

The ANOVA of peak basal rotation between the groups showed differences among the groups ($p=0.04$) and with respect to age ($p=0.004$). LSD for basal rotation detected differences between the normal subject group and the severe MR patients and between the moderate MR patients and the severe MR patients.

Measurement	Normal	Moderate MR	Severe MR	ANOVA P
Peak Apical Rotation [deg]	7.5±3.6	5.8±2.7 [†]	6.2±2.8 [†]	P=0.004
Peak Basal Rotation [deg]	-3.9±1.3	-3.4±1.4	-2.8±1.6 ^{†‡}	P=0.04
Peak Twist [deg]	11.5±3.3	9.2±3.0 [†]	8.8±2.6 [†]	P=0.0001
Peak Twist Rate [deg/s]	95.3±30.2	78.3±24.7 [†]	71.6±23.0 [†]	P<0.0001
Peak Untwisting Rate [deg/s]	-89.9±43.8	-62.6±32.9 [†]	-63.0±32.0 [†]	P=0.0007
Norm Peak Untwisting Rate [1/s]	-8.0±3.3	-7.1±3.6	-7.2 ±3.2	P=0.4
Time to Peak Twist [ms]	237.3±43.5	254.3±63.2	251.2±87.1	P=0.4
Systolic Twist-per-Volume Slope [deg/mL]	-0.14±0.05	-0.12±0.04 [†]	-0.07±0.03 ^{†‡}	P<0.0001

[†] LSD indicates significant difference from Normal

[‡] LSD indicates significant difference from Moderate

Table 6.2: LV Twist Measurements

LV Twist analysis

LV apical and basal rotation, LV twist and twist rates, and LV twist-per-volume results are summarized in Table 6.2. Figure 6.2 demonstrates the changes in mean LV twist for normal, moderate MR, and severe MR subjects. Figure 6.3 is a scatter plot,

which demonstrates the peak LV twist data from normal, moderate MR, and severe MR subjects.

Similar ANOVA results were observed for the mean peak LV twist, mean peak LV systolic twist rate and mean diastolic untwisting rate, where significant differences were observed between normal subjects and MR patients. However, no significant difference was observed between moderate and severe MR patients for these measures. No significant differences were observed due to patient demographic covariates (age, weight, height, gender). Normalized peak untwisting rate and time to peak twist showed no significant difference among the three groups.

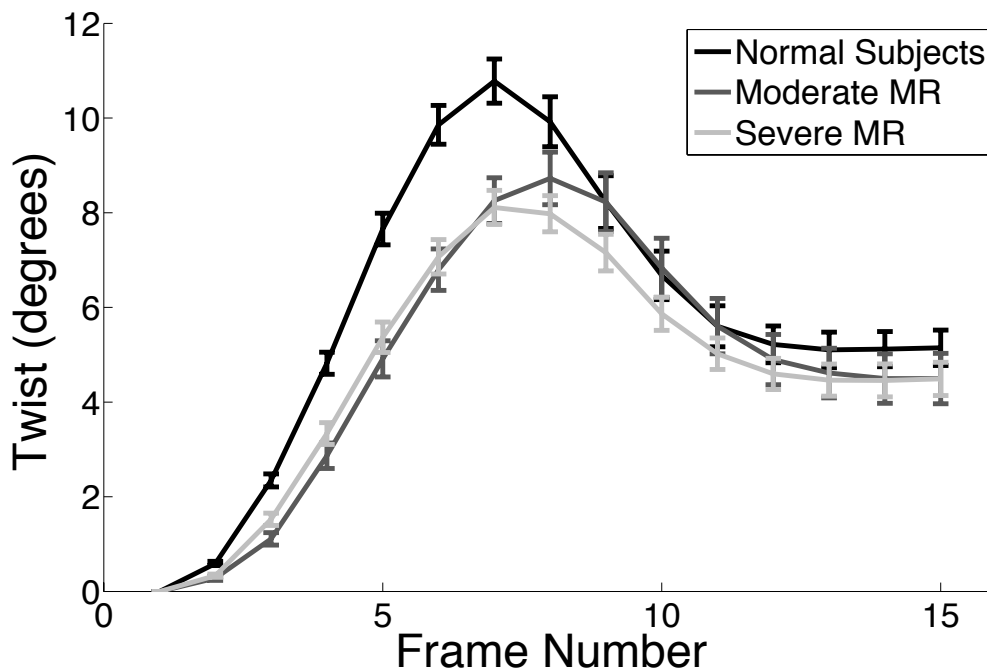


Figure 6.2. Population mean LV twist during the cardiac cycle for normal subjects and patients with moderate MR and severe MR. Error bars are standard error of the mean for clarity. Mean peak LV twist in normal subjects is larger compared to both patients with moderate and severe MR ($p=0.0001$). No significant

difference in mean peak LV twist was observed between moderate and severe MR patients (Table 6.2).

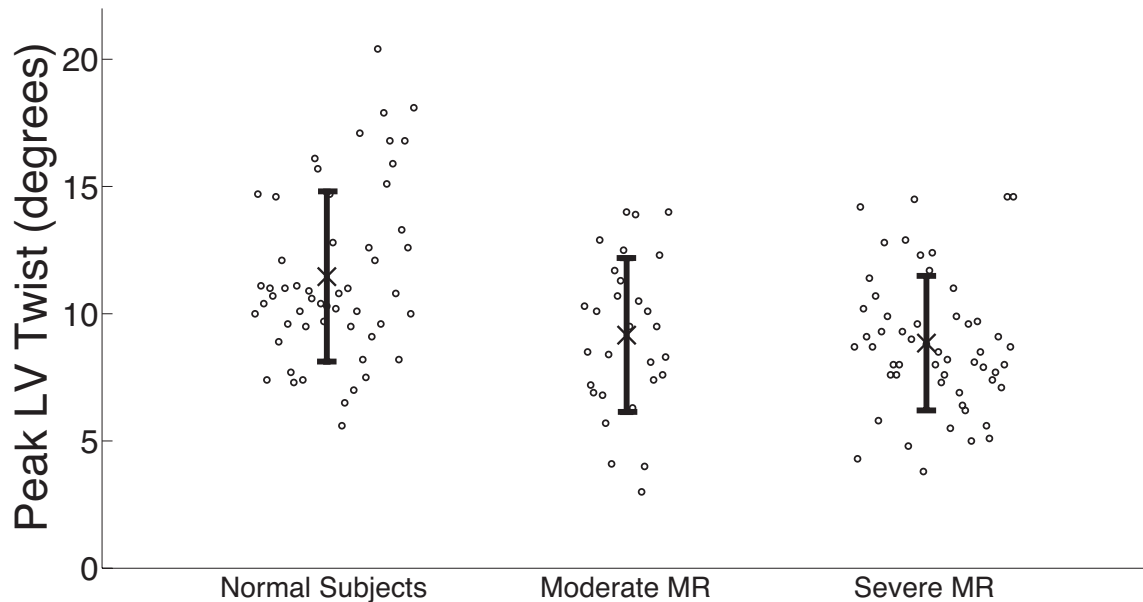


Figure 6.3. Peak LV twist values for normal subjects, moderate MR subjects, and severe MR subjects. The 'X' represents the mean peak LV twist and the error bars represent the standard deviation. LSD only showed significant decreases between the normal subjects and the moderate MR patients and between the normal subjects and the severe MR patients and no difference between the moderate and severe MR patients.

Systolic twist-per-volume

Systolic twist-per-volume slope for normal subjects, moderate MR patients, and severe MR patients was: $-0.14 \pm 0.05^\circ/\text{mL}$, $-0.12 \pm 0.04^\circ/\text{mL}$, and $-0.07 \pm 0.03^\circ/\text{mL}$ respectively. The ANOVA of systolic twist-per-volume slope between the groups showed differences among the groups ($p < 0.0001$) and with respect to weight ($p = 0.006$). LSD

detected significant decreases between normal subjects and moderate MR patients, normal subjects and severe MR patients, and moderate MR patients and severe MR patients. These differences were not associated with patient demographic covariates (age, weight, height, gender). Figure 6.4 illustrates the twist-per-volume data for normal, moderate MR, and severe MR subjects.

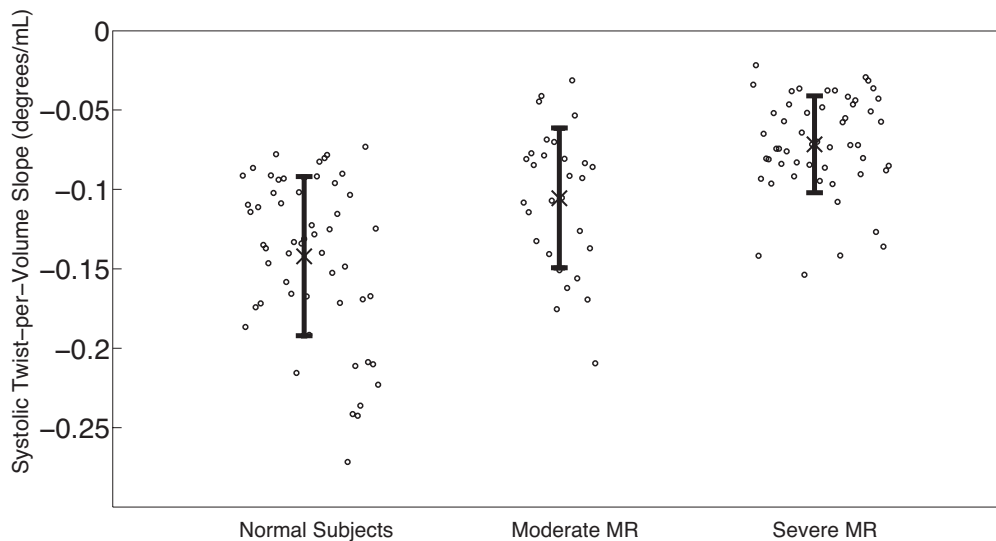


Figure 6.4. Systolic twist-per-volume slope derived from normal subjects, moderate MR subjects and severe MR subjects. The 'X' represents the mean systolic twist-per-volume slope and the error bars represent the standard deviation. LSD detected significant decreases in systolic twist-per-volume slope between normal subjects and moderate MR patients, normal subjects and severe MR patients, and moderate MR patients and severe MR patients.

CL-shear angle

CL-shear angle results and the measured parameters used to estimate CL-shear are summarized in Table 3. Mean peak CL-shear angle for normal subjects, moderate MR

patients, and severe MR patients were: $5.0 \pm 1.4^\circ$, $4.7 \pm 1.6^\circ$, $5.0 \pm 1.3^\circ$ respectively. Additionally, the ANOVA of peak CL-shear angle did not reveal any differences between the three groups ($p=0.7$). Figure 6.5 shows the CL-shear angle results for normal, moderate MR, and severe MR subjects. Figure 6.6 illustrates the peak CL-shear data for normal, moderate MR, and severe MR subjects.

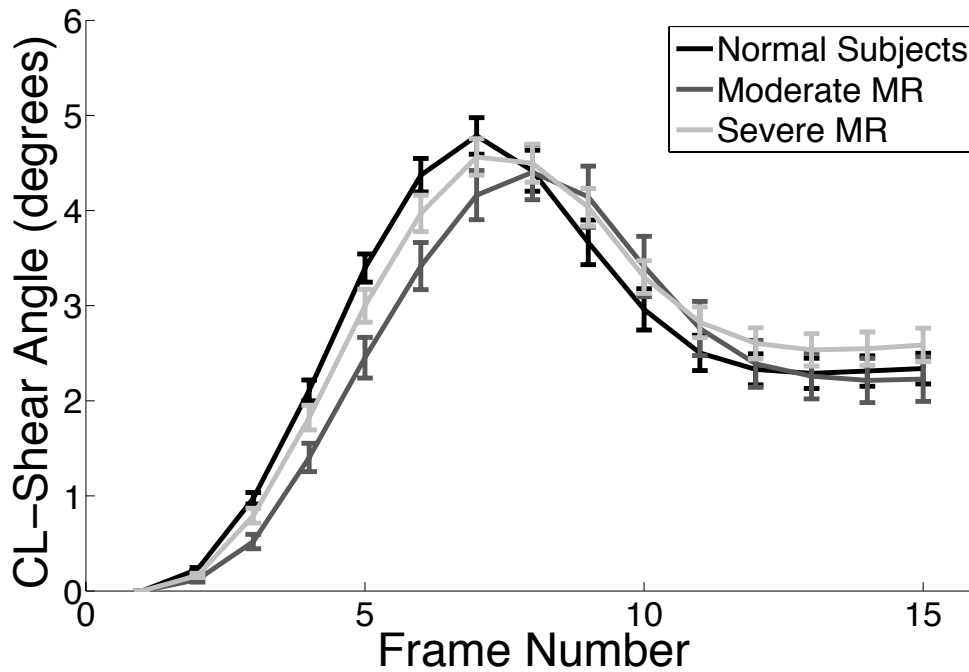


Figure 6.5. CL-shear angle for normal subjects and patients with moderate MR and severe MR during the cardiac cycle. Data curves represent the population mean. Standard error of the mean is used for the error bars for clarity. The magnitude of LV CL-shear angle appears to pseudo-normalize ($P=0.7$).

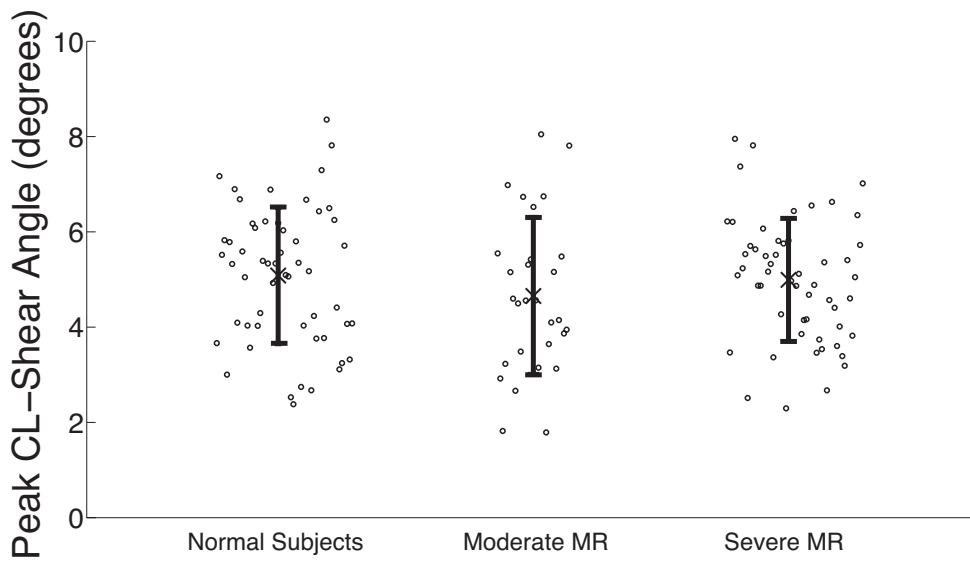


Figure 6.6. Peak LV CL-shear angle for normal subjects, moderate MR subjects, and severe MR subjects. The 'X' represents the mean peak CL-shear angle and the error bars represent the associated standard deviation of the mean. All pairwise comparisons of peak CL-shear angle for normal, moderate MR, and severe MR were considered not significant.

In order to investigate the underlying reason that CL-shear angle measures were similar across the groups the individual measures used to evaluate CL-shear angle were investigated (Table 6.3). LSD showed significant increases between the normal subject group and the severe MR patients and between the moderate MR patients and the severe MR patients for the apical and basal radii. LSD did not detect significant differences between any pair-wise comparison of normal subjects, moderate MR patients, and severe MR patients for the distance between apical and basal slices.

Measurement	Moderate			ANOVA
	Normal	MR	Severe MR	P-Value
Peak CL-shear angle [deg]	5.0±1.4	4.7±1.6	5.0±1.3	P=0.7
Epicardial radius Apex [mm]	20.7±3.1	19.9±3.3	24.9±3.8 ^{†‡}	P<0.0001
Epicardial radius Base [mm]	30.7±3.8	30.7±2.6	35.8±3.2 ^{†‡}	P<0.0001
Distance between Apex and Base [cm]	5.2±0.6	4.8±0.8	4.9±0.6	P=0.1

[†] LSD indicates significant difference from Normal

[‡] LSD indicates significant difference from Moderate

Table 6.3. CL-Shear Angle Measurements

A Hedges' effect size test comparing healthy subjects and patients with moderate MR shows peak twist-per-volume slope (g=0.50), LVESV (g=0.27), LVEDV (g=0.34), LVED mass (g=0.20). Similarly when comparing patients with moderate MR and patients with severe MR the effect size values are: peak twist-per-volume (g=1.67), LVESV (g=0.98), LVEDV (g=1.22), LVED (g=1.25). The comparison shows that peak

twist-per-volume slope has the largest effect size and thus higher discrimination power to detect differences between groups

Discussion

LV twist was shown to decrease significantly in patients with moderate or severe MR. In moderate MR patients this decrease was primarily due to a significant decrease in apical twist, while in patients with severe MR there was a significant reduction in both basal and apical rotations. Ennis *et al.* studied chronic 'pure' MR in sheep using implanted radiopaque markers and demonstrated a significant decrease in both LV twist and in twist-per-volume slope(34). Additionally, Tibayan *et al.* studied the evolution from acute to chronic MR in dogs using videofluoroscopy and radiopaque markers and also observed a decrease in twist after three months of chronic MR(33). Borg *et al.* used speckle tracking echocardiography in patients with chronic primary MR to illustrate that the onset of LV untwist was delayed and untwisting rate was reduced in patients with MR. They did not observe significant differences in LV twist when compared to normal subjects and instead proposed the use of a twist-per-volume slope between peak twist and mitral valve opening, which showed a significant decrease in patients with MR(98). The expected decrease in peak twist paired with the increase in LV volume seen in patients with MR could make the twist-per-volume slope particularly insightful for evaluating the severity of dysfunction. Reduction in LV twist in patients with MR is consistent with previous reports (34,97,106). The decrease in apical rotation may be due to spherical remodeling of the mid-ventricular and apical LV (100). There were not, however, significant differences in peak LV twist between moderate and severe MR

subjects, therefore peak LV twist does not correlate with the severity or progression of MR in this patient cohort. Both moderate and severe MR were associated with significant decreases in the peak untwisting rate, which are consistent with previous literature(98). However, tag fading occurs around 500ms into the cardiac cycle, which makes measuring peak untwisting rate with the temporal resolution of this study challenging.

Peak LV CL-shear angle appeared to pseudo-normalize in patients with MR. The formula for CL-shear angle depends on several factors. The pseudo-normalization of CL-shear angle in moderate and severe MR can be explained by the significant increase in the apical and basal epicardial radii in conjunction with the significant decrease in apical rotation in MR patients compared with normal subjects. The increase in apical and basal epicardial and endocardial radii in the MR patient groups were consistent with the spherical global remodeling previously demonstrated by Schiros *et al* (100). The severe MR patients also had a significant decrease in basal rotation, which further pseudo-normalizes CL-shear angle compared to moderate MR and normal subjects. Additionally, the pseudo-normalization did not occur just for peak CL-shear angle, but was apparent throughout the cardiac cycle (Figure 6.5).

In another study, CL-shear pseudo normalizes with increasing age as a consequence of decreasing twist and increasing ventricular volumes (107). CL-shear angle may not be a suitable imaging biomarker for the detection of LV dysfunction.

For patients with MR, the pseudo-normalization obscured the presence of LV dysfunction and lead to no significant difference between the normal subjects and the MR patients. CL-shear angle may not be a suitable imaging biomarker for the detection

of LV dysfunction in patients with MR, since the measure pseudo-normalizes as a consequence of pathologically increased LV volumes.

We also calculated the Torsion-to-Shortening Ratio (TSR) (108) for a subset of twenty normal subjects, twenty patients with moderate MR and twenty patients with severe MR. TSR was unchanged across groups due to a decrease in torsion and a decrease in shortening.

A significant decrease in the systolic twist-per-volume slope was detected for all pairwise comparisons of the subject groups (severe MR being the smallest), which is consistent with literature (34). Importantly, twist-per-volume slope was the only measure of rotational mechanics that distinguished all three groups. The changes indicate that LV stroke volume increases with respect to MR severity, while twist decreases. This may indicate an energetically unfavorable ejection pattern and lead to exacerbation of the underlying disease (99).

Limitations

Patients and healthy subjects showed some differences in demographics, hence we cannot exclude that this influenced the observed changes in LV (45)rotational mechanics. All studies were performed at 1.5T MR scanner, therefore diastolic rotational information was limited due to tag fading. Performing imaging at 3T MR scanner or using a complementary tagging pattern could improve diastolic estimates. In future studies, the temporal resolution could be improved in order to refine estimates of diastolic rotational mechanics, but this can be difficult to achieve in patients with limited breath hold capacity.

The FAST method has previously been validated using line tags whereas grid tags were used for the reported study. Careful validation of FAST for grid tags is still needed, but as all subjects were imaged with grid tags and analyzed with the same FAST processing method. The comparison between groups is expected to be fair.

Conclusion

The results of this study have shown that systolic twist-per-volume slope was significantly decreased for moderate MR subjects and further decreased for severe MR subjects. Whereas peak LV twist decreases similarly in patients with either moderate or severe MR compared with normal subjects. Therefore, peak systolic twist-per-volume slope may serve as quantitative imaging biomarkers for LV dysfunction in patients with MR.

Acknowledgements

This study was supported in part by AHA 11PRE6080005 to Meral Reyhan, NIH/NHLIB R00-HL087614 to Daniel Ennis and NIH/NHLIB grant P50-HL077100 to Thomas Denney.

Chapter 7 – Single Breath-hold Estimates of Left Ventricular Rotational Mechanics

Introduction

Quantitative measurements of left ventricular (LV) rotational mechanics can be estimated using myocardial tagging (29) and may provide early insight to LV dysfunction before changes in LV ejection fraction (LV-EF). Changes in LV-EF are a late outcome in many cardiovascular diseases and may even be preserved in extreme cases(109). LV peak twist (peak rotational angle difference between the LV apex and the LV base) is a commonly used parameter for evaluating LV rotational mechanics. Current clinical protocols for measuring LV twist therefore require two separate breath hold acquisitions to obtain tagged images at the LV apex and LV base. This subjects estimates of LV twist to inter-breath hold differences. Furthermore, repeated breath holding can become problematic for pediatric patients (e.g. Duchenne muscular dystrophy (110)), chronic obstructive pulmonary disease (111) patients or elderly patients. These patients either have limited breath hold capacity or may become fatigued easily during a multi-breath hold exam. Furthermore, LV twist estimates from images acquired in different breath hold scans can produce measurements that are subject to measurement bias as a consequence of inadvertent, irreproducible, and subtle Valsalva (82) or Mueller (83) maneuvers. All of this limits the accuracy and precision of estimates of LV rotational mechanics that inherently require data obtained in different breath holds. Consequently, an imaging approach that permits the acquisition of multiple slices in a single breath hold, without a significant compromise in spatial or temporal resolution or a concomitant

decrease in contrast-to-noise ratio (CNR) could aid in the evaluation of LV dysfunction in several clinical scenarios.

The recent development of multi-slice excitation permits acquiring more than one slice in a single breath hold using Controlled Aliasing In Parallel Imaging Results In Higher Acceleration (CAIPIRINHA)(112). Compared with the SENSE technique(113), CAIPIRINHA reduces the concomitant g-noise penalty by distributing the aliasing energy more evenly in image space. However, a direct combination of CAIPIRINHA and GRAPPA results in an overlapped image that is extremely hard to resolve using either SENSE or GRAPPA reconstruction methods. This is due to the sharp signal discontinuities in conventional GRAPPA-like frequency domain under sampling techniques (53), when concatenating the field of view (FOV) - shifted reference slices to form the SENSE/GRAPPA calibration data. These signal discontinuities can lead to phase errors in the reconstructed image. As a solution, Setsompop et al. have proposed slice-GRAPPA(114), which fits GRAPPA-like kernels to each slice from the pre-scan calibration data sets. These kernels are then used to estimate the k-space data of each individual imaging slice from the under sampled k-space data. Slice-GRAPPA method resolves the images with preserved quality and SNR.

In this study we combine CAIPIRINHA with a cardiac gated, non-selective tagging sequence, to acquire LV twist measurements in a single breath hold. Image is reconstructed using the slice-GRAPPA method. The objective of this study was to eliminate intra-scan error and to validate the CAIPIRINHA LV twist estimates and reproducibility in healthy volunteers.

Methods

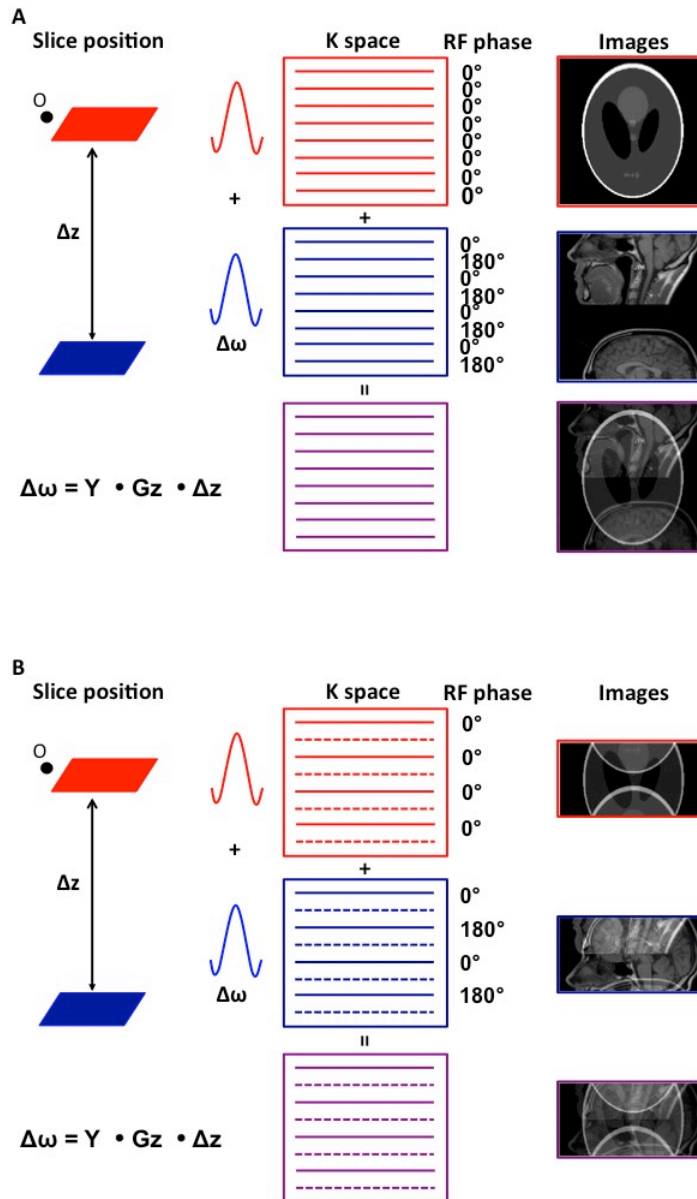


Figure 7.1 Diagram of the simultaneous two-slice excitation and RF pulse phase interleaving scheme, the concomitant k-space acquisition scheme, and the acquired aliased images for CAIPI rate-2 ($R=2$) acceleration (A) and CAIPI rate-2 + GRAPPA rate-2 acceleration ($R=4$) (B).

We propose a CAIPIRINHA plus cardiac tagging approach wherein the non-selective cardiac tagging preparation pulses were followed by a combination of two imaging pulses: RF_1 (red) and RF_2 (blue) with a frequency offset of $\Delta\omega$ (Figure 7.1). RF_1 is used to acquire the odd k_y lines and has constant 0° phase (red plane), while RF_2 has alternating 0° and 180° interleaved phases (blue plane). During image acquisition the two RF pulse are summed together (purple) to excite two slices simultaneously. The frequency difference between the two pulses was calculated as:

$$\Delta\omega = \gamma G \Delta z \quad \text{Eq. 7.1}$$

where γ is the gyromagnetic ratio, Δz is distance between the two slices and G is the amplitude of the slice selection gradient.

A SPOiled GRAdient (SPGR) echo tagging sequence, which generates grid tag patterns throughout the heart, was modified to support CAIPIRINHA. The sequence was evaluated in an IRB approved study after obtaining informed consent in ten (N=10) healthy human subjects. All subjects were scanned on a Siemens Avanto 1.5T scanner (Siemens Healthcare, Erlangen, Germany) with a six-element body matrix coil in combination with a six-element spine coil.

Subsequent to localizing the subject's heart, the LV apical and basal imaging planes were defined as the most apical or basal images wherein the blood pool was visible in all cardiac phases and wherein the LV myocardium maintained an annular shape during the entire cardiac cycle. Images were acquired with the following parameters: 330-400x330-400mm FOV, 5mm slice thickness TE/TR = 4.5/5.3ms, 12° imaging flip angle 192x192 acquisition matrix, 250 Hz/pixel bandwidth, and 8 mm tag spacing. Three groups of images were acquired at the apical and basal level of the heart and are

compared in Results section: Scan-1) Traditional SPAMM grid tagged images with GRAPPA-2, but without CAIPIRINHA were acquired in two separate breath holds. These images were used as the “gold standard” reference images(115). The total scan time for Scan-1 was 28 seconds (2 x 14 seconds) for both apical and basal images. Scan-2) SPAMM grid tagged images without GRAPPA-2, but with two-slice CAIPIRINHA were acquired in a single breath hold. The scan time for Scan-2 was 20 seconds for both apical and basal images. Scan-3) SPAMM grid tagged images with simulated GRAPPA-2 + CAIPIRINHA were generated from two sets of fully sampled images acquired using two-slice CAIPIRINHA. The raw data was retrospectively under-sampled and combined to simulate GRAPPA 2 scheme.

Two single shot images with one cardiac phase were also acquired using the GRE FLASH sequence at the apical and basal level. Coil sensitivity weighting was extracted from the two single shot GRE images for further image reconstruction steps. Both Group B and Group C images were reconstructed using a Matlab (Mathworks, Natick, MA, USA) CAIPIRINHA toolbox(114).

Images in group A, B and C were acquired twice to test the intra scan reproducibility. Imaging sequence order was randomized to minimize ordering bias, which could be introduced by heart rate variation due to repeated breath-holds. LV twist measurements were calculated using the FAST method (55). Paired t-test with $P < 0.05$ were used to detect significant differences in LV peak twist between the two methods.

RESULTS

In vivo images

Figure 7.2 shows the cardiac tagged images for group A (separate breath-hold scans), group B (CAIPIRINHA rate-2), and group C (CAIPIRINHA rate-2 + GRAPPA rate-2). Overall, the images showed good slice-separation in all subjects with slightly amplified noise.

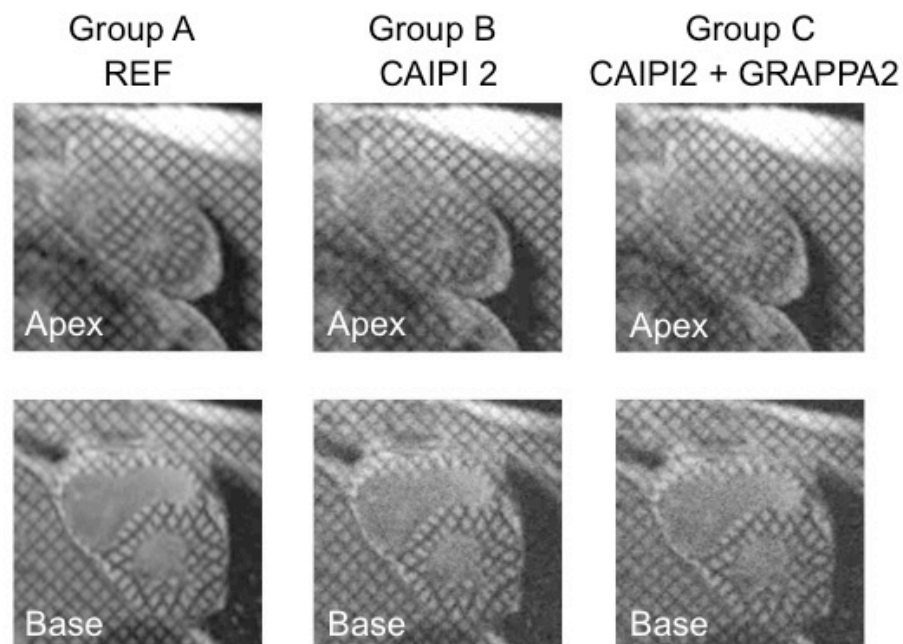


Figure 7.2 LV apical and basal grid tagged images acquired with separate breath hold (REF), CAIPIRINHA rate-2 (CAIPI-2), and CAIPIRINHA rate-2 plus GRAPPA rate-2 (CAIPI2+GRAPPA2). The CAIPIRINHA-based images demonstrated good slice separation between basal and apical slices.

LV twist calculation

Figure 7.3 shows the mean LV twist results from ten (N=10) healthy volunteers using the conventional grid tagged method (blue curve), the CAIPIRINHA rate-2 grid tagged method (red curve) and the CAIPIRINHA rate-2 plus GRAPPA rate-2 (black). The blue and black curves are slightly shifted along the time-axes to avoid overlap between the

two curves.

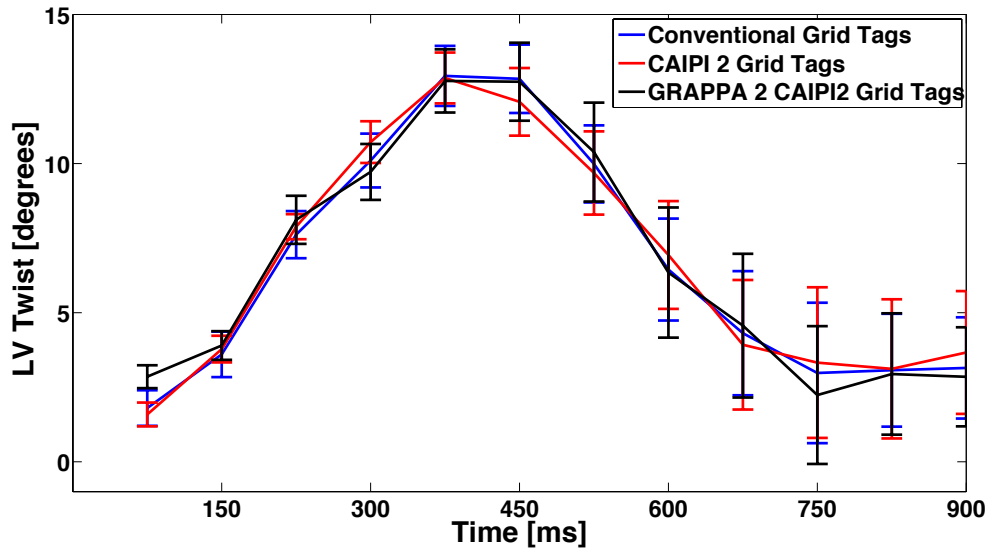


Figure 7.3 Comparison of LV twist estimates between the CAIPIRINHA grid tagged images with or without GRAPPA-based acceleration and conventional grid tagged images.

Mean LV PT (°)	(REF)	(CAIPI-2)	(CAIPI-2 + GRAPPA 2)
Measure 1	13.4±3.7	14.2±2.3	13.6±2.9
Measure 2	14.0±4.5	13.9±2.7	14.1±3.6

Table 7.1 Mean LV peak twist for healthy subjects (N=10).

	(REF)	(CAIPI-2)	(CAIPI-2 + GRAPPA 2)
Δ LV-PT (°)	0.6±0.8	0.3±0.4	0.5±0.7

Table 7.2 Intra-exam LV peak twist (LV-PT) difference between two acquisitions.

Table 7.1 shows that the mean LV peak twist results from the two measurements were not significantly different. Paired t-test shows no significant difference between REF and CAIPI-2 ($p=0.43$); REF and CAIPI-2 + GRAPPA-2 ($p=0.55$); and CAIPI-2 vs CAIPI-2+ GRAPPA-2 ($p=0.48$). The reproducibility test results are summarized in Table 7.2. Intra-exam LV peak twist differences shows that the CAIPI-2 reproducibility had the smallest mean and standard deviation while the REF group had the largest value.

Discussion

In this work, a generalized implementation of multi-slice SPGR imaging of cardiac tagged slices was presented. Using this approach the total number of scan sequences needed for LV twist measurements can be reduced by half. This has the advantage of reducing the time needed to acquire the images during a clinical exam and also reduces the chances of clinically relevant intra-breath hold confounders on measurements of LV rotational mechanics. CAIPIRINHA and cardiac tagging are complementary techniques because the tagging pulses are non-selective. Our analysis shows high agreement between CAIPIRINHA and non- CAIPIRINHA methods. Consequently, CAIPIRINHA and cardiac tagging can be combined for single breath hold acquisitions of multiple short-axis imaging planes and used to rapidly measure LV twist with the FAST technique. Paired t-tests of mean LV peak twist showed no significant difference

between each method. However, reproducibility test showed that CAIPI-2 had the smallest difference and thus is more reproducible compared with traditional two breath-holds method. Subtle intrathoracic pressure differences between different breath holds may affect cardiac preload or afterload conditions and further subtly impact LV twist results.

CONCLUSION

The combination of CAIPIRINHA with an LV tagging sequence can achieve similar estimates of peak LV twist in a single breath hold, which simplifies the exam and avoids measurement differences that may arise from data acquired in different breath holds.

Chapter 8 Thesis Summary

This thesis focuses on the quantitative evaluation of LV rotational mechanics in both healthy volunteers and patients, which could be potentially used as sensitive biomarkers for early disease diagnosis, prognosis, and in the evaluation of therapeutic response. While current clinical MRI exams use both breath-hold and free breathing techniques to acquire images, LV rotational mechanics shows significant difference between the two. Free breathing is the preferred technique and is recommended for future applications.

Complementary radial tagging (CRT) has a tag pattern that better fits the annular-shaped LV myocardium in the short-axis view with enhanced tag contrast through the entire cardiac cycle. It could be used to accurately evaluate LV rotational mechanics in the middle or late diastolic phases, but the extended acquisition time poses a significant limitation for patients with limited breath hold capacity. Combining a free-breathing approach with a CRT approach would be a logical next step.

The combined use of simultaneous multi-slice (SMS) imaging with cardiac MRI tagging permits reducing the total number of scans needed for LV rotational mechanics evaluation by half and is especially well chosen for measurements that require acquisition of two parallel and distant slices. All three techniques (free-breathing, CRT, and SMS) described in this thesis could be further combined. The ultimate goal would be a free breathing CRT approach with SMS for more accurate and faster LV rotational mechanics evaluation during free breathing.

Reference:

1. Agur KLMAFDAMR. Clinically Oriented Anatomy 7th Edition: Wolters Kluwer Health/Lippincott Williams & Wilkins; 2013.
2. Taber LA. Biomechanics of cardiovascular development. Annual Review of Biomedical Engineering 2001;3:1-25.
3. Betts JG. Anatomy & physiology OpenStax College; 2013.
4. Larsen W. Embriologia Humana. Elsevier Science 2003:177.
5. Sengupta PP, Korinek J, Belohlavek M, Narula J, Vannan MA, Jahangir A, Khandheria BK. Left ventricular structure and function: basic science for cardiac imaging. Journal of the American College of Cardiology 2006;48(10):1988-2001.
6. Dubose TJ. Embryonic Heart Rate and Age. JJournal of Diagnostic Medical Sonography 1990;6(3):151-157.
7. Karvonen J, Vuorimaa T. Heart rate and exercise intensity during sports activities. Practical application. Sports medicine 1988;5(5):303-311.
8. Guyton ACH, J.E. Textbook of Medical Physiology206.
9. Berne RM, Levy MN. Cardiovascular physiology. St. Louis: Mosby; 1997. xi, 324 p. p.
10. Hurst JW. Naming of the waves in the ECG, with a brief account of their genesis. Circulation 1998;98(18):1937-1942.
11. Anderson RH, Ho SY, Redmann K, Sanchez-Quintana D, Lunkenheimer PP. The anatomical arrangement of the myocardial cells making up the ventricular mass. European Journal of Cardio-Thoracic Surgery 2005;28(4):517-525.

12. Taber LA, Yang M, Podszus WW. Mechanics of ventricular torsion. *J Biomech* 1996;29(6):745-752.
13. Sengupta PP, Tajik AJ, Chandrasekaran K, Khandheria BK. Twist mechanics of the left ventricle: principles and application. *JACC Cardiovasc Imaging* 2008;1(3):366-376.
14. Chen JJ, Liu W, Zhang HY, Lacy L, Yang XX, Song SK, Wickline SA, Yu X. Regional ventricular wall thickening reflects changes in cardiac fiber and sheet structure during contraction: quantification with diffusion tensor MRI. *American Journal of Physiology-Heart and Circulatory Physiology* 2005;289(5):H1898-H1907.
15. Edelman RR, Gaa J, Wedeen VJ, Loh E, Hare JM, Prasad P, Li W. In vivo measurement of water diffusion in the human heart. *Magnetic resonance in medicine : official journal of the Society of Magnetic Resonance in Medicine / Society of Magnetic Resonance in Medicine* 1994;32(3):423-428.
16. Kung GL, Nguyen TC, Itoh A, Skare S, Ingels NB, Jr., Miller DC, Ennis DB. The presence of two local myocardial sheet populations confirmed by diffusion tensor MRI and histological validation. *J Magn Reson Imaging*;34(5):1080-1091.
17. Ingels NB, Jr., Hansen DE, Daughters GT, 2nd, Stinson EB, Alderman EL, Miller DC. Relation between longitudinal, circumferential, and oblique shortening and torsional deformation in the left ventricle of the transplanted human heart. *Circ Res* 1989;64(5):915-927.
18. Sengupta PP, Khandheria BK, Korinek J, Wang JW, Jahangir A, Seward JB, Belohlavek M. Apex-to-base dispersion in regional timing of left ventricular

- shortening and lengthening. *Journal of the American College of Cardiology* 2006;47(1):163-172.
19. Arts T, Veenstra PC, Reneman RS. Epicardial deformation and left ventricular wall mechanisms during ejection in the dog. *Am J Physiol* 1982;243(3):H379-390.
 20. Aelen FW, Arts T, Sanders DG, Thelissen GR, Muijtjens AM, Prinzen FW, Reneman RS. Relation between torsion and cross-sectional area change in the human left ventricle. *J Biomech* 1997;30(3):207-212.
 21. Russel IK, Tecelao SR, Kuijjer JP, Heethaar RM, Marcus JT. Comparison of 2D and 3D calculation of left ventricular torsion as circumferential-longitudinal shear angle using cardiovascular magnetic resonance tagging. *J Cardiovasc Magn Reson* 2009;11:8.
 22. Young AA, Cowan BR. Evaluation of left ventricular torsion by cardiovascular magnetic resonance. *J Cardiovasc Magn Reson* 2012;14(1):49.
 23. Melacini P, Basso C, Angelini A, Calore C, Bobbo F, Tokajuk B, Bellini N, Smaniotto G, Zucchetto M, Iliceto S, Thiene G, Maron BJ. Clinicopathological profiles of progressive heart failure in hypertrophic cardiomyopathy. *European heart journal* 2010;31(17):2111-2123.
 24. Nagel E, Stuber M, Burkhard B, Fischer SE, Scheidegger MB, Boesiger P, Hess OM. Cardiac rotation and relaxation in patients with aortic valve stenosis. *Eur Heart J* 2000;21(7):582-589.

25. Stuber M, Scheidegger MB, Fischer SE, Nagel E, Steinemann F, Hess OM, Boesiger P. Alterations in the local myocardial motion pattern in patients suffering from pressure overload due to aortic stenosis. *Circulation* 1999;100(4):361-368.
26. Popescu BA, Beladan CC, Calin A, Muraru D, Deleanu D, Rosca M, Ginhina C. Left ventricular remodelling and torsional dynamics in dilated cardiomyopathy: reversed apical rotation as a marker of disease severity. *European journal of heart failure* 2009;11(10):945-951.
27. Kanzaki H, Nakatani S, Yamada N, Urayama S, Miyatake K, Kitakaze M. Impaired systolic torsion in dilated cardiomyopathy: reversal of apical rotation at mid-systole characterized with magnetic resonance tagging method. *Basic Res Cardiol* 2006;101(6):465-470.
28. Young AA, Kramer CM, Ferrari VA, Axel L, Reichek N. Three-dimensional left ventricular deformation in hypertrophic cardiomyopathy. *Circulation* 1994;90(2):854-867.
29. Ennis DB, Epstein FH, Kellman P, Fananapazir L, McVeigh ER, Arai AE. Assessment of regional systolic and diastolic dysfunction in familial hypertrophic cardiomyopathy using MR tagging. *Magn Reson Med* 2003;50(3):638-642.
30. Muntoni F, Torelli S, Ferlini A. Dystrophin and mutations: one gene, several proteins, multiple phenotypes. *The Lancet Neurology* 2003;2(12):731-740.
31. Frankel KA, Rosser RJ. The pathology of the heart in progressive muscular dystrophy: epimyocardial fibrosis. *Human pathology* 1976;7(4):375-386.

32. Lammerding J, Lee RT. Torn apart: membrane rupture in muscular dystrophies and associated cardiomyopathies. *The Journal of clinical investigation* 2007;117(7):1749-1752.
33. Tibayan FA, Yun KL, Fann JI, Lai DT, Timek TA, Daughters GT, Ingels NB, Miller DC. Torsion dynamics in the evolution from acute to chronic mitral regurgitation. *J Heart Valve Dis* 2002;11(1):39-46; discussion 46.
34. Ennis DB, Nguyen TC, Itoh A, Bothe W, Liang DH, Ingels NB, Miller DC. Reduced systolic torsion in chronic "pure" mitral regurgitation. *Circ Cardiovasc Imaging* 2009;2(2):85-92.
35. Dong SJ, Hees PS, Huang WM, Buffer SA, Jr., Weiss JL, Shapiro EP. Independent effects of preload, afterload, and contractility on left ventricular torsion. *The American journal of physiology* 1999;277(3 Pt 2):H1053-1060.
36. Notomi Y, Srinath G, Shiota T, Martin-Miklovic MG, Beachler L, Howell K, Oryszak SJ, Deserranno DG, Freed AD, Greenberg NL, Younoszai A, Thomas JD. Maturation and adaptive modulation of left ventricular torsional biomechanics: Doppler tissue imaging observation from infancy to adulthood. *Circulation* 2006;113(21):2534-2541.
37. Haacke EM, Brown R, Thompson M, Venkatesan R. *Magnetic Resonance Imaging: Physical Principles and Sequence Design*. New York: Wiley-Liss; 1999.
38. Liang ZP, Lauterbur PC. *Principles of Magnetic Resonance Imaging: A Signal Processing Perspective*. Akay M, editor. New York: IEEE Press; 2000.
39. Bernstein MA, King KE, Zhou XJ. *Handbook of MRI Pulse Sequences*. San Diego: Elsevier Academic Press; 2004.

40. Kwong RY. Cardiovascular Magnetic Resonance Imaging. Cannon CP, editor. Totowa: Humana Press; 2008.
41. Lee S, Yang DS, Choi MS, Kim CY. Development of respiratory motion reduction device system (RMRDs) for radiotherapy in moving tumors. Japanese journal of clinical oncology 2004;34(11):686-691.
42. Kaneko H, Horie J. Breathing movements of the chest and abdominal wall in healthy subjects. Respiratory care 2012;57(9):1442-1451.
43. Axel L, Dougherty L. MR imaging of motion with spatial modulation of magnetization. Radiology 1989;171(3):841-845.
44. Herzka DA, Guttman MA, McVeigh ER. Myocardial tagging with SSFP. Magnetic Resonance in Medicine 2003;49(2):329-340.
45. Fischer SE, McKinnon GC, Maier SE, Boesiger P. Improved myocardial tagging contrast. Magn Reson Med 1993;30(2):191-200.
46. Stuber M, Spiegel MA, Fischer SE, Scheidegger MB, Danias PG, Pedersen EM, Boesiger P. Single breath-hold slice-following CSPAMM myocardial tagging. Magma 1999;9(1-2):85-91.
47. Zerhouni EA, Parish DM, Rogers WJ, Yang A, Shapiro EP. Human heart: tagging with MR imaging--a method for noninvasive assessment of myocardial motion. Radiology 1988;169(1):59-63.
48. Nasiraei-Moghaddam A, Finn JP. Tagging of cardiac magnetic resonance images in the polar coordinate system: Physical principles and practical implementation. Magnetic Resonance in Medicine 2013:doi:10.1002/mrm.24839.

49. Fonseca CG, Backhaus M, Bluemke DA, Britten RD, Chung JD, Cowan BR, Dinov ID, Finn JP, Hunter PJ, Kadish AH, Lee DC, Lima JA, Medrano-Gracia P, Shivkumar K, Suinesiaputra A, Tao W, Young AA. The Cardiac Atlas Project--an imaging database for computational modeling and statistical atlases of the heart. *Bioinformatics* 2011;27(16):2288-2295. doi: 2210.1093/bioinformatics/btr2360. Epub 2011 Jul 2286.
50. Walker PM, Marie PY, Mezeray C, Bessieres M, Escanye JM, Karcher G, Danchin N, Mattei S, Villemot JP, Bertrand A. Synchronized inversion recovery-spin echo sequences for precise in vivo T1 measurement of human myocardium: a pilot study on 22 healthy subjects. *Magn Reson Med* 1993;29(5):637-641.
51. Kellman P, Arai AE, Xue H. T1 and extracellular volume mapping in the heart: estimation of error maps and the influence of noise on precision. *Journal of cardiovascular magnetic resonance : official journal of the Society for Cardiovascular Magnetic Resonance* 2013;15:56.
52. Di Donato M, Dabic P, Castelvechio S, Santambrogio C, Brankovic J, Collarini L, Joussef T, Frigiola A, Buckberg G, Menicanti L, the RG. Left ventricular geometry in normal and post-anterior myocardial infarction patients: sphericity index and 'new' conicity index comparisons. *European Journal of Cardio-Thoracic Surgery* 2006;29(Supplement 1):S225-S230.
53. Griswold MA, Jakob PM, Heidemann RM, Nittka M, Jellus V, Wang J, Kiefer B, Haase A. Generalized autocalibrating partially parallel acquisitions (GRAPPA). *Magnetic Resonance in Medicine* 2002;47(6):1202-1210.

54. Reyhan M, Natsuaki Y, Ennis DB. Off-resonance insensitive complementary SPAtial Modulation of Magnetization (ORI-CSPAMM) for quantification of left ventricular twist. *Journal of Magnetic Resonance Imaging* 2014;39(2):339-345.
55. Reyhan M, Natsuaki Y, Ennis DB. Fourier analysis of STimulated echoes (FAST) for the quantitative analysis of left ventricular twist. *Journal of Magnetic Resonance Imaging* 2012;35(3):587-593.
56. Sengupta PP, Tajik AJ, Chandrasekaran K, Khandheria BK. Twist Mechanics of the Left Ventricle: Principles and Application. *JACC: Cardiovascular Imaging* 2008;1(3):366-376.
57. Dietrich O, Raya JG, Reeder SB, Reiser MF, Schoenberg SO. Measurement of signal-to-noise ratios in MR images: Influence of multichannel coils, parallel imaging, and reconstruction filters. *Journal of Magnetic Resonance Imaging* 2007;26(2):375-385.
58. Jovicich J, Czanner S, Greve D, Haley E, van der Kouwe A, Gollub R, Kennedy D, Schmitt F, Brown G, MacFall J, Fischl B, Dale A. Reliability in multi-site structural MRI studies: Effects of gradient non-linearity correction on phantom and human data. *NeuroImage* 2006;30(2):436-443.
59. Razieh Kaveh ANM, Sarah N Khan, J Finn Paul. Regional rotation of the left ventricle in healthy and cardiomyopathic subjects measured with radial myocardial tagging. *Journal of Cardiovascular Magnetic Resonance* 2014;16 (Suppl 1):P24.
60. Emery AE. Population frequencies of inherited neuromuscular diseases--a world survey. *Neuromuscular disorders* : NMD 1991;1(1):19-29.

61. Mann CJ, Perdiguero E, Kharraz Y, Aguilar S, Pessina P, Serrano AL, Munoz-Canoves P. Aberrant repair and fibrosis development in skeletal muscle. *Skeletal muscle* 2011;1(1):21.
62. Bushby K, Finkel R, Birnkrant DJ, Case LE, Clemens PR, Cripe L, Kaul A, Kinnett K, McDonald C, Pandya S, Poysky J, Shapiro F, Tomezsko J, Constantin C, Group DMDCCW. Diagnosis and management of Duchenne muscular dystrophy, part 2: implementation of multidisciplinary care. *The Lancet Neurology* 2010;9(2):177-189.
63. Nigro G, Comi LI, Politano L, Bain RJ. The incidence and evolution of cardiomyopathy in Duchenne muscular dystrophy. *International journal of cardiology* 1990;26(3):271-277.
64. Gulel O, Soylu K, Yuksel S, Karaoglanoglu M, Cengiz K, Dilek M, Hamiseyev C, Kale A, Arik N. Evidence of left ventricular systolic and diastolic dysfunction by color tissue Doppler imaging despite normal ejection fraction in patients on chronic hemodialysis program. *Echocardiography* 2008;25(6):569-574.
65. Zagatina A, Zhuravskaya N, Kotelnikova A. Application of tissue Doppler to interpretation of exercise echocardiography: diagnostics of ischemia localization in patients with ischemic heart disease. *Eur J Echocardiogr* 2007;8(6):463-469.
66. Huang CH, Tsai MS, Hsieh CC, Wang TD, Chang WT, Chen WJ. Diagnostic accuracy of tissue Doppler echocardiography for patients with acute heart failure. *Heart* 2006;92(12):1790-1794.

67. Devlin AM, Moore NR, Ostman-Smith I. A comparison of MRI and echocardiography in hypertrophic cardiomyopathy. *The British journal of radiology* 1999;72(855):258-264.
68. Willig TN, Carlier L, Legrand M, Riviere H, Navarro J. Nutritional assessment in Duchenne muscular dystrophy. *Developmental medicine and child neurology* 1993;35(12):1074-1082.
69. Oda T, Shimizu N, Yonenobu K, Ono K, Nabeshima T, Kyoh S. Longitudinal study of spinal deformity in Duchenne muscular dystrophy. *Journal of pediatric orthopedics* 1993;13(4):478-488.
70. Mondillo S, Galderisi M, Mele D, Cameli M, Lomoriello VS, Zaca V, Ballo P, D'Andrea A, Muraru D, Losi M, Agricola E, D'Errico A, Buralli S, Sciomer S, Nistri S, Badano L, Echocardiography Study Group Of The Italian Society Of C. Speckle-tracking echocardiography: a new technique for assessing myocardial function. *Journal of ultrasound in medicine : official journal of the American Institute of Ultrasound in Medicine* 2011;30(1):71-83.
71. Lima JA, Judd RM, Bazille A, Schulman SP, Atalar E, Zerhouni EA. Regional heterogeneity of human myocardial infarcts demonstrated by contrast-enhanced MRI. Potential mechanisms. *Circulation* 1995;92(5):1117-1125.
72. Kim RJ, Wu E, Rafael A, Chen EL, Parker MA, Simonetti O, Klocke FJ, Bonow RO, Judd RM. The use of contrast-enhanced magnetic resonance imaging to identify reversible myocardial dysfunction. *The New England journal of medicine* 2000;343(20):1445-1453.

73. Moon JC, Treibel TA, Schelbert EB. T1 mapping for diffuse myocardial fibrosis: a key biomarker in cardiac disease? *Journal of the American College of Cardiology* 2013;62(14):1288-1289.
74. Robbers-Visser D, Boersma E, Helbing WA. Normal biventricular function, volumes, and mass in children aged 8 to 17 years. *J Magn Reson Imaging* 2009;29(3):552-559.
75. Sarikouch S, Peters B, Gutberlet M, Leismann B, Kelter-Kloepping A, Koerperich H, Kuehne T, Beerbaum P. Sex-specific pediatric percentiles for ventricular size and mass as reference values for cardiac MRI: assessment by steady-state free-precession and phase-contrast MRI flow. *Circ Cardiovasc Imaging* 2010;3(1):65-76.
76. White SK, Sado DM, Flett AS, Moon JC. Characterising the myocardial interstitial space: the clinical relevance of non-invasive imaging. *Heart* 2012;98(10):773-779.
77. Thompson RB, Paterson I, Chow K, Cheng-Baron J, Scott JM, Esch BT, Ennis DB, Haykowsky MJ. Characterization of the relationship between systolic shear strain and early diastolic shear strain rates: insights into torsional recoil. *American Journal of Physiology - Heart and Circulatory Physiology* 2010;299(3):H898-H907.
78. Osman NF, Kerwin WS, McVeigh ER, Prince JL. Cardiac motion tracking using CINE harmonic phase (HARP) magnetic resonance imaging. *Magnetic resonance in medicine : official journal of the Society of Magnetic Resonance in Medicine / Society of Magnetic Resonance in Medicine* 1999;42(6):1048-1060.

79. Aletras AH, Ding S, Balaban RS, Wen H. DENSE: displacement encoding with stimulated echoes in cardiac functional MRI. *Journal of magnetic resonance* 1999;137(1):247-252.
80. Simonds AK. Respiratory complications of the muscular dystrophies. *Seminars in respiratory and critical care medicine* 2002;23(3):231-238.
81. Herzka DA, Derbyshire JA, Kellman P, McVeigh ER. Single heartbeat cardiac tagging for the evaluation of transient phenomena. *Magnetic resonance in medicine : official journal of the Society of Magnetic Resonance in Medicine / Society of Magnetic Resonance in Medicine* 2005;54(6):1455-1464.
82. Gorlin R, Knowles JH, Storey CF. The Valsalva maneuver as a test of cardiac function; pathologic physiology and clinical significance. *The American journal of medicine* 1957;22(2):197-212.
83. Condos WR, Jr., Latham RD, Hoadley SD, Pasipoularides A. Hemodynamics of the Mueller maneuver in man: right and left heart micromanometry and Doppler echocardiography. *Circulation* 1987;76(5):1020-1028.
84. Zhong X, Spottiswoode BS, Meyer CH, Kramer CM, Epstein FH. Imaging three-dimensional myocardial mechanics using navigator-gated volumetric spiral cine DENSE MRI. *Magnetic resonance in medicine : official journal of the Society of Magnetic Resonance in Medicine / Society of Magnetic Resonance in Medicine* 2010;64(4):1089-1097.
85. Santelli C, Nezafat R, Goddu B, Manning WJ, Smink J, Kozerke S, Peters DC. Respiratory bellows revisited for motion compensation: preliminary experience for cardiovascular MR. *Magnetic resonance in medicine : official journal of the*

- Society of Magnetic Resonance in Medicine / Society of Magnetic Resonance in Medicine 2011;65(4):1097-1102.
86. Jin N, Lewandowski RJ, Omary RA, Larson AC. Respiratory self-gating for free-breathing abdominal phase-contrast blood flow measurements. *J Magn Reson Imaging* 2009;29(4):860-868.
 87. Reyhan M, Kim HJ, Brown MS, Ennis DB. Intra- and interscan reproducibility using Fourier Analysis of STimulated Echoes (FAST) for the rapid and robust quantification of left ventricular twist. *J Magn Reson Imaging* 2014;39(2):463-468.
 88. Sampath S, Derbyshire JA, Atalar E, Osman NF, Prince JL. Real-time imaging of two-dimensional cardiac strain using a harmonic phase magnetic resonance imaging (HARP-MRI) pulse sequence. *Magn Reson Med* 2003;50(1):154-163.
 89. Reyhan MK, H. Ennis, DB. . Left Ventricular Twist , but not Circumferential-Longitudinal Shear Angle Increases with Increasing Age in Normal Subjects. 2013; San Francisco California.
 90. Kellman P, Ched'hotel C, Lorenz CH, Mancini C, Arai AE, McVeigh ER. Fully automatic, retrospective enhancement of real-time acquired cardiac cine MR images using image-based navigators and respiratory motion-corrected averaging. *Magnetic resonance in medicine : official journal of the Society of Magnetic Resonance in Medicine / Society of Magnetic Resonance in Medicine* 2008;59(4):771-778.
 91. Venkatesh BA, Gupta H, Lloyd SG, Dell 'Italia L, Denney TS, Jr. 3D left ventricular strain from unwrapped harmonic phase measurements. *J Magn Reson Imaging* 2010;31(4):854-862.

92. Hor KN, Wansapura J, Markham LW, Mazur W, Cripe LH, Fleck R, Benson DW, Gottliebson WM. Circumferential strain analysis identifies strata of cardiomyopathy in Duchenne muscular dystrophy: a cardiac magnetic resonance tagging study. *Journal of the American College of Cardiology* 2009;53(14):1204-1210.
93. Mazur W, Hor KN, Germann JT, Fleck RJ, Al-Khalidi HR, Wansapura JP, Chung ES, Taylor MD, Jefferies JL, Benson DW, Gottliebson WM. Patterns of left ventricular remodeling in patients with Duchenne Muscular Dystrophy: a cardiac MRI study of ventricular geometry, global function, and strain. *The international journal of cardiovascular imaging* 2012;28(1):99-107.
94. Perloff Jk Fau - Roberts WC, Roberts WC. The mitral apparatus. Functional anatomy of mitral regurgitation. *Circulation* 1972;46(2):227-239.
95. Moustafa SE, Kansal M, Alharthi M, Deng Y, Chandrasekaran K, Mookadam F. Prediction of incipient left ventricular dysfunction in patients with chronic primary mitral regurgitation: a velocity vector imaging study. *European journal of echocardiography : the journal of the Working Group on Echocardiography of the European Society of Cardiology* 2011;12(4):291-298.
96. Kazui T, Niinuma H, Tsuboi J, Okabayashi H. Changes in left ventricular twist after mitral valve repair. *J Thorac Cardiovasc Surg* 2010;141(3):716-724.
97. Shudo Y, Nakatani S, Sakaguchi T, Miyagawa S, Yoshikawa Y, Takeda K, Saito S, Takeda Y, Sakata Y, Yamamoto K, Sawa Y. Left ventricular mechanics following restrictive mitral annuloplasty for functional mitral regurgitation: two-

- dimensional speckle tracking echocardiographic study. *Echocardiography* 2012;29(4):445-450.
98. Borg AN, Harrison JL, Argyle RA, Ray SG. Left ventricular torsion in primary chronic mitral regurgitation. *Heart* 2008;94(5):597-603.
99. Bovendeerd PH, Arts T, Huyghe JM, van Campen DH, Reneman RS. Dependence of local left ventricular wall mechanics on myocardial fiber orientation: a model study. *J Biomech* 1992;25(10):1129-1140.
100. Schiros CG, Dell'Italia LJ, Gladden JD, Clark D, 3rd, Aban I, Gupta H, Lloyd SG, McGiffin DC, Perry G, Denney TS, Jr., Ahmed MI. Magnetic resonance imaging with 3-dimensional analysis of left ventricular remodeling in isolated mitral regurgitation: implications beyond dimensions. *Circulation* 2012;125(19):2334-2342.
101. Guttman MA, Zerhouni EA, McVeigh ER. Analysis of Cardiac Function from MR Images. *IEEE computer graphics and applications* 1997;17(1):30-38.
102. Khorsand A, Graf S, Frank H, Kletter K, Sochor H, Maurer G, Schuster E, Globits S, Dudczak R, Porenta G. Model-based analysis of electrocardiography-gated cardiac (18)F-FDG PET images to assess left ventricular geometry and contractile function. *Journal of nuclear medicine : official publication, Society of Nuclear Medicine* 2003;44(11):1741-1746.
103. Kotovskaia AR, Koloteva MI, Luk'ianiuk V, Zhernavkov AF, Kondratiuk LL. [Individual prediction by the analysis of preflight ECG data of cardiac function disorders in cosmonauts during standard deorbit after long-term space flights and

- in the period of postflight observation]. *Aviakosmicheskaja i ekologicheskaja meditsina = Aerospace and environmental medicine* 2008;42(4):14-20.
104. Feng W, Nagaraj H, Gupta H, Lloyd SG, Aban I, Perry GJ, Calhoun DA, Dell'Italia LJ, Denney TS, Jr. A dual propagation contours technique for semi-automated assessment of systolic and diastolic cardiac function by CMR. *J Cardiovasc Magn Reson* 2009;11:30.
 105. Kurjanova EV, Teplyj DL, Zereninova NV. Development of regulation of the cardiac chronotropic function in albino rats during the early postnatal ontogeny according to the results of spectral analysis of heart rhythm variability. *Bulletin of experimental biology and medicine* 2012;152(6):675-678.
 106. Tibayan FA, Rodriguez F, Langer F, Zasio MK, Bailey L, Liang D, Daughters GT, Ingels NB, Jr., Miller DC. Alterations in left ventricular torsion and diastolic recoil after myocardial infarction with and without chronic ischemic mitral regurgitation. *Circulation* 2004;110(11 Suppl 1):II109-114.
 107. Meral L Reyhan ML, Himanshu Gupta, Steven GLlyod, Louis J Dell'Italia, Hyun J Kim, Thomas S Denney, Daniel Ennisw. Left ventricular twist, but not circumferential-longitudinal shear angle, increases with increasing age in normal subjects. *Journal of Cardiovascular Magnetic Resonance* 2013;15(Suppl 1):P7.
 108. Delhaas T, Kotte J, van der Toorn A, Snoep G, Prinzen FW, Arts T. Increase in left ventricular torsion-to-shortening ratio in children with valvular aortic stenosis. *Magnetic Resonance in Medicine* 2004;51(1):135-139.
 109. Udelson JE. Heart failure with preserved ejection fraction. *Circulation* 2011;124(21):e540-543.

110. Birnkrant DJ, Bushby KM, Amin RS, Bach JR, Benditt JO, Eagle M, Finder JD, Kalra MS, Kissel JT, Koumbourlis AC, Kravitz RM. The respiratory management of patients with duchenne muscular dystrophy: a DMD care considerations working group specialty article. *Pediatric pulmonology* 2010;45(8):739-748.
111. Pauwels RA, Buist AS, Calverley PM, Jenkins CR, Hurd SS, Committee GS. Global strategy for the diagnosis, management, and prevention of chronic obstructive pulmonary disease. NHLBI/WHO Global Initiative for Chronic Obstructive Lung Disease (GOLD) Workshop summary. *American journal of respiratory and critical care medicine* 2001;163(5):1256-1276.
112. Breuer FA, Blaimer M, Heidemann RM, Mueller MF, Griswold MA, Jakob PM. Controlled aliasing in parallel imaging results in higher acceleration (CAIPIRINHA) for multi-slice imaging. *Magnetic resonance in medicine : official journal of the Society of Magnetic Resonance in Medicine / Society of Magnetic Resonance in Medicine* 2005;53(3):684-691.
113. Pruessmann KP, Weiger M, Scheidegger MB, Boesiger P. SENSE: sensitivity encoding for fast MRI. *Magnetic resonance in medicine : official journal of the Society of Magnetic Resonance in Medicine / Society of Magnetic Resonance in Medicine* 1999;42(5):952-962.
114. Setsompop K, Gagoski BA, Polimeni JR, Witzel T, Wedeen VJ, Wald LL. Blipped-controlled aliasing in parallel imaging for simultaneous multislice echo planar imaging with reduced g-factor penalty. *Magnetic Resonance in Medicine* 2012;67(5):1210-1224.

115. Reyhan M, Wang Z, Li M, Kim HJ, Gupta H, Lloyd SG, Dell'Italia LJ, Denney T, Ennis DB. Left ventricular twist and shear in patients with primary mitral regurgitation. *J Magn Reson Imaging* 2014.